Reconfigurable Bulk Acoustic Wave Resonators and Filters Employing Electric-field-induced Piezoelectricity and Negative Piezoelectricity for 5G

by

Milad Zolfagharloo Koohi

A dissertation submitted in partial fulfillment
of the requirements for the degree of
Doctor of Philosophy
(Electrical Engineering)
in the University of Michigan
2020

Doctoral Committee:

Professor Amir Mortazawi, Chair
Professor Ehsan Afshari
Assistant Professor John Heron
Professor Kamal Sarabandi

Milad Zolfagharloo Koohi
milad@umich.edu
ORCID iD: 0000-0003-1764-5510

To my wife and parents

ACKNOWLEDGEMENTS

I have been very lucky to meet a variety of great people in the journey of accomplishing my graduate education. I would like to take this opportunity to acknowledge and thank those that have made my Ph.D. studies possible.

First, I would like to thank my advisor and friend Professor Amir Mortazawi for his support, guidance, and encouragement throughout these years at the University of Michigan, where I learned how to become a successful independent researcher. Second, I would like to thank my thesis committee members. I thank Professor Kamal Sarabandi and Professor Ehsan Afshari for the insightful comments I received from them regarding my research and also their help and support as teachers. I would also like to thank Professor John Heron for providing me with his insights and points of view on my research from a different perspective, which broadened my PhD work.

I would like to thank the research group members of Professor Mortazawi. My PhD was possible with the helps of my brilliant friend Dr. Seungku Lee, with whom I enjoyed my discussions and collaborations during my first two years at Michigan. I thank Suhyun Nam for his collaboration on BST thin film device research as well as co-authoring many conference and journal publications with me. I also thank Dr. Xiaoyu Wang, Dr. Fatemeh Akbar, Omar Abdelatty, Ruiying Chai, and Wenhao Peng for their help and support with classes and research.

I would also like to thank my colleagues and fellow graduate students in the Radiation Laboratory (RadLab), Lurie Nanofabrication Facility (LNF), and Electrical Engineering and Computer Science (EECS) Department. This work would also not be possible without the help of RadLab staff, EECS staff, and support, guidance, and patience of the Lurie Nanofabrication Facility staff. In addition, I must thank my countless friends who have accompanied me through the good and bad times; their presence has been invaluable to me.

Lastly and most importantly, I would like to thank my parents, my wife, my brothers and sisters, for their love and support during the years I have been studying at the University of Michigan.

Milad Zolfagharloo Koohi

August 2020

Table of Contents

LIST OF TABLES

LIST OF FIGURES

ABSTRACT

The ever-expanding wireless communications and sensing are influencing every aspect of human life. With the persistent demand for higher data capacity and recent advancements in wireless technologies, the design of current radio frequency front-end circuitry in communication devices calls for transformative changes. Frequency band proliferation is the biggest contributor to the added RF front-ends complexity in the design of future radios. To operate at various frequency bands, a complex combination of switches and filters is used in mobile devices, and the number of these frequency selective components in each device is expected to exceed 100 with the advent of 5^{th} generation (5G) communication networks. Acoustic wave filters based on piezoelectric materials are the primary technologies employed in current communication systems, including mobile phones. Alternatively, the integration of multifunctional ferroelectric materials into reconfigurable frequency selective components promises reduced complexity, diminished size, and high performance for future radios, enabling them to support 5G wireless technologies and beyond.

A promising reconfigurable bulk acoustic wave technology, employing electric-field-induced piezoelectricity and negative piezoelectricity in ferroelectrics, is presented in this dissertation. Successful implementation of ferroelectric filters would eliminate the need for external switcheplexers in the RF front-ends and reduce the number of required filters, leading to a significant reduction in size, cost, and complexity.

Contributions of this work are categorized into three major parts. In the first part, an intrinsically switchable thin film bulk acoustic wave resonator (FBAR) based on ferroelectric BST with the highest figure of merit (i.e., $Q_m \times K_t^2$) in the literature is presented. The BST FBARs are then employed to design intrinsically switchable filters with the lowest insertion loss to date. Such filters combine filtering and switching functionalities onto a single device, eliminating the need for external switches in RF front-ends.

The second part of this work focuses on the development of frequency and bandwidth reconfigurable filters based on BST FBARs. The first switchless acoustic wave filter bank is presented in chapter 3, demonstrating the capability of BST FBARs in simplifying future agile radios. Next, a novel bandwidth reconfigurable filter based on BST FBARs is introduced in chapter 4, where the idea is experimentally validated with multiple design examples.

Finally, through rigorous mathematical analysis and experimental validation, it has been demonstrated that a dynamic 'non-uniform piezoelectric coefficient' created within a composite structure made up of multi-layers of ferroelectrics allows the selective excitation of different mechanical Eigenmodes with a constant electromechanical coupling coefficient. Such technology overcomes the fundamental limitations associated with the electromechanical coupling coefficient of harmonic resonances in bulk acoustic wave resonators. To create 'non-uniform piezoelectric coefficients' in such structures, ferroelectrics' electric-field-induced piezoelectricity and negative piezoelectricity has been exploited. This innovative technology provides a fundamentally new approach and a

framework for synthesizing programmable frequency selective components, which leads to transformative advances in wireless systems' front-end architecture.

As part of the future direction, it is suggested that the multilayer structure presented in this section to be further studies as part of a new acoustic wave resonator design, which: (a) is capable of operation at a wide frequency range up to mm-wave frequencies designated for 5G (b). Such a structure has the potential to overcome the fundamental limitation of acoustic resonator's ever-decreasing electromechanical coupling factors (K_t^2) as their frequency of operation increases.

CHAPTER I:

Introduction

1.1 Dissertation Motivation

Wireless communication has become an integral part of our lives, continuously improving the quality of everyday activities. A multitude of functionalities are offered by recent generations of mobile phones, resulting in significant adoption of wireless devices and growth in data traffic, as reported by Ericson in Fig. 1.1 [1]. To accommodate consumers' continuous demands for high data rates, the number of frequency bands allocated for communication by governments across the world has steadily been increasing. Furthermore, new technologies, such as carrier aggregation (CA) and multiple input,

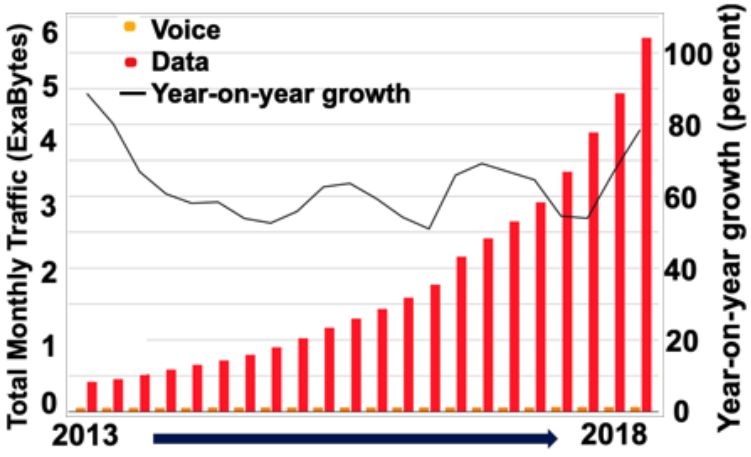

Fig. 1.1 Significant growth in data traffic over the past few years, indicating nearly 60% increase per year [1]

multiple output (MIMO), have been developed to increase the data capacity. Today's mobile devices are capable of supporting numerous wireless technologies (i.e. Wi-Fi, Bluetooth, GPS, 3G, 4G, etc.), each having their own designated frequency bands of operation. Bandpass filters, multiplexers, and switchplexers in RF transceivers are essential for the coexistence of different wireless technologies and play a vital role in efficient spectrum usage. Current mobile devices contain many bandpass filters to select the frequency band of interest, based on the communications standard and available spectrum, as shown in Fig. 1.2. This figure presents a schematic of a generic RF front-end for a typical mobile device. Each generation of mobile devices demands a larger number of RF filters, and with the transition toward 5th generation (5G) communication networks and its corresponding frequency bands, the larger number of required filters will only add to the

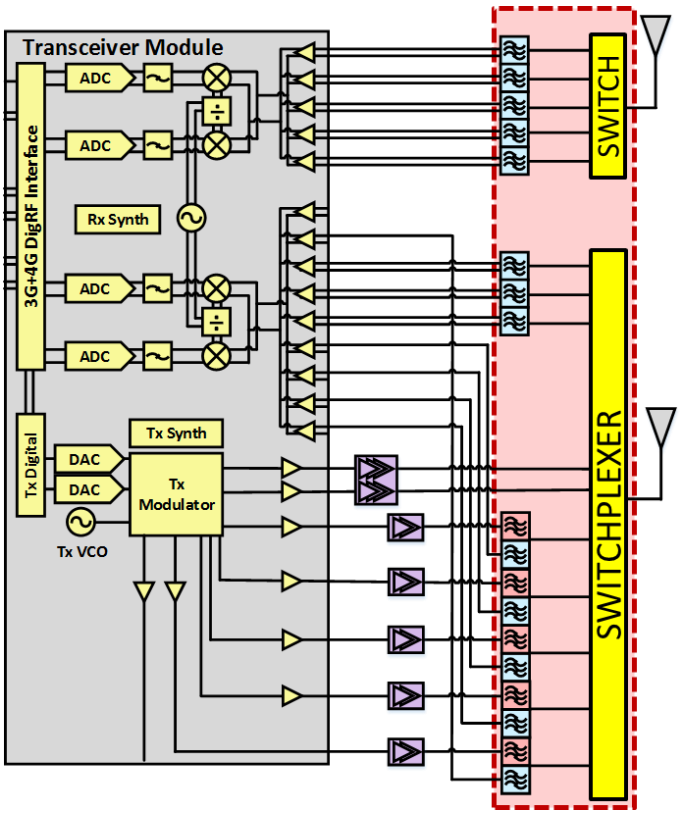

Fig. 1.2 A schematic of a generic RF-front end for a mobile device.

complexity and cost of cell phone RF front-ends.

Currently, only acoustic (piezoelectric) filters can meet the stringent filter requirements in RF front-ends [2]. Although they are capable of meeting the requirements for the current standards, external switches are also required to select between different frequency bands of operation (Fig. 1.2). The addition of the switches to the RF modules adds to their complexity and loss. In today's cellphones, more than 50 filters and switches are employed, and this number is expected to exceed 100 in the nearby future [2]. This poses significant challenges from the cost, size, and power consumption standpoint. A possible approach to address these challenges is to integrate both switching and filtering functionalities onto a single device by replacing the combination of switchplexers and conventional bulk acoustic wave (BAW) filters with intrinsically switchable filters. A simplified version of today's RF front-end block diagram [3] is compared with the envisioned RF front-end based on switchable filters in Fig. 1.3.

The building block of switchable filters is switchable resonators that can be turned on and off with an application of a DC bias voltage. Switchable resonators are realized through electrostatic (capacitive) [4]–[8] or electrostrictive [9]–[16] transduction mechanisms. The performance of electrostatic and electrostrictive based switchable resonators is compared in Table 1.1. High quality factors (*Qs*) in the magnitude of 10000 are achievable in electrostatically transduced resonators. However, such resonators possess large motional resistance, limiting their use in RF systems with 50 Ω standard impedance due to significant impedance mismatch. Also, the low electromechanical coupling coefficient

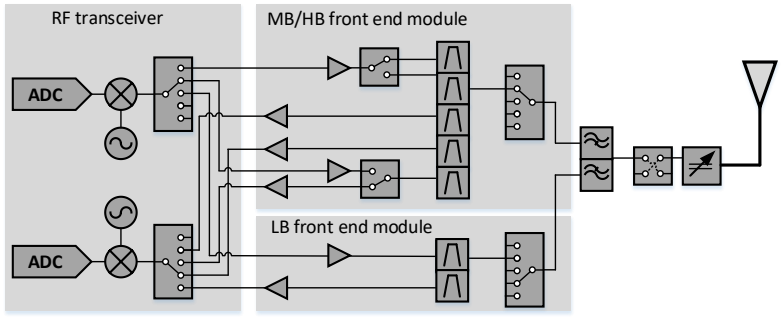

(a)

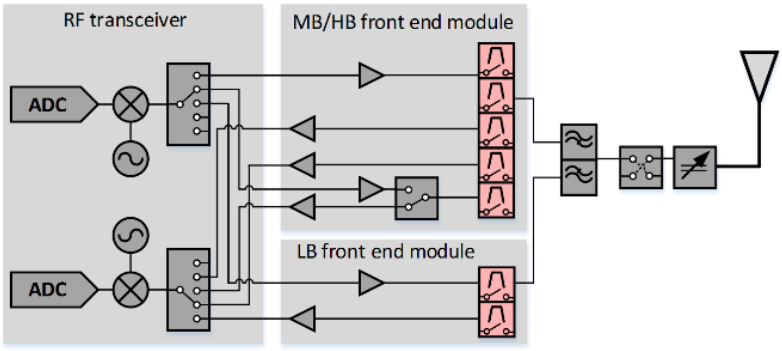

(b)

Fig. 1.3 (a) A simplified block diagram for today's RF-front end architecture [3] and (b) the envisioned architecture based on switchable filters.

(K_t^2) of these resonators limits the maximum achievable bandwidth of the filters. On the other hand, electrostrictive transduction offered by ferroelectrics barium strontium titanate ($Ba_xSr_{(1-x)}TiO_3$ or BST) exhibit high K_t^2 and low motional resistance providing an

Table 1.1
Comparison of Switchable Resonators Based on Transduction Mechanisms [17]

PROPERTIES	**Electrostatic Transduction Based Resonators**	**Electrostrictive Transduction Based Resonators**
Quality Factor (*Q*)	Very High (>10000)	~ 400*
Electromechanical coupling (K_t^2)	Low	High*
Motional Resistance	Very High	Low
Typical Resonance Frequency	Low (<2 GHz)	High

* *Q* and K_t^2 are reported for regular (non-composite) BST thin film bulk acoustic resonator

opportunity to design intrinsically switchable high performance filters. The next section highlights the importance of ferroelectric BST for the design of reconfigurable radio frequency acoustic wave devices.

1.2 Background

1.2.1 Multifunctional Ferroelectric BST

Ferroelectric BST is a multifunctional material, which exhibits distinctive characteristics depending on its operating temperature with respect to the phase transition temperature (i.e., Curie temperature (T_c)) as seen in Fig. 1.4 (a) [18], [19]. Below T_c, the BST material is in the ferroelectric phase, exhibiting a hysteresis in its polarization. Ferroelectric mode of operation is suitable for memory applications such as non-volatile memories (FeRAM) [18]–[20]. However, above T_c, the BST material operates in the paraelectric phase and exhibits multiple characteristics suitable for RF/microwave device applications, such as a large electrostriction coefficient, high relative permittivity, low loss tangent, and integration onto a silicon substrate. For instance, BST's high permittivity (ε_r>200) and electric-field-dependent properties, as shown in Fig. 1.4 (b), has been used to design high-k capacitors and varactors [18]–[22]. Of special interest is the BST's electric-field-induced piezoelectric effect known as electrostriction, which allows BST acoustic wave resonators to be intrinsically switchable.

BST has a cubic perovskite unit-cell structure in its paraelectric phase, as shown in Fig. 1.5. Thus the components of the piezoelectric tensor are all zero in this phase due to its centrosymmetric structure. However, when a DC bias voltage is applied across the ferroelectric material, the electric field displaces the center titanium ion in BST structure,

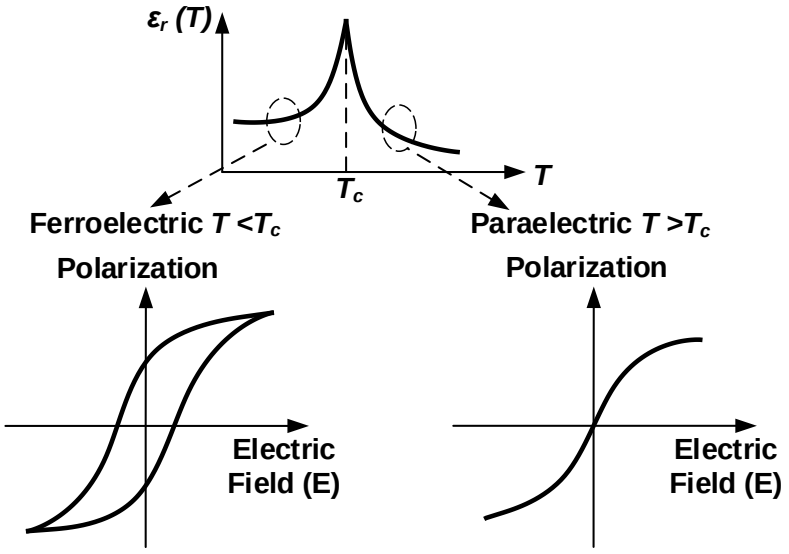

(a)

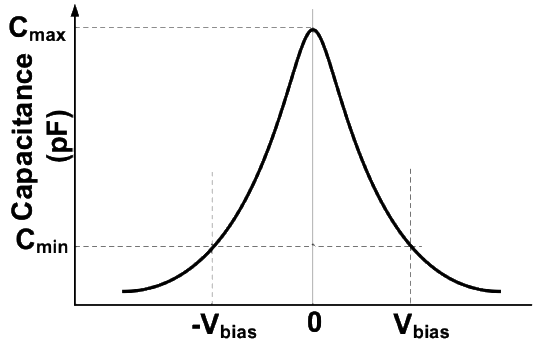

(b)

Fig. 1.4 (a) The temperature-dependent response of ferroelectric BST in its ferroelectric phase (below T_c) and its paraelectric phase (above T_c). (b) A typical BST varactor in paraelectric phase provides a bell shape response as a function of voltage.

leading to a non-symmetric structure that exhibits piezoelectric effect (i.e., E-field-induced piezoelectricity). In conventional piezoelectric materials, the relationship between the electric and acoustic fields is approximately linear under the small signal domain, as shown in Fig. 1.6 (a). In BST, the induced strain and electrical polarization are related by the electrostriction equation (1.1) [23]. The electric polarization under an applied electric field E can be expressed by (1.2):

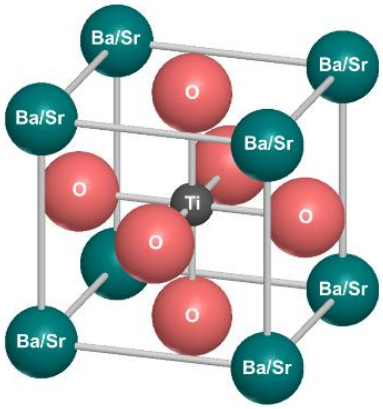

Fig. 1.5 Crystalline structure of perovskite ferroelectric BST in paraelectric phase under zero DC bias voltage, which exhibits no piezoelectric characteristic due to a centrosymmetric unit cell.

$$S = \alpha P^2 \tag{1.1}$$

$$P = P_s + \chi E \tag{1.2}$$

where S is the strain, α is the electrostriction coefficient, and χ is the susceptibility of the material. Substituting (1.2) in (1.1) [23] results in:

$$S = \alpha P_s^2 + (2\alpha P_s \chi + \alpha \chi^2 E)E \tag{1.3}$$

In paraelectric phase BST, where spontaneous polarization is zero (P_s = 0), the electromechanical transduction occurs primarily through the E-field-induced piezoelectric effect (second term in the parentheses) that originates from BST's large electrostriction coefficient. The typical quadratic strain (S)-electric field (E) curve for BST in the paraelectric phase is shown in Fig. 1.6 (b), where the effective piezoelectric coefficient around a particular DC bias point (E_{DC}) is given by the slope of this curve [24]:

$$\frac{dS}{dE}\Big|_{E_{DC}} = 2\alpha\chi^2 E_{DC} \tag{1.4}$$

Based on (1.4), the sign and value of the effective piezoelectric coefficient are functions of the polarity and magnitude of the applied DC electric field ($E_{DC} = \frac{V_{DC}}{t_{BST}}$, where V_{DC} is the voltage across the BST film and t_{BST} is the BST film thickness). As shown in Fig. 1.6 (b), BST film biased to the left side of the curve, under a negative DC voltage, presents a 'negative piezoelectric' coefficient to an ac field applied across the electrodes. The E-field-induced piezoelectricity and 'negative piezoelectricity' can be used to control the electromechanical coupling in BST with a DC bias voltage, and it has been utilized in designing a wide range of reconfigurable BAW devices throughout this dissertation.

1.2.2 Intrinsically Switchable BST Bulk Acoustic Wave Resonators

High performance, compact, and low-cost BAW resonators are essential components of modern wireless communication systems. BAW resonators consist of a piezoelectric transduction layer, sandwiched between two metal electrodes. RF signals applied to the electrodes excite acoustic waves that propagate within the bulk of the device. The propagating bulk acoustic waves will, in turn, generate an electrical response. The acoustic

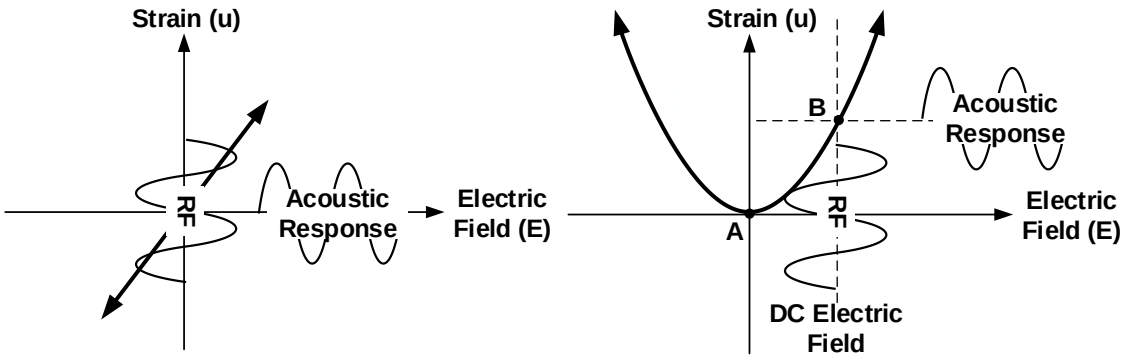

Fig. 1.6 (a) Simplified illustration of acoustic-electric fields interactions in a typical piezoelectric materials and (b) the electric field induced piezoelectricity of BST as a result of its strong electrostriction property. Under zero DC electric field (E = 0 V/m, point A), the slope of the curve is zero and no acoustic wave is excited; biasing the material under DC electric field (point B) enables the material to couple the electric energy into acoustic waves.

waves are confined within the resonator due to the acoustic impedance mismatch between the resonator body and its surrounding environment. There are two primary methods of confining the bulk acoustic waves; hence BAW resonators are classified into two different categories. The first type of BAW resonator is the solidly mounted resonator (SMR), which utilizes an acoustic Bragg reflector, comprised of alternating quarter-wavelengths of high and low acoustic impedance materials, to confine the acoustic energy at the design frequency. The second type is the thin film bulk acoustic wave resonator (FBAR) that utilizes the mismatch between the resonator material and air, by removing the material surrounding the resonator to confine acoustic waves. Simplified cross-sectional views of SMRs and FBARs are shown in Fig. 1.7. The resonance frequency of both FBARs and SMRs is determined by the thickness of the layers that make up the device. Furthermore, both types of BAW resonators have been heavily used in the telecommunications industry, each with their distinct advantages.

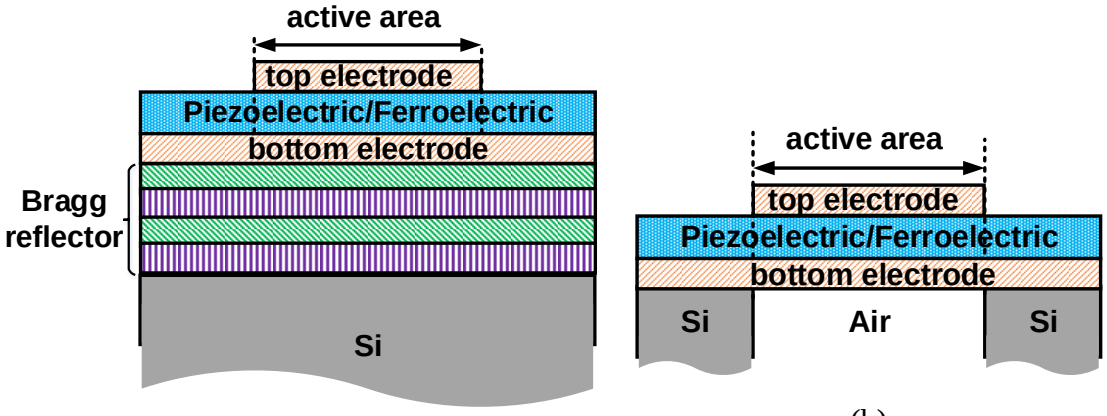

Fig. 1.7 Cross-sectional views of typical (a) solidly mounted resonators (SMRs) and (b) thin film bulk acoustic resonators (FBARs).

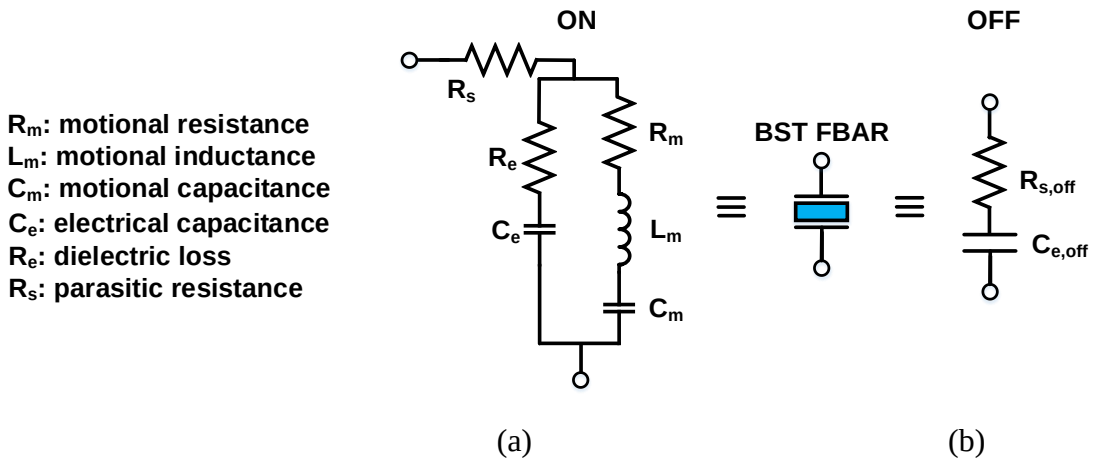

Fig. 1.8 (a) ON state lumped element mBVD model for a 1-port switchable BST FBAR and (b) its OFF state capacitive model. [28]

Bulk acoustic wave resonators (FBAR and SMR) based on ferroelectric BST possess several unique features, which can simplify the RF front-ends. Due to BST's strong electrostriction properties, BST resonators can be switched on and off with the application of a DC bias voltage [9]–[18], [25]–[28]. Furthermore, due to the high permittivity of BST, it is possible to design much smaller resonators as compared to the resonators based on the traditional piezoelectric materials, therefore significantly reducing the size of RF front-end modules.

The electrical behavior of ferroelectric resonators in the ON state can be represented by a modified Butterworth-Van Dyke (mBVD) model [29], shown in Fig. 1.8 (a). In this figure, the motional branch is modeled by a capacitor (C_m) in series with an inductor (L_m), forming the series resonator. The additional resistor (R_m) represents the mechanical loss factor. The electrical branch consists of a static capacitance (C_e) along with a resistance (R_e), which represents the dielectric loss as well as the losses associated with laterally propagating waves. Under zero DC bias voltage, the resonator is in its OFF state, and the motional branch in this model (i.e., L_m, C_m, R_m) vanishes, as shown in Fig 1.8 (b). The

lumped element circuit models are utilized to design intrinsically switchable ferroelectric filters to predict their ON and OFF states' responses.

1.3 Dissertation Goal and Organization

The goal of this dissertation is to design, simulate, fabricate, and characterize reconfigurable bulk acoustic wave filters by exploiting the electric field induced piezoelectricity and negative piezoelectricity in ferroelectric BST for future agile RF front-ends. The organization of this dissertation is as follows. In the second chapter design and fabrication process for an optimized BST FBAR are detailed, demonstrating the maximum reported figure of merit (product of quality factor and electromechanical coupling coefficient) based on the strong electrostriction coefficient in BST. Such resonators are then employed to design a variety of reconfigurable devices in the following chapters.

In chapter 3, intrinsically switchable FBAR filters based on ferroelectric BST are presented. A 1.5 stage π-network intrinsically switchable FBAR filter unit cell with a 3-dB fractional bandwidth of 3% at 2 GHz is systematically designed, simulated, and fabricated. The minimum insertion loss (IL) for the filter unit cell is 2.25 dB, representing the lowest IL reported for BST BAW filters to date, which is mainly due to its high $Q \times K_t^2$ BST resonators. Two 1.5-stage filter unit cells are connected in series to form a 2.5-stage filter, providing more than 25 dB of out-of-band rejection and OFF-state isolation between the input and the output ports.

Reconfigurable bulk acoustic wave filters provide a number of advantages for wireless communication systems, including compact size, cost-effectiveness, and less complexity. Chapter 5 focuses on an intrinsically switchable and frequency reconfigurable filter bank based on BST FBARs. In this chapter, a triple band switchable filter bank, consisting of

three 2.5 stage filters based on BST FBARs, is designed, simulated, and fabricated for the first time. The bandpass filters have center frequencies at 1.85, 1.96, and 2.04 GHz and are selectively turned on based upon the external DC bias voltage applied to each filter. Turning off all the filters provide an isolation of more than 27 dB between the input and the output ports. The presented intrinsically switchable ferroelectric filter bank potentially simplifies future RF front ends by integrating both switching and filtering functionalities onto a single device and reduces the overall circuit area.

Chapter 4 presents on a novel design methodology of an intrinsically switchable and bandwidth reconfigurable FBAR filter, employing the electrostriction in ferroelectric BST. Two examples of BST based FBAR filters are designed and fabricated as a proof of concept. Under the application of a dc bias voltage, the fabricated switchable filters exhibit a bandpass response with a fractional BW of 3%. By changing the state of BST FBARs through applied DC bias voltages, the bandwidth of the filters is adjusted. Without any bias, the filters switch off to provide isolation between the input and output ports. BST based bandwidth reconfigurable filters can potentially reduce the number of required filters and switches in the future multi-band RF front-ends.

In chapter 6, a new class of ferroelectric FBARs (i.e., mode-switchable FBARs) is introduced, and its design procedure is detailed. Such resonators operate based on a dynamic non-uniform effective piezoelectricity in composite multi-layer ferroelectrics with large electrostriction coefficients, like BST. Harmonic resonance modes (nf_o) of a multilayer ferroelectric bulk acoustic wave resonator can be selectively excited with an effective electromechanical coupling coefficient (K_{eff}^2) equal to the fundament mode, which is contrary to the trend $K_{eff}^2 \propto 1/n^2$ exhibited by conventional piezoelectric bulk

acoustic wave resonators [30]. Such a device can selectively be set to resonate at its different resonance harmonics by generating a pattern of non-uniform piezoelectric coefficient proportional to the stress field of each mode with an application of a proper set of DC control voltages applied across the ferroelectric layers. Such a resonator allows for the design of a new class of band-switching filters. As an experimental validation, a mode-switchable FBAR and a band-switching ladder-type filter based on a bilayer ferroelectric BST structure are designed and fabricated for the first time. The bilayer BST FBARs not only can be switched on or off, but also, by choosing different bias configurations, two resonance modes at 2 GHz and 3.6 GHz can be selectively excited having K_{eff}^2 of 8% and 7%, respectively.

Chapter 7 summarizes this work and presents the future direction of reconfigurable acoustic wave devices based on BST. Finally, journal and conference publications out of this work are listed.

CHAPTER II:

Design and Characterization of Intrinsically Switchable Ferroelectric BST FBARs

2.1 Chapter Motivation

Intrinsically switchable FBARs and SMRs based on BST have been investigated for the realization of intrinsically switchable BAW filters and multi-frequency-switchable oscillators [9]–[17], [25]–[28]. In general, BAW filter performance is dependent on its constituent resonators' performance. Important parameters of the acoustic resonators that affect the overall response of the BAW filters are their mechanical quality factor (Q_m) and electromechanical coupling coefficient (K_t^2). Mechanical quality factor represents the acoustic loss within a resonator, and K_t^2 describes the coupling strength between electric and acoustic energy in a resonator. A higher Q_m means a lower mechanical loss, allowing for the design of filters with a lower insertion loss (IL) and a sharp roll off. On the other hand, K_t^2 sets the limit for maximum achievable filter bandwidth (BW). Thus, high $Q_m \times K_t^2$ switchable BST resonators are needed to achieve a low IL, large BW, and sharp roll off in BST filters' ON state. Therefore, after selecting the materials and the technology

for a BAW filter design application, optimization of resonator structure is necessary. It can be accomplished by carefully selecting the thickness of constituting layers of the resonator, as discussed in this chapter.

Also, the BST transduction layer deposition process can significantly affect its electrical and mechanical properties, and consequently, the device performance. Previously, BST FBARs, fabricated using a pulsed laser deposition (PLD) system was reported with Q_m and K_t^2 values as high as 233 and 7%, respectively [9]. Another promising method for the fabrication of ferroelectric films is RF magnetron sputtering, which offers high uniformity over large area wafers, scalability, compatibility with standard IC processing, and low investment cost. Sputter deposited BST has been used for the design of BST SMRs with $Q_m s$ as high as 350; however, the reported K_t^2 for such resonators is about 2.4%, reducing the overall resonator figure of merit [14]. This chapter presents the design process for BST FBARs and their fabrication process using a sputtering technique, providing the highest $Q_m \times K_t^2$ to date. Important characteristics of the fabricated resonators, including quality factors, K_t^2, and temperature coefficient of frequencies (TCF) are measured and reported.

Finally, another key factor in the design of the filters is the linearity of resonators, which should meet the stringent requirements for multiband CA operations. A practical approach for improving the linearity is to modify the filter circuit architecture. For example, in the filter structure, the resonators that experience a large voltage swing can be replaced with multiple cascaded larger resonators. As an example, a single BST resonator and two cascaded BST resonators, each with twice the area of the single resonator is designed, fabricated, and their linearity and acoustic performance are compared.

2.2 Ferroelectric BST FBAR Design for Maximum K_t^2

A 1-D transmission line model is used to optimally design the FBAR structure [31]. The resonator structure consists of a BST layer sandwiched between top and bottom electrodes (Pt), as shown in Fig. 2.1. A thin SiO_2 diffusion barrier layer has also been used beneath the bottom electrode to avoid diffusion of Si into Pt layer during the BST deposition process. The 1-D acoustic wave transmission line model predicts the electrical response of a bulk acoustic resonator as a function of the material parameters and thickness of the constituting layers.

Each layer is modeled with an acoustic transmission line through its material properties, including acoustic impedance, acoustic velocity, and mechanical quality factor. First, the air at the top and bottom of the structure is included in the model as a termination with its acoustic characteristic impedance (Z_{air}). Then the load impedance Z_{air} is transformed to $Z_{bot,e}$ and $Z_{top,e}$ through successive impedance transformation by (2.1).

$$Z_i = \frac{Z_o(Z_L + Z_o \tanh(\gamma t_i))}{Z_o + Z_L \tanh(\gamma t_i)} \tag{2.1}$$

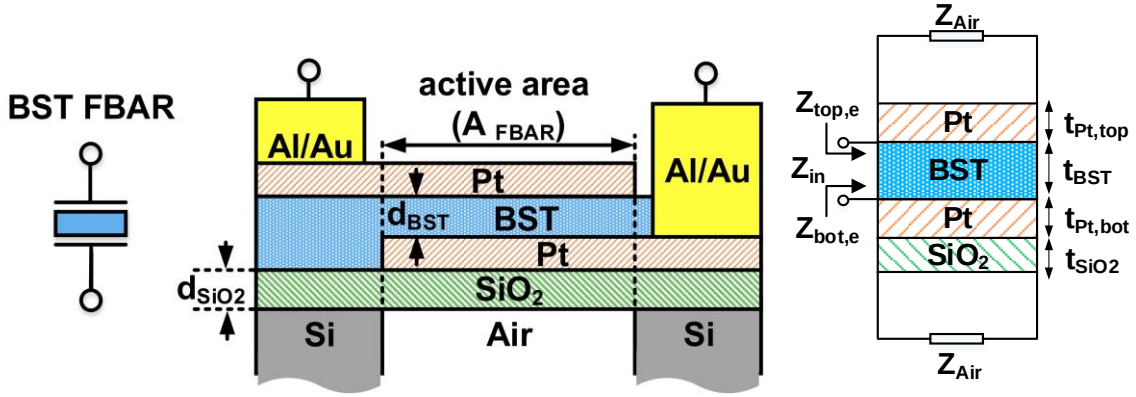

Fig. 2.1 Simplified cross-sectional view of the designed BST FBAR.

where γ, t, and Z_o are the acoustic propagation constant, thickness, and acoustic characteristic impedance of each layer, respectively, and Z_L is the acoustic impedance seen looking into the previous layer. The propagation constant (γ) of each layer is calculated by (2.2).

$$\gamma = \alpha + j\beta \tag{2.2}$$

$$\alpha = \frac{\beta}{2Q_m} \text{ and } \beta = \frac{\omega}{v} \tag{2.3}$$

where α, β, Q_m, ω, and v represents the attenuation constant, phase constant, mechanical quality factor, angular frequency, and acoustic velocity of each layer, respectively. Finally, the electrical input impedance of the BST FBAR (i.e., Z_{in} in Fig. 2.1) can be calculated as follows.

$$Z_{in} = \frac{1}{j\omega C_e}\left[1 - \frac{K^2 \tan\left(\frac{\phi}{2}\right)}{\frac{\phi}{2}} \times \frac{\left((z_t+z_b)\cos^2\left(\frac{\phi}{2}\right)+jsin\left(\frac{\phi}{2}\right)\right)}{(z_t+z_b)cos(\phi)+j(z_t z_b+1)\sin(\phi)}\right. \tag{2.4}$$

$$z_t = \frac{Z_{top,e}}{Z_{BST}} \text{ and } z_b = \frac{Z_{bot,e}}{Z_{BST}} \tag{2.5}$$

where K^2, φ, and C_e are the intrinsic electromechanical coupling coefficient of the BST, the acoustic phase across the BST layer, and the capacitance, respectively. The material parameters which have been used in the acoustic wave transmission line model are provided in Table 2.1. The intrinsic electromechanical coupling coefficient for BST (K^2_{BST}) thin film in ON state that has is used in this model is extracted from the measurements to be 10%. To calculated the K^2_{BST}, a 1-D acoustic wave transmission line model is fitted to a measured BST FBARs under 60 V bias voltage, that has been fabricated under similar conditions.

A BST FBAR is designed to have a fundamental resonance mode at 2 GHz through 1-D acoustic wave TL simulations. In these simulations, the effect of a 300 nm-thick silicon dioxide diffusion barrier layer used underneath the bottom electrode to prevent Si diffusion into the Pt bottom electrode has been taken into account. The thickness of both the top and bottom electrodes is set to be equal in the FBAR structure.

Table 2.1
Acoustic Material Parameters for Different Layers in BST FBARs

Material	***v (m/s)***	***Z_0 (kg/m^{2}s)***	***Q_m***
Pt	3236	69.410^6	260
BST	6307	35.3×10^6	500
SiO_2	5848	12.8×10^6	1000
Si	8445	19.7×10^6	2000
Au	2800	63.8×10^6	200

Using the acoustic transmission line model, K_t^2 as a function of electrode-to-BST thickness ratio for an FBAR structure similar to Fig 2.1 with a fundamental resonance mode at 2 GHz is plotted in Fig. 2.2 (a). It can be seen that K_t^2 is within 99% of its maximum value for electrode-to-BST thickness ratio of 0.05 to 0.1. Therefore in order to minimize the ohmic loss while maintaining a large K_t^2, an electrode-to-BST of 0.1 is selected. For a fixed

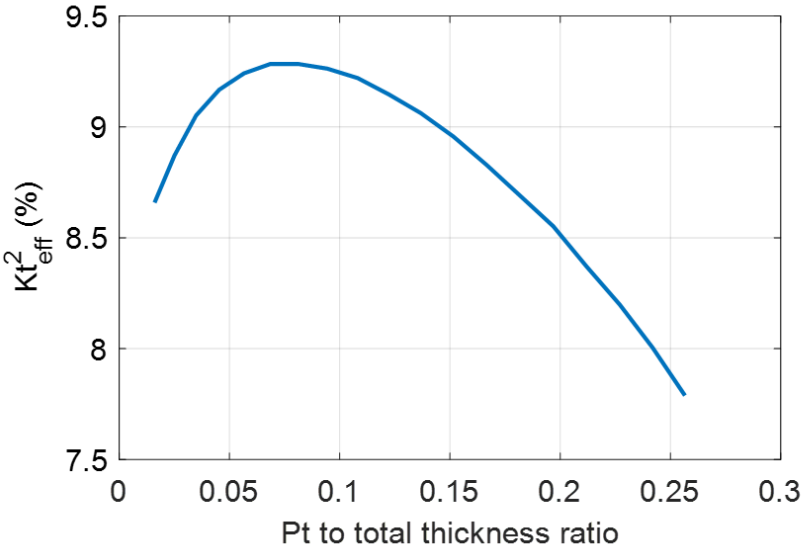

(a)

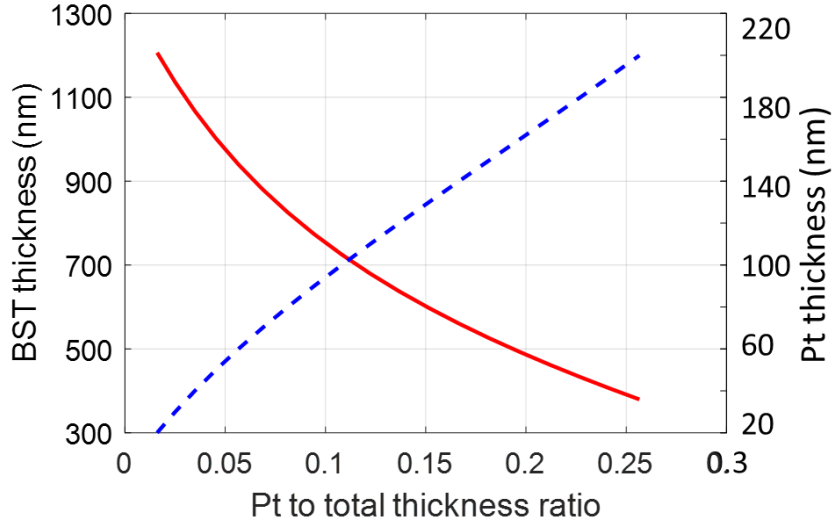

(b)

Fig. 2.2 (a) Effective electromechanical coupling coefficient (K_t^2) (d) thickness values of BST and Pt as a function of BST to total thickness ratio for resonator fundumental mode at 2 GHz.

fundamental resonance frequency at 2 GHz, both BST and electrodes thicknesses are plotted as a function of the electrode-to-BST ratio, as shown in Fig. 2.2 (b). The final thickness values of BST and each electrode are then determined from Fig. 2.2 (b) to be 770

and 100 nm, respectively; thus, the total BST FBAR membrane thickness is 1.27 μm. The thickness of all the layers in the BST FBAR structure is summarized in Table 2.2.

Table 2.2
BST FBAR's Designed Thickness Values

Layers	**Pt_{top}**	**BST**	**Pt_{bottom}**	**SiO_2**
Thickness values (nm)	100	770	100	300

2.3 Fabrication Procedure for BST FBARs Using RF Magnetron Sputtering

BST FBARs are fabricated on a high resistivity (100) oriented silicon substrate that has a thickness of 500 μm and resistivity of more than 10 KΩ × cm. The fabrication steps for the BST FBARs are depicted in Fig. 2.3. Fabrication starts by thermally growing a 300 nm SiO_2 on the Si wafer. The SiO_2 layer beneath the bottom electrode plays an essential role as a diffusion barrier during the high-temperature deposition of the ferroelectric BST. Thermally grown SiO_2 is a low loss material with a positive thermal coefficient of elasticity (TCE), and it is commonly used to compensate for the negative TCF of FBARs [30]. In the next step, a 100 nm-thick Pt bottom electrode is deposited and patterned by evaporation and lift-off. A 3.0 nm-thick layer of Ti is used for the adhesion of Pt bottom electrode to the SiO_2 layer. A 770-nm of BST is then deposited by an RF magnetron sputtering system at 650 ℃ in a 45 mTorr Ar and O_2 (4:1) environment. Two sputtering guns with RF power levels of 300 Watt are used for BST deposition. A 100 nm-thick layer of Pt is then deposited and patterned by evaporation and lift-off to serve as the top electrode. After

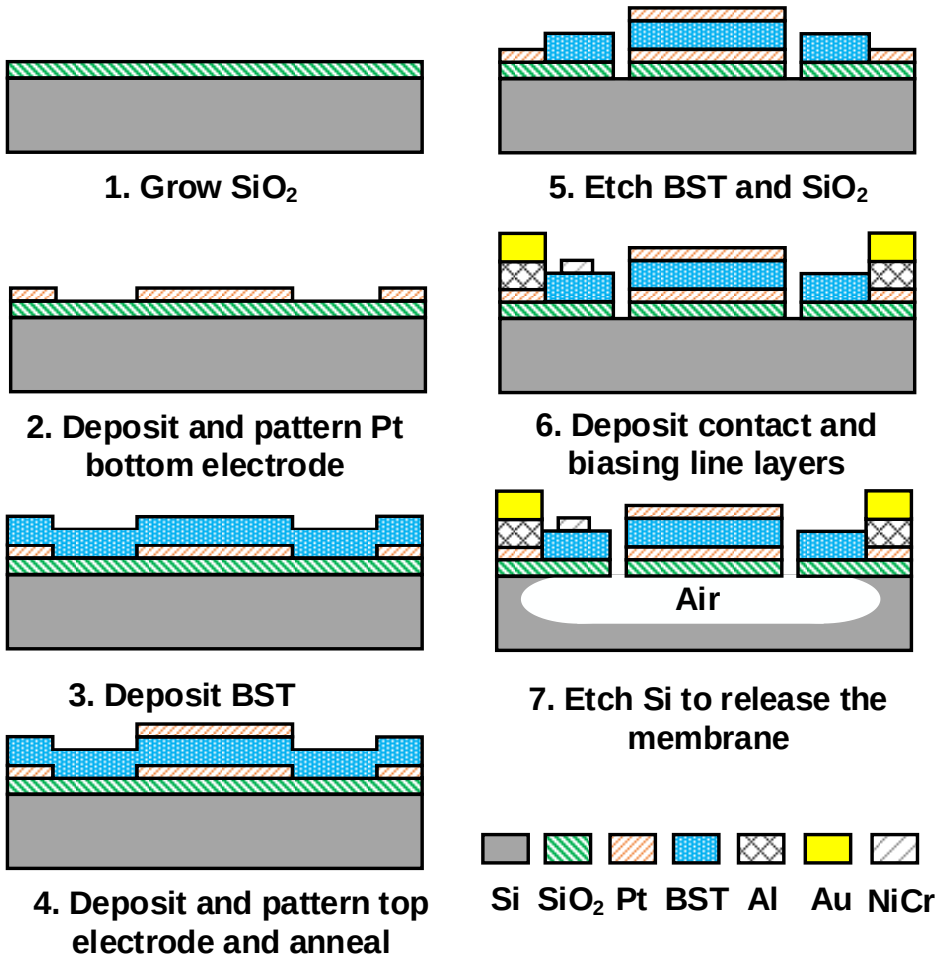

Fig. 2.3 Fabrication steps for the BST FBARs.

annealing the chip at 500 °C for 30 minutes in an O_2 environment, BST is etched in buffered HF (BHF) to create the release holes and a via to the bottom electrode. A layer of Ti/Al/Au (50/1300/100 nm) is then deposited and patterned using evaporation and lift-off as a contact layer. BST FBARs are released by etching the Si substrate beneath the device in a 3.0 Torr XeF_2 environment.

Device S-parameters are measured using a Keysight network analyzer and a Cascade Microtech probe station with ground-signal-ground (GSG) probes of 250 μm pitch size. Short-open-load-through (SOLT) calibration is performed for a 50 Ω system impedance.

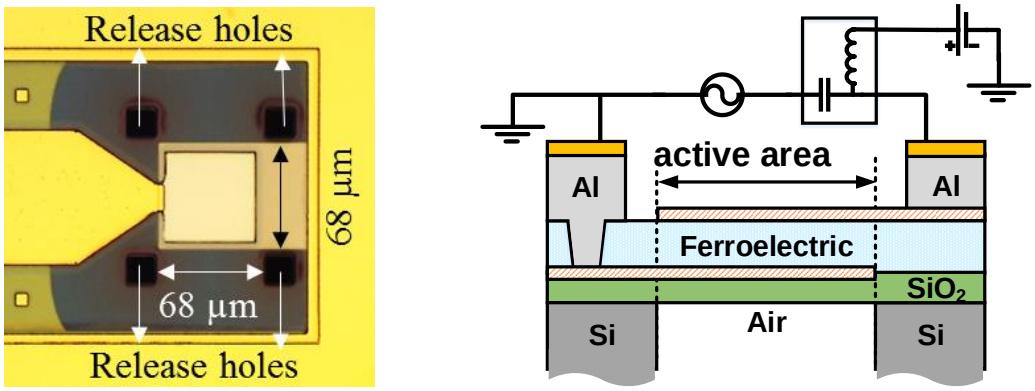

(a) (b)

Fig. 2.4 (a) Photograph of a fabricated BST FBAR, and (b) its cross sectional view that includes the biasing circuitry.

DC-bias voltages are applied through a bias tee connected to the input probe. Finally, S-parameters for the BST FBAR in ON (at 60 V DC) and OFF (no DC-bias applied) states are measured. The photograph of a fabricated BST FBAR operating at 2 GHz frequency, its cross-sectional view, and biasing circuitry are presented in Fig. 2.4. The size of the resonator active area is $68\ \mu m \times 68\ \mu m$.

2.4 A BST FBAR Measurement Results

The measurement setup for the fabricated BST FBARs is depicted in Fig. 2.5, where a DC bias voltage is applied through a bias tee connected at the input port of the device.

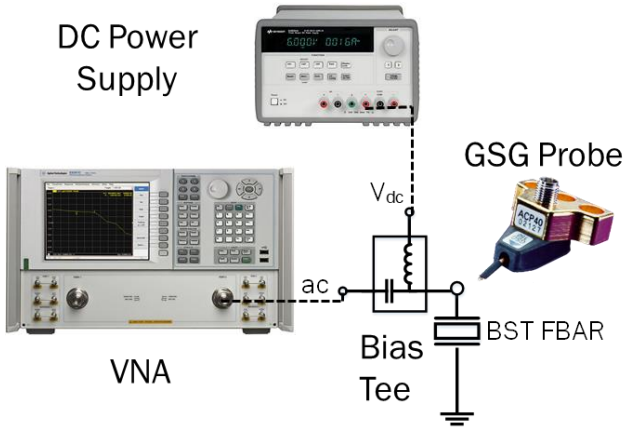

Fig. 2.5 Measurement setup for the fabricated BST FBAR.

The device S_{11} plotted on a Smith chart he magnitude of the input impedance for the fabricated BST FBAR in both ON (60 V) and OFF (0 V) states are provided in Fig. 2.6. By applying a DC bias voltage, a thickness mode resonance is turned on, due to BST's electric-field-induced piezoelectricity. The series and the parallel resonance frequencies

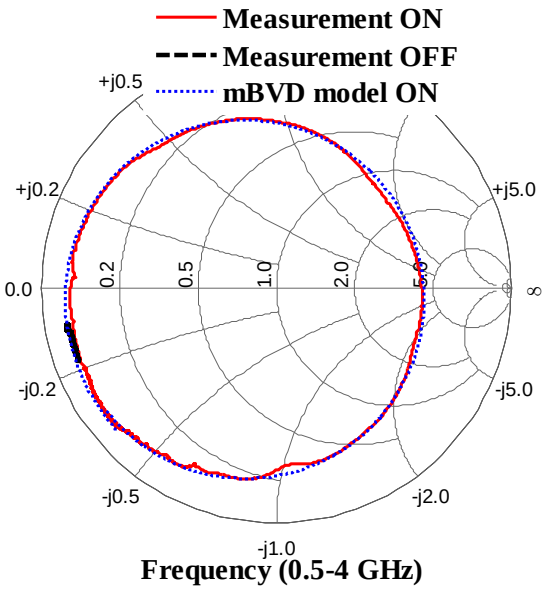

(a)

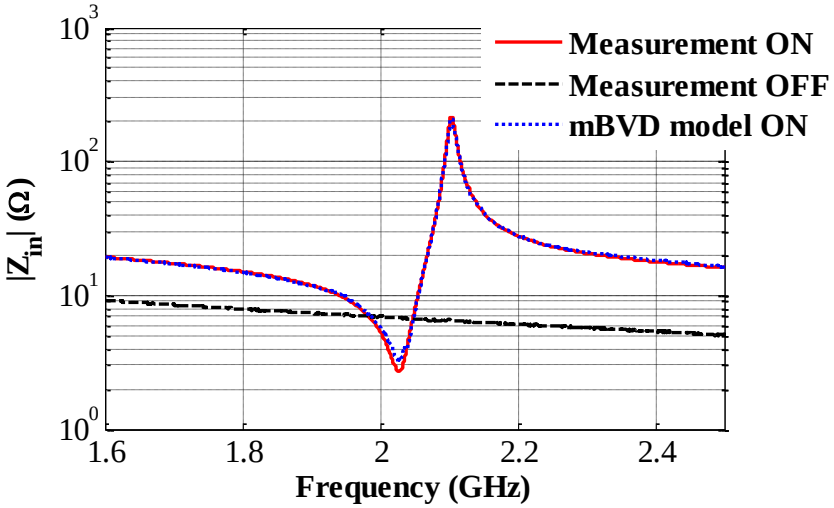

(b)

Fig. 2.6 (a) Magnitude of input impedance, and (b) reflection coefficient on Smith chart for the measured 1-port switchable BST FBAR in ON (70 V) and OFF states.

(frequencies at which the real part of the input admittance and impedance become maximum) are 2.028 GHz and 2.104 GHz, respectively. The required $V_{DC,ON}$ of 60 V, can be reduced to less than 20 V by fabricating the resonators based on a BST layer with better crystallinity, as demonstrated in [18]. In mobile phones, dc to dc boost converters, can be used to create the required dc bias voltage [32]. For further analysis, mBVD model presented in Fig. 2.7 is developed by using the measured FBAR data. The mBVD model parameter values are provided in Table 2.3. The resonator parameters, including K_t^2, Q_s, Q_p and Q_m are calculated using (2.6) and (2.7) [30] to be 8.6%, 100, 183 and 360, respectively. The BST FBAR presented here provides the highest $Q_m \times K_t^2$ as compared to the previously reported BST resonators.

$$K_t^2 = \frac{\pi^2}{4}\frac{f_s}{f_p}\frac{(f_p - f_s)}{f_p} \tag{2.6}$$

$$Q_s = \frac{\omega_s L_m}{R_m + R_s}, Q_p = \frac{\omega_p L_m}{R_m + R_e}, Q_m = \frac{\omega_s L_m}{R_m} \tag{2.7}$$

In order to calculate the BST FBAR TCF, the S-parameters are collected for a resonator at different temperatures ranging from 30 to 100 °C. The thermal coefficients of frequency for the series and parallel resonance frequencies are calculated using (2.8). The

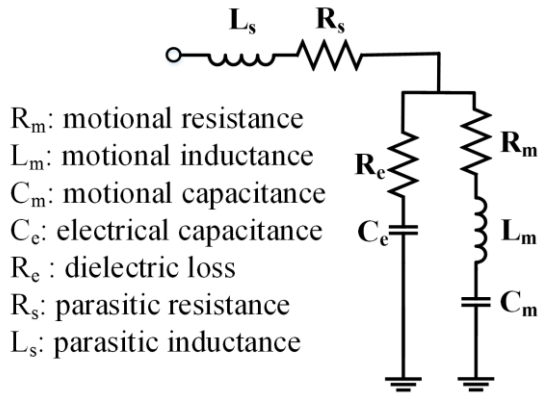

Fig. 2.7 mBVD model for a 1-port switchable BST FBAR.

temperature-dependent properties of the resonators are measured by varying the device temperature from 25 °C to 110 °C on a heating stage and recording the S_{11} around the device resonance frequency. TCF for the series and the parallel resonances of the fabricated BST FBAR are -65 ppm/K and -68 ppm/K over the measured temperature range, which is partially compensated by adding the SiO_2 layer. It is possible to fully compensate for the TCF of BST with a thicker SiO_2 layer.

$$\alpha_T = \frac{1}{f(T)}\frac{\partial f}{\partial T} \tag{2.8}$$

Table 2.3
mBVD Model Parameters

Parameter	**Value**	**Parameter**	**Value**
L_m (nH)	21.78	R_e (Ω)	0.795
R_m (Ω)	0.778	R_s (Ω)	2.037
C_m (pF)	0.280	L_s (nH)	0.133
C_e (pF)	4.107		

2.5 Linearity Measurements of BST FBARs

An important factor in the design of the acoustic wave filters is their linearity, which should meet the stringent requirements for multiband carrier CA operations. A practical approach for improving the linearity is to modify the filter circuit architecture. For example, in the filter structure, the resonators that experience a large voltage swing can be replaced with series connected larger resonators. It is expected that in a cascaded structure, IP_3 increases by $20\cdot\log_{10}N$ dB, N being the number of cascaded resonators. In this section, a single BST resonator and two series connected BST resonators, each with twice the area

of the single resonator, are designed, fabricated, and their linearity and acoustic performance are compared. Ideally, for N = 2, the IP_3 is expected to improve about 6 dB.

The photograph of the fabricated BST FBAR and the two cascaded BST FBARs are shown in Fig. 2.8. The size of the single resonator is 38 μm × 38 μm, while the size of each resonator in the cascaded structure is 76 μm × 38 μm. Measured S_{11} for single and cascaded resonators, when their second ports are grounded, is plotted on the Smith chart in both ON (60 V) and OFF (0 V) states, as shown in Fig. 2.9. The mBVD model for each ON state resonator is extracted and provided in Table 2.4. Based on these parameters, the quality factor and electromechanical coupling coefficient for both structures are calculated by (2.6) and (2.7) and listed in Table 2.4.

Through IP_3 measurements, the linearity of the BST FBAR is investigated. Two tones with Δf = 10 MHz having the same power, around the resonance frequency of each resonator, is injected to the input port. The output signal is fed into a spectrum analyzer, as shown in Fig. 2.10. The signal powers at the fundamental frequencies, along with their third order intermodulation products, are recorded. The measured input third-order intercept point (IIP_3) for a single resonator is 39 dBm, while the cascaded structure

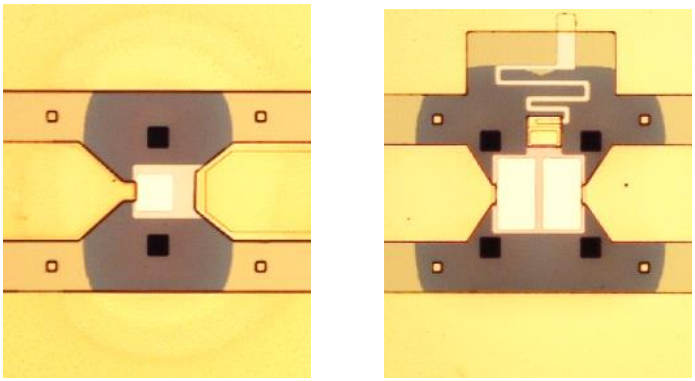

(a) (b)

Fig. 2.8 Photographs of (a) the single and (b) cascaded BST FBARs.

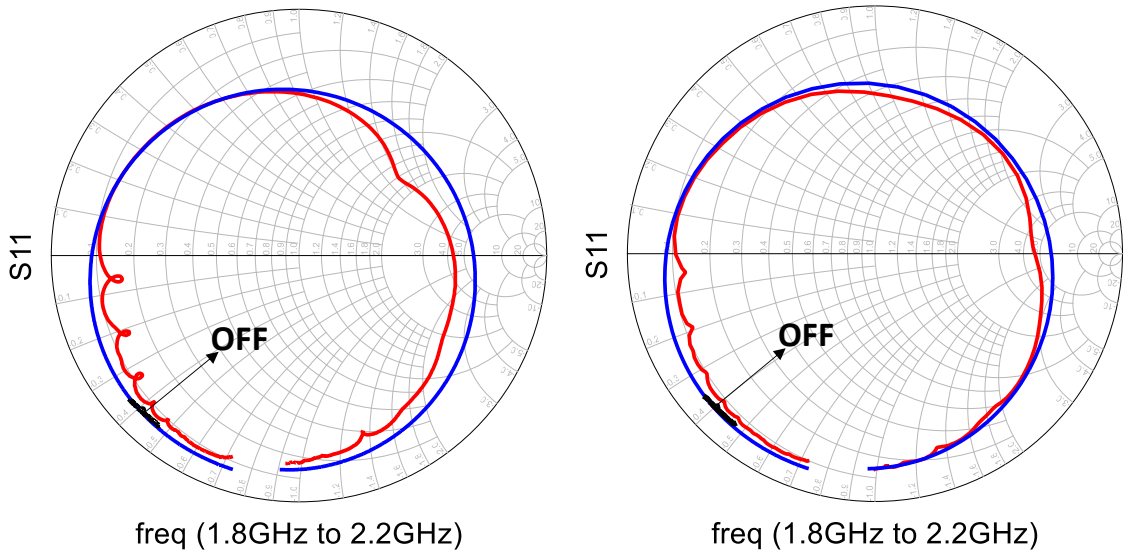

(a) (b)

Fig. 2.9 The measured S_{11} plotted on Smith chart for (a) a single BST FBAR and (b) a cascaded doubled size resonator in their ON and OFF states. Their lumped element mBVD model is also plotted in a dashed blue line on the same figure.

Table 2.4
Lumped Element mBVD Model Parameters for Measured Resonators

BST Resonator	**L_m (nH)**	**C_m (pF)**	**C_e (pF)**	**R_m (Ω)**	**R_e (Ω)**	**R_s (Ω)**
Single BST FBAR	76.75	0.84	1.94	2.78	2.96	1.66
Cascaded BST FBAR	68.29	0.92	1.93	2.55	2.95	1.70

presented an IIP_3 of 43 dBm. The variation between the 4 dB IP_3 improvement and the expected 6 dB value can be attributed to the nonzero series ohmic resistance of the resonator lead and routing.

The measurement results provided in Table 2.5 demonstrate that by cascading BST FBARs in series, a greater linearity can be achieved with comparable acoustic performance to the single resonator. As expected, by replacing each BST resonator with multiple series-connected larger resonators, the voltage swing across individual resonators is smaller,

which results in better linearity [30]. As seen in Fig. 2.9, the effect of lateral spurious modes on the cascaded BST FBARs is also less severe due to the larger size of the resonators. Finally, it should be noted that the size of the BST FBARs is considerably smaller compared to conventional piezoelectric FBARs, even with the cascaded structure.

Table 2.5
Measured Specifications of the Single and Cascaded BST FBARs

BST Resonator	f_s **(GHz)**	f_p **(GHz)**	Q_m	K_t^2 **(%)**	**IIP$_3$ (dBm)**
Single BST FBAR	1.982	2.024	343	5.0	39
Cascaded BST FBAR	1.998	2.046	336	5.6	43

2.6 Chapter Conclusion

A procedure for optimizing the FOM (i.e., high $Q_m \times K_t^2$) of BST FBARs is presented. A high $Q_m \times K_t^2$ BST FBAR, which is intended for designing low insertion loss switchable BAW filters, has been designed and fabricated. K_t^2 and Q_m of the fabricated BST FBAR in ON state are 8.6% and 360, respectively. TCF for the series and the parallel resonance frequencies of the BST FBAR is also measured to be -65 and -68 ppm/K, respectively. A single BST FBAR and two cascaded BST FBARs are designed and fabricated to compare their linearity and performance. Through IP$_3$ measurements, it has

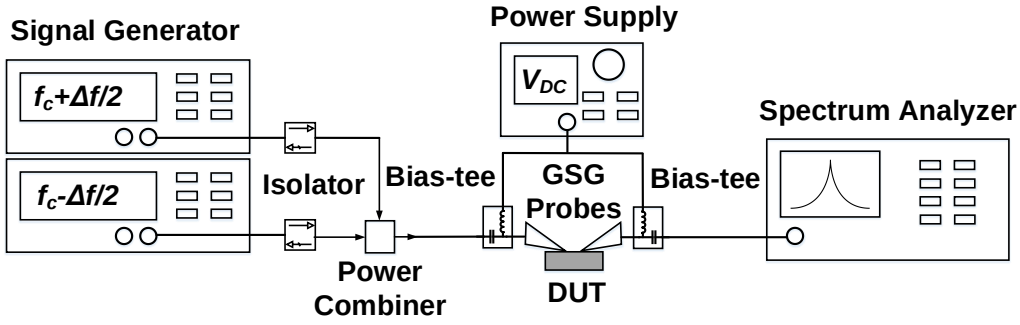

Fig. 2.10 Two tone measurement setup for intermodulation distortion of the BST FBARs.

been shown that the cascaded structure effectively improves the linearity of the BST FBARs, while providing an acoustic performance similar to a single BST FBAR. The BST FBARs developed in this chapter are the building blocks for designing a variety of reconfigurable BST FBAR filters presented in the following chapters.

CHAPTER III:

Intrinsically Switchable Ferroelectric Filters

3.1 Chapter Motivation

The rapidly multiplying number of frequency bands in mobile devices, as a response to consumers' continuous desire for higher data rates, has resulted in complex wireless communication systems. Today's mobile devices are required to support many wireless technologies (i.e., Wi-Fi, Bluetooth, GPS, 3G, 4G, etc.), each having their designated frequency bands. These devices contain a significant number of RF switches and band-select filters, allowing appropriate band selection based on the frequency and mode of operation [33]. The introduction of 5^{th} generation (5G) communication networks will only continue to increase the number of filters and switches inside cellphones, due to the allocation of new frequency bands and expansion of the existing ones. The design and implementation of switch matrixes (switchplexers) and filters for future cellular phones pose significant challenges, as they increase circuit size, complexity, and cost. In order to

reduce the complexity of switchplexers and filters in future radios, design approaches based on employing new materials for filter applications are being investigated.

Filter banks employing intrinsically switchable acoustic resonators based on multifunctional ferroelectric materials, such as barium titanate (BTO), strontium titanate (STO), and BST are considered to address the aforementioned challenges [12], [17], [34]–[36]. Previous work on ladder-type ferroelectric filters includes a demonstration of a BTO FBAR filter [12], a BST SMR filter [35], and a BST-on-Si FBAR filter [36]. These studies demonstrate the capability of ferroelectric materials in the design of intrinsically switchable filters.

This chapter presents a detailed design and fabrication process for multiple types of intrinsically switchable BST filters: (1) in the first section, a 1.5 stage intrinsically switchable ladder-type filter unit cell, based on BST FBARs, with an improved figure of merit (FOM = $K_t^2 \times Q$) [37] is demonstrated. Subsequently, two filter unit cells are connected in series to implement a 2.5 stage filter, enhancing the out-of-band rejection in the ON state and isolation between the input and the output ports in the OFF state. The BST FBAR filters presented here exhibit the lowest reported IL for intrinsically switchable BAW filters to date. (2) The majority of the on-chip RF solutions rely on differential RF signals due to their robustness against the common mode noise and reduced sensitivity to supply voltage fluctuations [38]. Thus, single ended to balanced or balanced to balanced filters are of interest in system integration with ICs. An intrinsically switchable balanced lattice-ladder BST FBAR filter is designed and fabricated for the first time. Due to the high BST relative permittivity, the size of ladder-type BST filters is considerably smaller compared to conventional piezoelectric BAW filters. With acoustically coupled BST

filters, the device footprint can be even further reduced. (3) Furthermore, a realization of ferroelectric BST stacked crystal filters (SCFs) based on the acoustic coupling of two BST transducers, forming a single resonator, is presented. BST SCFs not only provide a sharp filter response and a high out-of-band rejection at a reduced circuit area but also offer a high input to output OFF state isolation level as a result of its small feed-through capacitance. Miniaturized BST filters can significantly simplify RF front-end modules with their inherent switchability.

3.2 Intrinsically Switchable Ladder-type BST Filters

3.2.1 BST FBAR Filter Design

The basic building block of an intrinsically switchable ladder-type filter is a BST resonator (FBAR or SMR). As discussed in the previous chapter, the electrical behavior of intrinsically switchable BST resonators in their ON state is represented by the mBVD

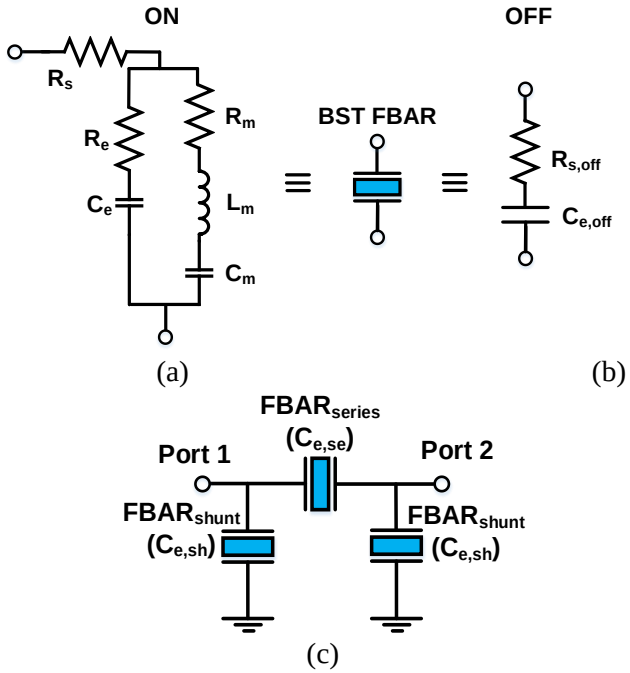

Fig. 3.1 Lumped element circuit model for the BST FBAR in (a) ON and (b) OFF states, and (c) the schematic representation of a 1.5 stage π- network switchable BST FBAR filter unit cell.

model [29], [30], shown in Fig. 3.1 (a). In the OFF state, the BST devices simply behave like a capacitor ($C_{e,off}$ in Fig. 3.1 (b)). Such circuit models are utilized in designing BST band-pass filters and for predicting their ON and OFF response. In this section, a ladder-type BST filter is designed and fabricated in a systematic approach based on the BST FBARs presented in the previous chapter.

A 1.5-stage filter unit cell with a fractional bandwidth (FBW) of $\frac{K_t^2}{2}$% at the filter center frequency ($f_c = \omega_c/2\pi$) of 2 GHz is designed for a system impedance (Z_o) of 50 Ω. The filter unit cell is implemented based on a π-network configuration, shown in Fig. 3.1(c), by following the image parameter method described in [39]. First, the electrical capacitances of the series ($C_{e,se}$) and the shunt ($C_{e,sh}$) BST FBARs in their ON state are determined in order to meet the required design constraints. Then, the structure of the FBARs is designed based on the filter specifications.

The series and shunt FBARs' electrical capacitances are calculated using (3.1) and (3.2) to be $C_{e,se}$ = 0.81 pF and $C_{e,sh}$ = 1.49 pF, respectively:

$$C_{e,se} = \left(\frac{1}{\omega_c Z_o \sqrt{M}}\right) \div \sqrt{\frac{(M-1)^2}{FBW^2 M}\left(1+\sqrt{1+FBW^2}\right)-2} \tag{3.1}$$

$$C_{e,sh} = \left(\frac{1}{2\omega_c Z_o \sqrt{M}}\right) \times \sqrt{\frac{(M-1)^2}{FBW^2 M}\left(1+\sqrt{1+FBW^2}\right)-2}, \tag{3.2}$$

where M is:

$$M = 4 \div \left(1+\sqrt{1-\frac{16K_t^2}{\pi^2}}\right)^2. \tag{3.3}$$

In the next step, BST FBARs are designed to meet the filter specifications. The BST FBAR structure, shown in Fig. 3.2, consists of platinum electrodes, a thin layer of ferroelectric BST ($Ba_{0.5}Sr_{0.5}TiO_3$), and a layer of SiO_2 beneath the bottom electrode. In order to design the thicknesses of each layer for operation at 2 GHz, a 1-D transmission line simulation is performed, as described in the previous chapter. In this simulation, the thickness of SiO_2 diffusion barrier layer is assumed 300 nm, resulting in BST and Pt electrode thickness values of d_{BST} = 770 nm and d_{Pt} = 100 nm, respectively. The resonator is expected to provide a K_t^2 of 6% and FOM of more than 20 based on previous measurements of resonators with similar structure and size. The FOM value here is expected to be smaller than the resonator presented in the previous chapter, due to pronounced fringing field effects associated with the smaller size resonators utilized in the filter structure [40].

Next, the anti-resonance frequency of the shunt FBARs ($f_{a,shunt}$) is set to be identical to the resonance frequency of the series FBARs ($f_{r,series}$) in order to obtain typical band-pass characteristics of a ladder-type filter configuration, where $f_c = f_{a,shunt} = f_{r,series} = 2$ GHz. Therefore, shunt FBARs are mass-loaded with a thin layer of Pt to reduce their resonance frequency, which is calculated using (3.4). The thickness of the required extra Pt layer ($d_{Pt,mass}$) is determined with the 1-D transmission line model to be 14 nm.

$$f_{r,shunt} = \frac{f_{a,shunt}}{2}\left(1+\sqrt{1-\frac{16K_t^2}{\pi^2}}\right) \tag{3.4}$$

Subsequently, the series and the shunt FBAR areas (A_{FBAR}) are calculated by (3.5) to provide the required electrical capacitances:

$$A_{FBAR} = \frac{C_e d_{BST}}{\varepsilon_o \varepsilon_{eff,ON}} \tag{3.5}$$

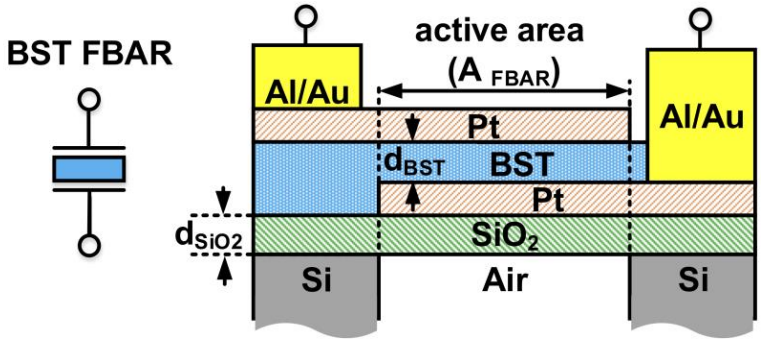

Fig. 3.2 Simplified cross-sectional view of the designed BST FBAR.

Table 3.1
Series and Shunt BST FBARs' Designed Physical Parameters

FBAR	A_{FBAR} $(\mu m)^2$	d_{BST} (nm)	d_{SiO2} (nm)	d_{Pt} (nm)	$d_{Pt,mass}$ (nm)
Series	563	770	300	100	0
Shunt	1037	770	300	100	14

where ε_0 is the permittivity of the free space and $\varepsilon_{eff,ON}$ is the relative permittivity of BST when the FBAR is turned on ($\varepsilon_{eff,ON}$ ~ 125 at 60 V DC). All the calculated physical parameters for the BST FBARs are summarized in Table 3.1.

3.2.2 BST Filter Implementation and Simulation

The schematic of the filter unit cell is shown in Fig. 3.3. The series FBAR is replaced by two FBARs, each with twice the original area, to simplify the DC-biasing network. This is also expected to enhance the linearity and power handling of the filter [30], [41]. In this configuration, control of all the FBARs is handled through applying DC-bias voltages at the input and output ports. In Fig. 3.3, R_{bias} represents a high resistivity DC-biasing line connected to the ground.

The complete resonators' parameters used in filter simulations are provided in Table 3.2. The mBVD model parameters for the series and the shunt FBARs are calculated based on these parameters using (3.6)-(3.8). In order to simulate the OFF state isolation response of the BST FBAR filter, the mBVD model for the resonators is replaced with their OFF state capacitive model shown in Fig. 3.1(b). OFF state capacitances ($C_{e,off,se}$ and $C_{e,off,sh}$ under zero DC bias voltage) are estimated to be twice the ON state capacitances ($C_{e,se}$ and $C_{e,sh}$ at V_{dc}=60 V) based on the measurement results for the 1-port BST FBARs. In the filter simulations, the resonator series resistance (R_s) and BST loss tangent are determined

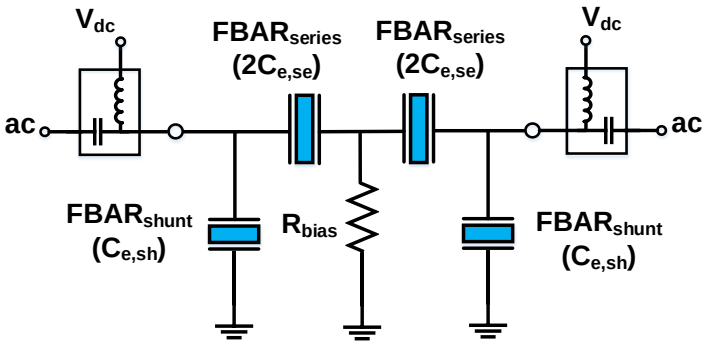

Fig. 3.3 Schematic of the 1.5 stage BST FBAR filter unit cell. The filter is turned on by applying DC-voltages through the input and output ports with two bias tees in the RF path.

Table 3.2
Series and Shunt BST FBARs' Parameters Used for the Filter Simulations

FBAR	f_r *(GHz)*	f_a *(GHz)*	K_t^2 *(%)*	Q_m
Series	2.00	2.05	6	350
Shunt	1.95	2.00	6	350

to be 1.5 Ω and 0.02, respectively, both obtained based on l-port BST FBARs measurements.

$$C_m = C_e\left[\left(\frac{f_a}{f_r}\right)^2 - 1\right] \tag{3.6}$$

$$L_m = \frac{1}{C_m(2\pi f_r)^2} \tag{3.7}$$

$$R_m = \frac{2\pi f_r L_m}{Q_m} \tag{3.8}$$

Advanced Design System (ADS) software is used to simulate the 1.5 stage BST FBAR filter unit cell. Its simulated transmission and reflection responses in ON and OFF states

are provided in Fig. 3.4. The filter minimum IL and FBW are 1.5 dB and 3%, respectively, at the filter center frequency of 2 GHz, and it provides more than 13 dB of isolation between the input and output ports in its OFF state.

A 2.5 stage filter, shown in Fig. 3.5, is implemented by cascading two 1.5 stage BST FBAR filter unit cells. An additional high resistivity line is added for biasing the center

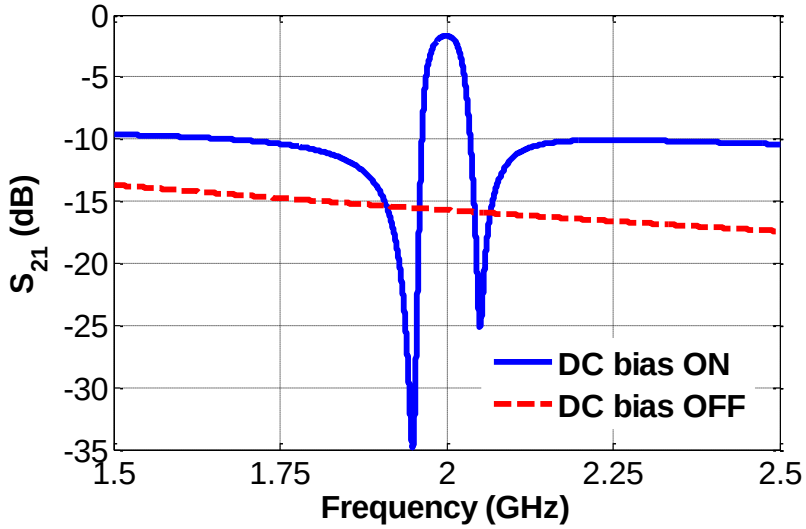

(a)

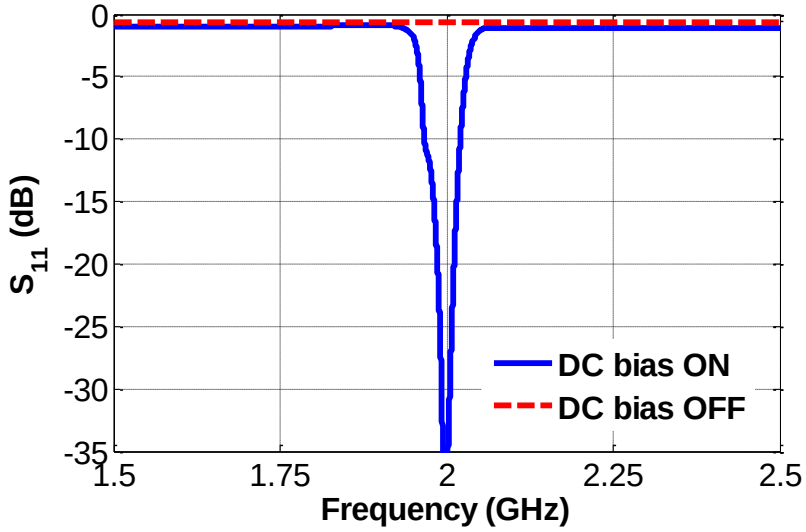

(b)

Fig. 3.4 (a) Transmission and (b) reflection responses for the simulated 1.5 stage BST FBAR filter.

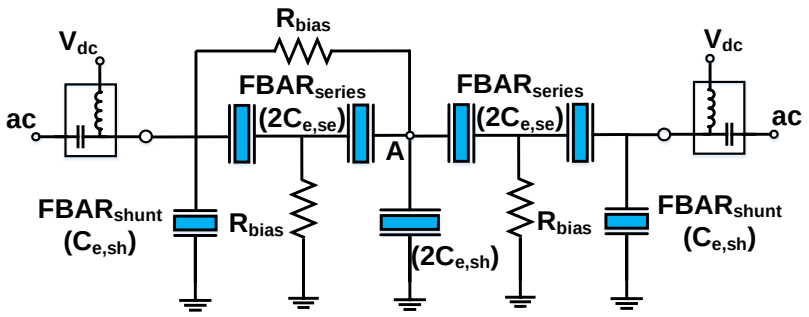

Fig. 3.5 Schematic of the 2.5 stage BST FBAR filter.

node (A). As shown in Fig. 3.5, all the BST FBARs can be turned on only by applying DC-bias voltages through the input and the output ports. Simulation results for transmission and reflection of the 2.5 stage BST FBAR filter in both states are plotted in Fig. 3.6. Based on the simulation results, the filter provides an out-of-band rejection and isolation greater than 25 dB. The minimum insertion loss and the filter FBW are expected to be 3 dB and 2.6% at 2 GHz, respectively.

3.2.3 Filter Fabrication Process and Measurement Setup

Intrinsically switchable ladder-type BST FBAR filters are fabricated using a process described in chapter 2. Additional steps include the deposition of a 50 nm of NiChrome to form the DC biasing network and 14 nm-thick Pt, used for mass loading of the shunt resonators. Both layers are deposited and patterned by evaporation and lift-off. The thickness values for each layer in the BST FBARs' structure are measured using a Dektak stylus profilometer and listed in Table 3.3. The measured thicknesses are close to the values designed in the previous section.

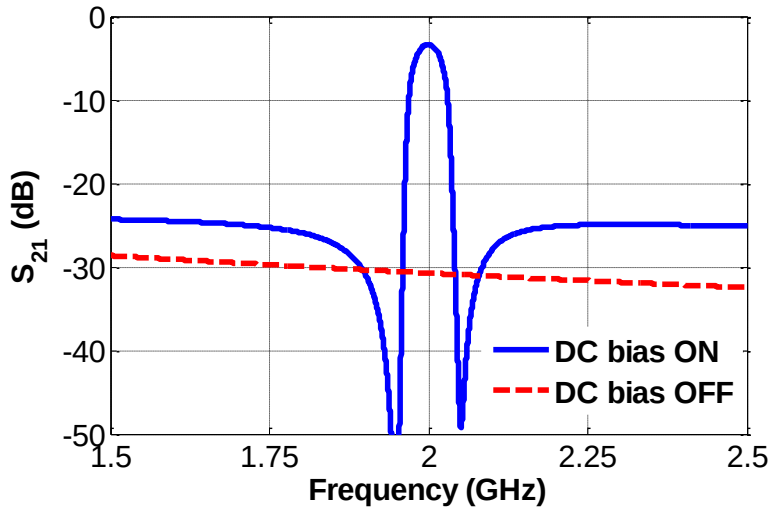

(a)

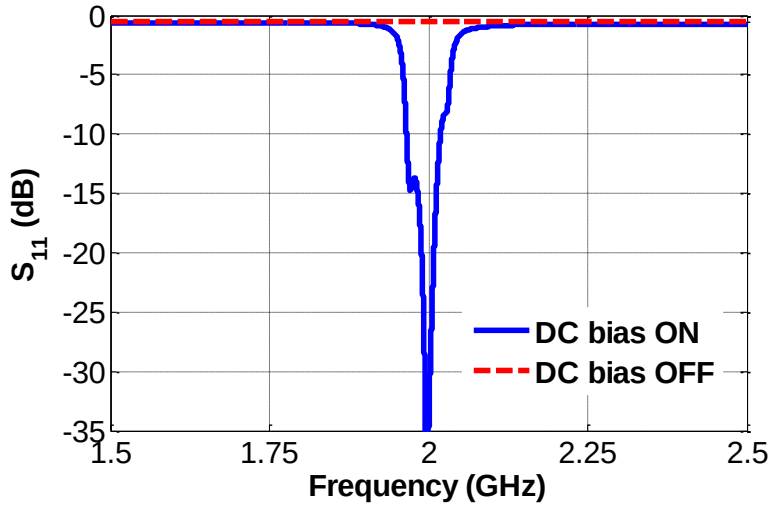

(b)

Fig. 3.6 Simulation results for (a) transmission and (b) reflection of the 2.5 stage BST FBAR filter. The out-of-band rejection and isolation level are more than 25 dB.

Device S-parameters are measured using a Keysight network analyzer and a Cascade Microtech probe station with ground-signal-ground (GSG) probes of 250 µm pitch size. Short-open-load-through (SOLT) calibration is done for a system impedance of 50 Ω. DC-bias voltages are applied through the bias tees connected to each probe. Finally, S-parameters for the BST FBAR and filters in ON (at 60 V DC) and OFF (no DC-bias applied) states are measured.

Table 3.3
Measured Thickness Values for the Deposited Films

Layers	**1.5 stage**	**2.5 stage**
Top Pt (nm)	94	94
BST (nm)	750	710
Bottom Pt (nm)	95	95
SiO_2 (nm)	280	280

3.2.4 Measurement Results and Discussion

The photograph of a fabricated BST FBAR is shown in Fig. 3.7(a). The size of the resonator's active area is 38 μm × 38 μm. As shown in the figure, two small window openings are used to release the BST FBAR membrane by XeF_2 gas. The measured S_{11} of the fabricated BST FBAR in both ON (60 V) and OFF (0 V) states are provided in Fig.

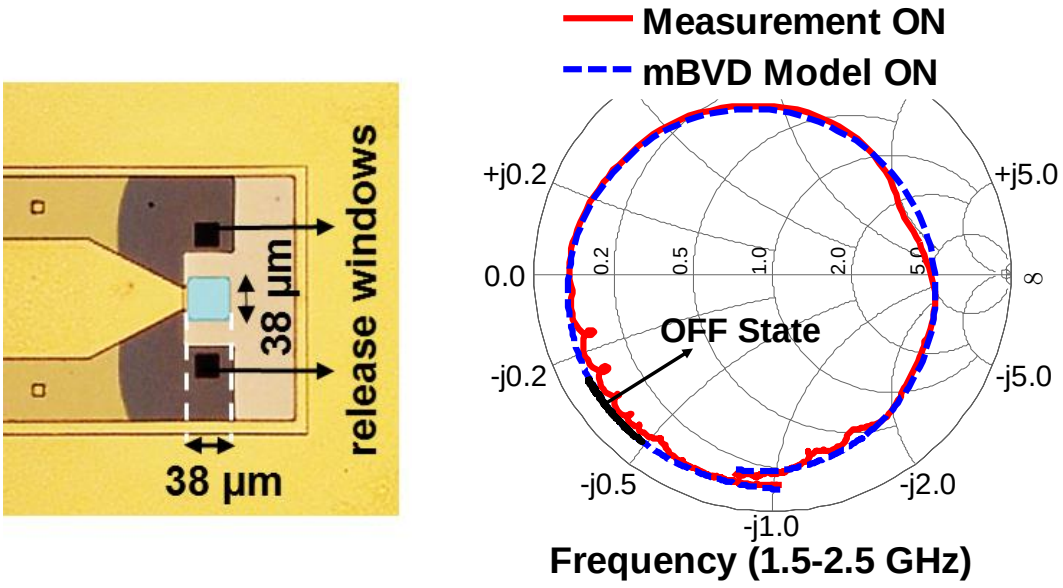

(a) (b)

Fig. 3.7 (a) Photograph of a fabricated BST FBAR and (b) its measured S_{11} plotted on Smith chart in its ON (60 V) and OFF states (0 V). The S_{11} for the lumped element mBVD model of the resonator is also plotted with a dashed line.

3.7(b). In its OFF state, the resonator behaves like a capacitor, where its S_{11} is shown by a solid black line in the figure. Applying a DC bias voltage across the resonator electrodes induces piezoelectricity in the BST layer, thereby turning ON the resonator. The measured device resonance and anti-resonance frequencies are 2.11 GHz and 2.17 GHz, respectively. The extracted lumped element mBVD model parameters for the measured BST FBAR are provided in Table 3.4. The S_{11} of the mBVD model is also plotted in Fig. 3.7(b) by a dashed line, showing the accuracy of the model. Based on this model, K_t^2, Q_m, Q_r, and Q_a are calculated using (2.6) and (2.7) to be 6.6%, 340, 166, and 140, respectively. The figure of merit ($Q_m \times K_t^2$) for this resonator is calculated to be 22. The resonator parameters are summarized in Table 3.5.

Photographs of the fabricated 1.5 and 2.5-stage BST FBAR filters are shown in Fig. 3.8. The 1.5-stage filter unit cell consists of two series and two shunt FBARs, while the

Table 3.4
mBVD Model Parameters

Parameter	**Value**	**Parameter**	**Value**
L_m (nH)	51.3	R_e (Ω)	3
R_m (Ω)	2	R_s (Ω)	2.1
C_m (pF)	0.11	L_s (nH)	0.07
C_e (pF)	1.84		

Table 3.5
BST FBARs' Measured Characteristics

Parameter	f_r **(GHz)**	f_a **(GHz)**	K_t^2 **(%)**	Q_m	$Q_m \times K_t^2$
Value	2.11	2.17	6.6	340	22

2.5-stage filter is made of four series and three shunt FBARs. The BST filter unit cell footprint size is 80 µm × 110 µm, which is comparably smaller than the size of conventional FBAR filters.

Measurement results for the fabricated 1.5-stage BST filter are presented in Fig. 3.9. In its ON state, a band-pass response with a 3-dB bandwidth of 58 MHz (FBW = 2.8%) at the center frequency of f_c = 2.08 GHz is observed. The minimum IL for this filter is 2.25 dB, and the return loss is larger than 20 dB within the bandwidth. The out-of-band rejection is 11.5 dB in its ON state. When the DC bias voltage is removed, the filter is turned off, providing more than 13 dB of isolation between the input and the output ports. The response of the simulated filter based on the measured BST, Pt, and oxide thickness values from Table 3.3 is also provided for comparison in Fig. 3.9.

Measurement results for the 2.5-stage BST FBAR filter are shown in Fig. 3.10. The minimum out-of-band rejection is more than 25 dB when the filter is in its ON state,

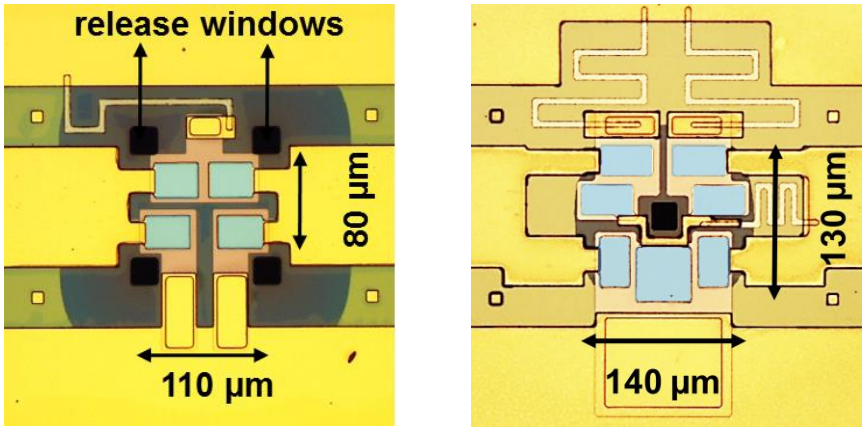

(a) (b)

Fig. 3.8 Photographs of (a) the 1.5 stage and (b) 2.5 stage π-network BST FBAR filters.

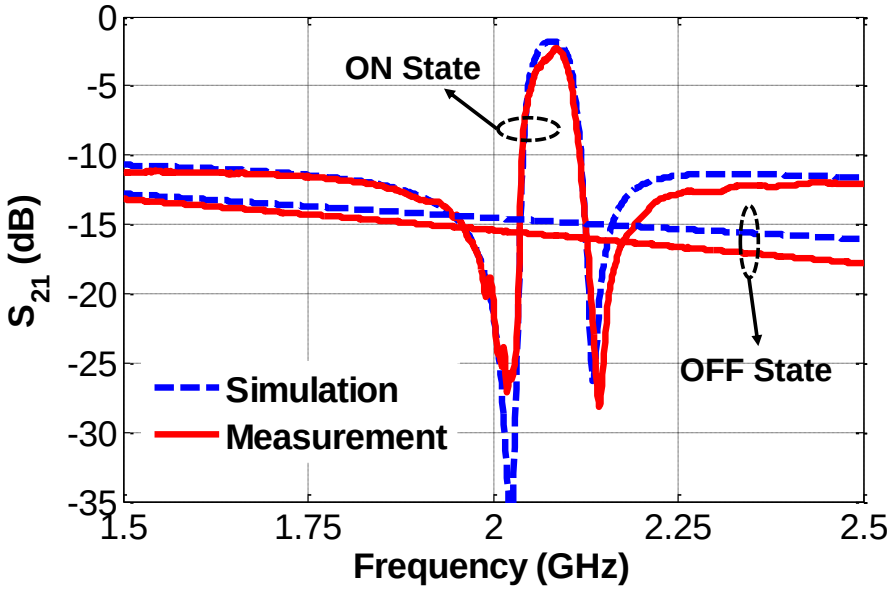

(a)

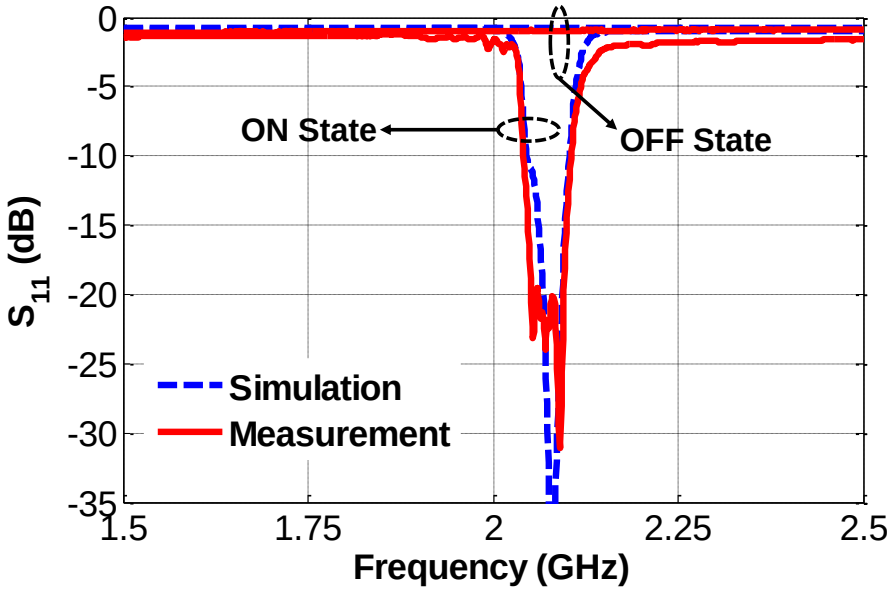

(b)

Fig. 3.9 (a) Transmission and (b) reflection responses for the measured (solid line) and simulated (dashed line) 1.5 stage BST FBAR filter unit cell in its ON and OFF states.

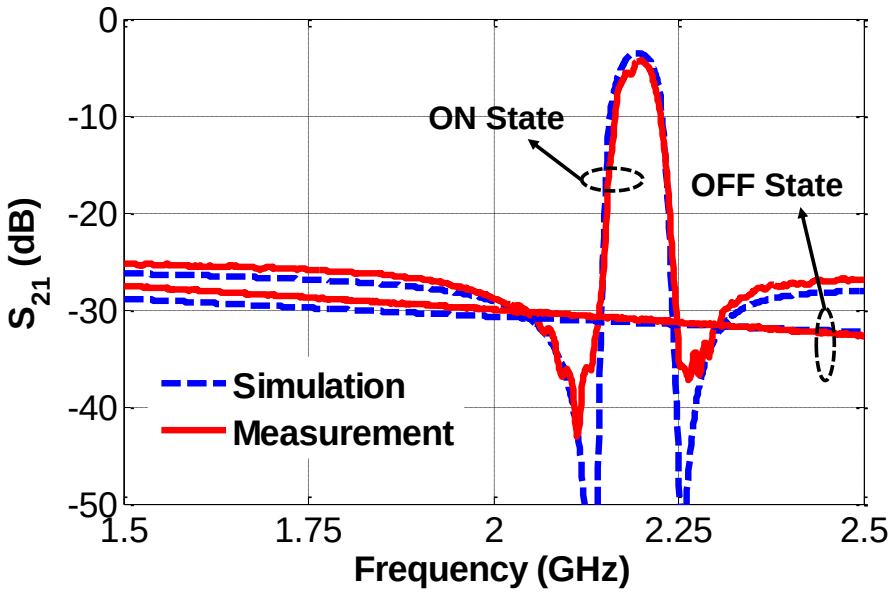

(a)

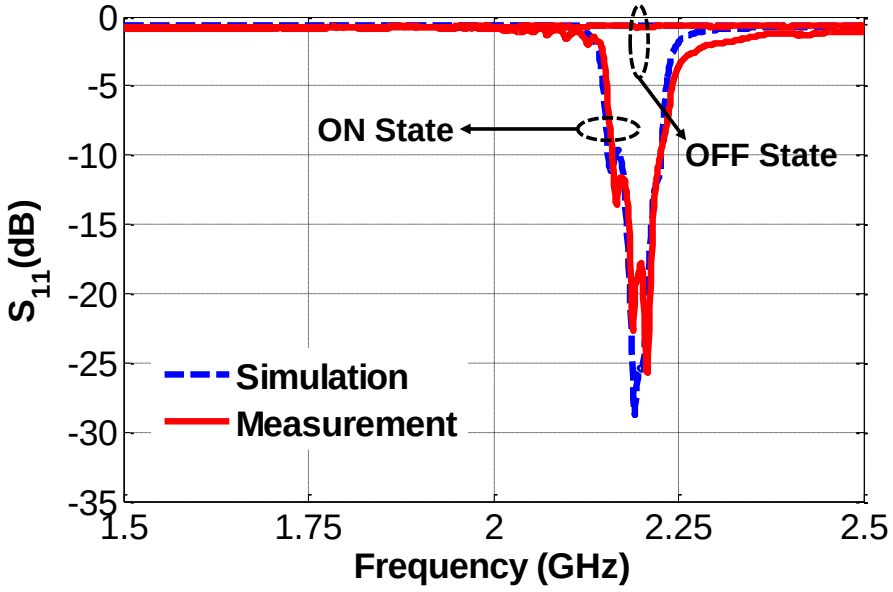

(b)

Fig. 3.10 (a) Transmission and (b) reflection responses for the measured (solid line) and simulated (dashed line) 2.5 stage BST FBAR filter in its ON and OFF states. Minimum rejection level and isolation are more than 25 dB.

providing an improvement of 12 dB as compared to 1.5 stage filter. Turning off the filter leads to isolation of more than 28 dB between the input and the output ports. The filter exhibits a minimum insertion loss of 4.3 dB and 3-dB bandwidth of 55 MHz at 2.2 GHz (FBW=2.5%) in its ON state.

The linearity of the 2.5 stage BST FBAR filter is investigated through IP_3 measurements. Two tones of the same power (Δf = 10 MHz) within the filter passband are transmitted through the filter in its ON state, and the output signal is fed into a spectrum analyzer, similar to the measurement setup of Fig. 2.9. Finally, the signal power at the fundamental frequencies, along with the third-order intermodulation products, is recorded. The measured input third-order intercept point (IIP_3) for the filter is 47 dBm, which is shown in Fig. 3.11. For comparison, IIP_3 of several AlN filters are reported in [42], [43]. The BST filter linearity can be further enhanced by replacing each BST FBAR with multiple series-connected larger BST FBARs, as shown in the previous chapter.

Measurement results for the 1.5 and 2.5-stage BST FBAR filters, provided in Fig. 3.9 and 3.10, are in good agreement with the simulation results. The small discrepancy in the filter center frequency can be attributed to the thickness variation of the deposited films. The difference in the minimum insertion loss is speculated to be due to several factors: the loss of the interconnects between the resonators, lower biasing-line resistance than expected, and the spurious lateral modes in the rectangular shape FBARs. The measured filters' specifications are summarized in Table 3.6. The presented 1.5 and 2.5-stage switchable FBAR filters demonstrated in this work have the lowest minimum insertion loss in comparison with previously reported switchable ferroelectric BAW filters. The

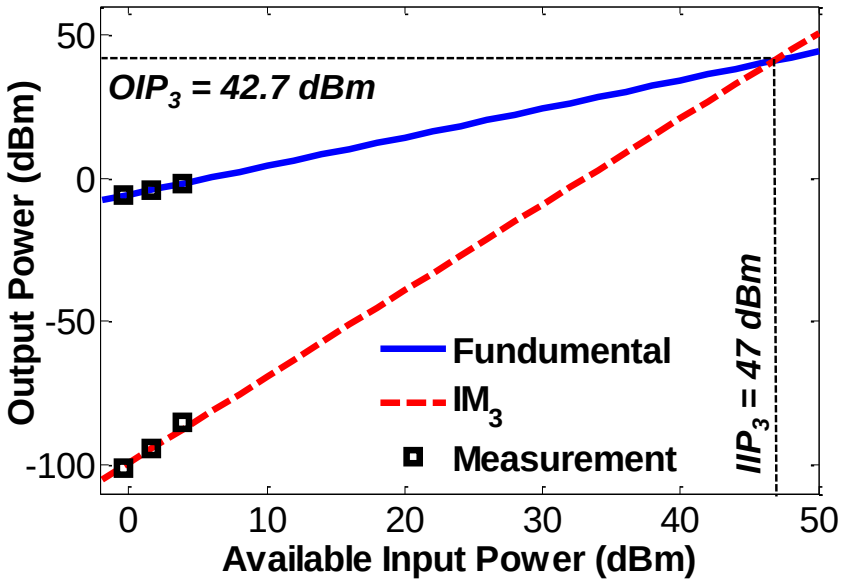

Fig. 3.11 Measured IP_3 data for a 2.5 stage BST FBAR filter.

Table 3.6
Measured Filters' Specifications for the Fabricated 1.5 and 2.5 Stage FBAR Filters

BAW Filter	Minimum IL (dB)	BW (MHz)	Isolation (dB)	Rejection (dB)
1.5-stage	2.25	58	14	11.5
2.5-stage	4.3	50	>28	>25

intrinsically switchable filters are the building blocks for multi-band switchless filter banks.

3.3 Intrinsically Switchable Balanced Filters

3.3.1 Balanced BST FBAR Filter Design and Simulation

RF front-end configuration in today's mobile devices has become extremely complex; hence the cellphone manufacturers have tried to address this by using integrated RF front-end modules that contain acoustic wave filters and amplifiers. The majority of the on-chip RF solutions rely on differential RF signals due to their robustness against the common mode noise and reduced sensitivity to supply voltage fluctuations. [38] Thus, single-ended

to balanced or balanced to balanced filters are of interest in system integration with ICs. Balanced filters based on bulk acoustic wave (BAW) resonators either use ladder or lattice networks, as shown in Fig.3.12 (a) and (b). Single-stage lattice-type filters can achieve an excellent stopband attenuation, while their roll-off is not as steep as a ladder-type filter. By combining a lattice stage with a balanced ladder stage (lattice-ladder structure, as shown in Fig. 3. 12 (c)), one can achieve a high out-of-band and near-in rejection simultaneously [30]. In this section, an intrinsically switchable balanced lattice-ladder BST FBAR filter is designed and fabricated for the first time.

A balanced ladder-type, as well as a lattice-type BST FBAR filter, are designed for a 50 Ω system impedance at 2 GHz with a fractional bandwidth of 3%. The electrical capacitance of both filters are designed through the image parameter method by using (3.9) and (3.10), given the electromechanical coupling coefficient (K_t^2) of resonators, the system impedance (Z_0), the filter center frequency (f_c), and the fractional bandwidth of the filter (Δ).

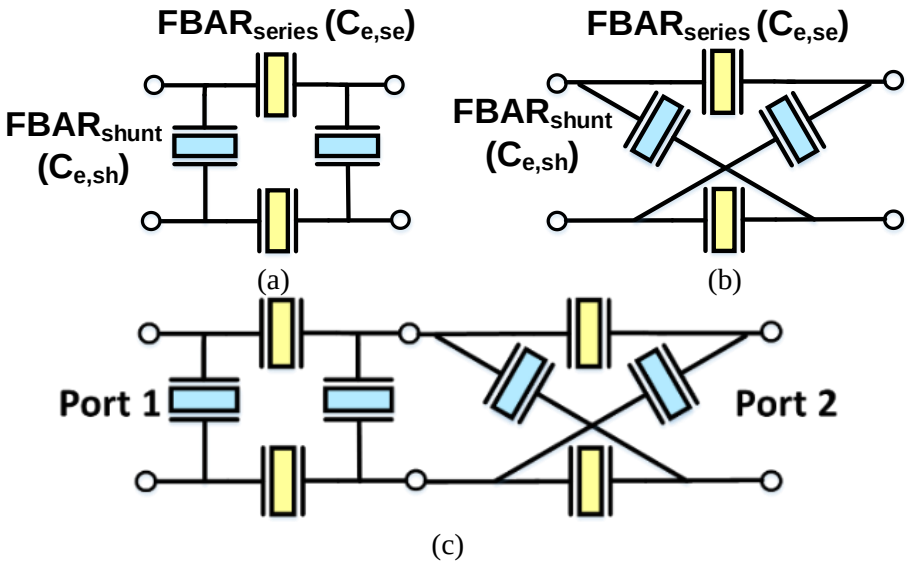

Fig. 3.12 Balanced filter schematics: (a) ladder-type, (b) lattice-type, and (c) ladder-lattice structure.

$$C_{e,s} = \left(\frac{2}{\omega_c Z_0 \sqrt{M}}\right) \times \sqrt{\frac{(M-1)^2}{\Delta^2 M}\left(1+\sqrt{1+\Delta^2}\right)-2} \quad (3\text{-}9)$$

$$C_{e,sh} = \left(\frac{1}{2\omega_c Z_0 \sqrt{M}}\right) \div \sqrt{\frac{(M-1)^2}{\Delta^2 M}\left(1+\sqrt{1+\Delta^2}\right)-2} \quad (3\text{-}10)$$

Where M is given by:

$$M = 4 \div \left(1+\sqrt{1-\frac{16K_t^2}{\pi^2}}\right)^2 \quad (3\text{-}11)$$

The above formulas can be derived following the method described in [39]. The calculated capacitance of the series ($C_{e,s}$) and shunt ($C_{e,sh}$) BST FBARs are 1.6 pF and 1.5 pF, respectively. In these calculations the BST FBAR nominal K_t^2 is assumed to be 6% similar to the previous section. The BST FBARs are constructed of a thin layer of ferroelectric BST ($Ba_{0.5}Sr_{0.5}TiO_3$) sandwiched between platinum electrodes, and a layer of SiO_2 beneath the bottom electrode, as shown in Fig. 3.2. The thickness of BST, Pt electrodes, and oxide layers is designed through 1-D transmission line simulations to be d_{BST} = 770 nm. d_{Pt} = 100, and d_{SiO2} = 300 nm, as described in the previous chapter. Subsequently, the series and the shunt FBAR areas (A_{FBAR}) are calculated by (3.5) to provide the required electrical capacitances.

The 1.5-stage ladder-type and 2–pole lattice-type filters are connected in series to form a balanced ladder-lattice filter. In order to bias all the resonators in the filter, some of the resonators are replaced with two cascaded series resonators having twice the capacitance of a single resonator. The schematic of the ladder-lattice filter with its biasing circuitry is shown in Fig. 3.13. The mBVD model parameters, as discussed in chapter 2, for the series and the shunt FBARs are employed to simulate the filters, using ADS software. The simulated transmission and reflection responses of each section, including the 1.5-stage ladder and 2-pole lattice filters, as well as the entire ladder-lattice BST FBAR filter, are

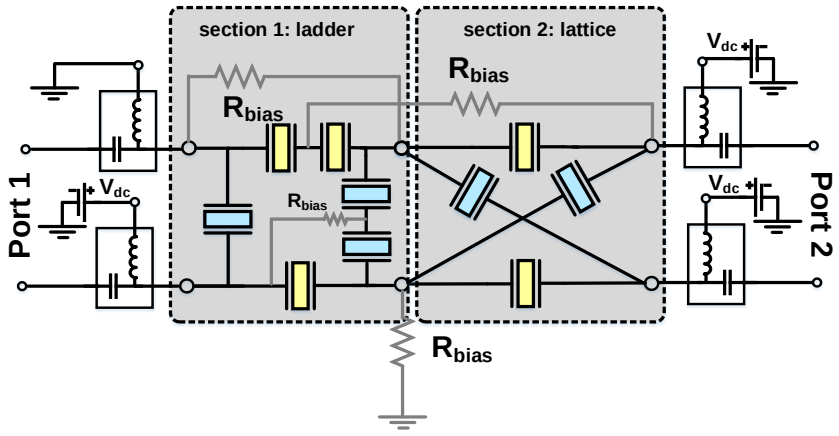

Fig. 3.13 Schematic of the BST FBAR ladder-lattice balanced filter along with its biasing circuitry.

provided in Fig. 3.14 (a), (b), and (c), respectively. The OFF-state isolation response of the filters is also plotted on the same figures. The resonators in Fig. 3.13 are replaced with their equivalent capacitance under zero bias voltage to model their OFF-state response.

Based on the simulation results, the first section of the filter, a 1.5-stage ladder, provides a 10 dB out-of-band-rejection with transmission zeros close to the filter center frequency. While the second section, i.e., the 2-pole lattice, provides an out-of-band-rejection and isolation of greater than 30 dB. Consequently, the combined lattice-ladder filter exhibits a high out-of-band-rejection of more than 40 dB with a steep roll-off. The filter minimum insertion loss and FBW are expected to be 3.5 dB and 2.6% at 2 GHz, respectively. The device exhibits a large isolation of more than 40 dB between the input and the output ports in its OFF state when no DC bias voltage is applied to the resonators.

3.3.2 Experimental Results for Balanced BST FBAR Filters

The intrinsically switchable ladder-lattice BST FBAR filter is fabricated following the steps described in chapter 2. Each section of the filter is also fabricated separately to further investigate its performance. Photographs of the fabricated filters are shown in the inset of

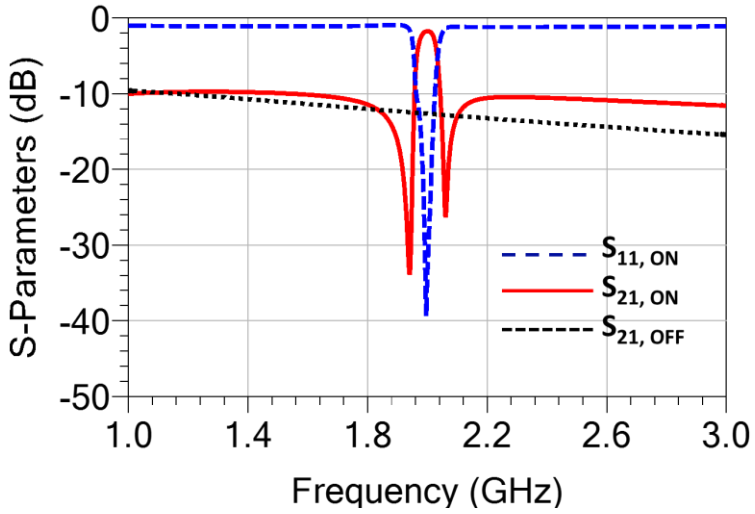

(a)

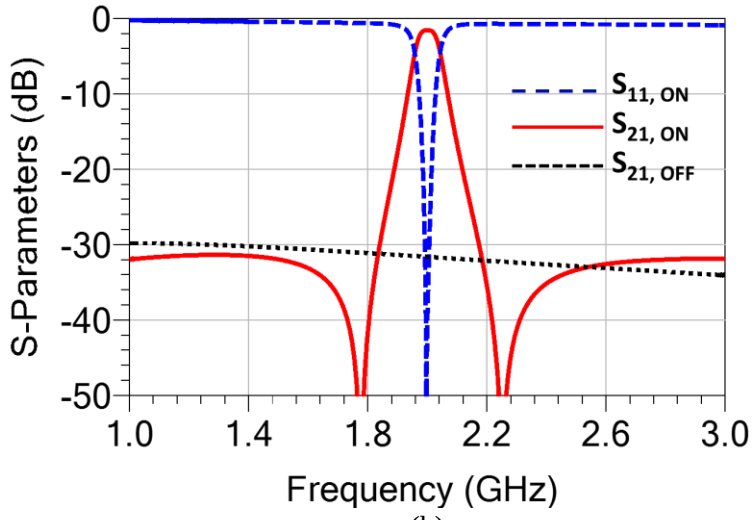

(b)

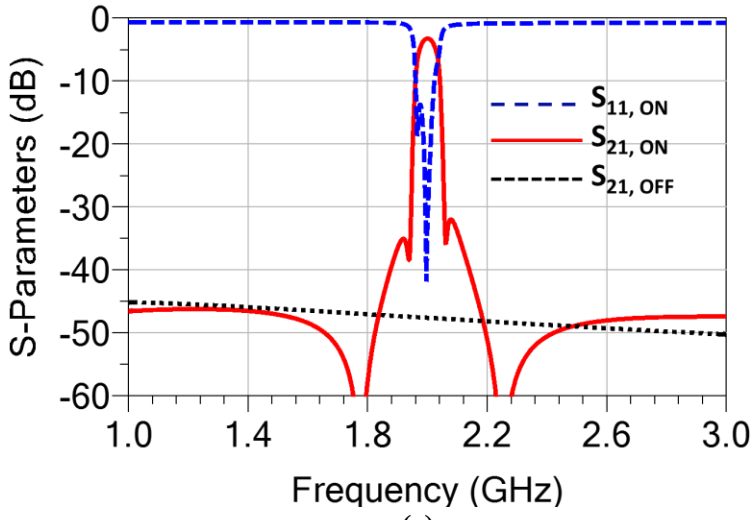

(c)

Fig. 3.14 S-parameters of the simulated (a) ladder, (b) lattice, (c) ladder-lattice filters in ON state. Their OFF-state transmission response is also provided in a dotted black line.

Fig. 3.15. Due to the BST's large relative permittivity, the size of the ladder-lattice BST FBAR filter active area is only 270 μm × 140 μm. The filters S-parameters are measured using a four-port Keysight vector network analyzer and a Cascade Microtech probe station with ground-signal-ground-signal-ground (GSGSG) probes of 150 μm pitch size. Short-open-load-through (SOLT) calibration is conducted for a system impedance of 50 Ω. DC-bias voltages are applied through bias tees connected to all four ports. Finally, S-parameters for the BST FBAR filters in their ON (at 70 V DC) and OFF (no DC-bias applied) states are measured. In order to convert single-ended measurement data into the differential, mixed-mode S-parameters are then calculated. The transmission (S_{dd21}) and reflection (S_{dd11}) responses of all three filters are plotted in the ON state, as shown in Fig. 3.15. The OFF state transmission response is also provided in the same figures.

As expected, the balanced ladder structure provides a steep near in rejection, as shown in Fig 3.15 (a), while the lattice structure provides a high out of band rejection as well as a high OFF state isolation level between the two ports (Fig 3.15 (b)). The combined ladder-lattice BST FBAR filter, however, exhibits a high out-of-band rejection of more than 35 dB across the measured frequency band as well as a sharp roll-off. Most importantly, such a filter provides a high OFF state isolation level of more than 40 dB that reduces the number of required filtering stages. The minimum insertion loss and 3-dB fractional bandwidth of the ladder-lattice BST FBAR filter are measured to be 6.2 dB and 3%, respectively. In general, the measurement results for the balanced BST FBAR filters, provided in Fig. 3.15, are in good agreement with the simulation results. The discrepancy in minimum insertion loss is attributed to the loss of the interconnects between the resonators (more specifically, the resonators in the lattice structure) and lower biasing-line resistance than expected in

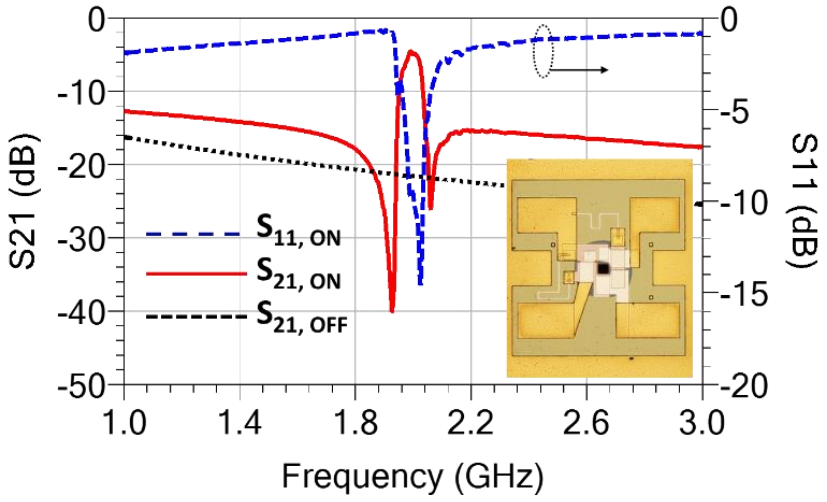

(a)

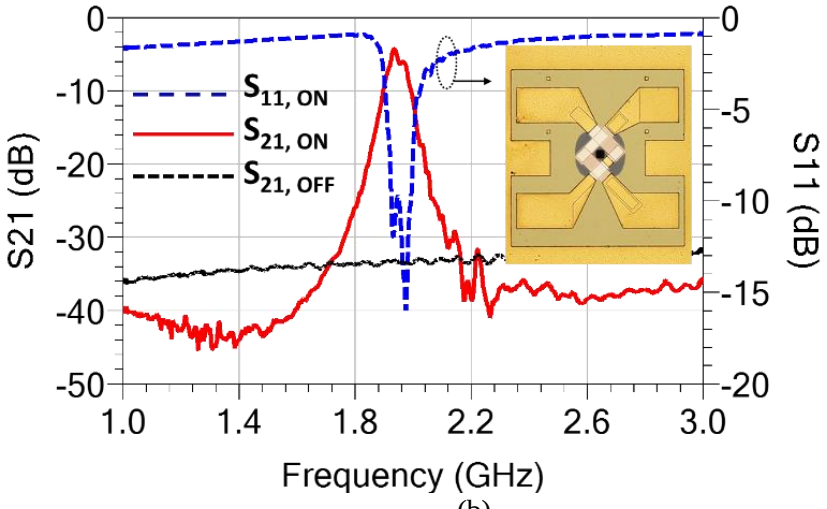

(b)

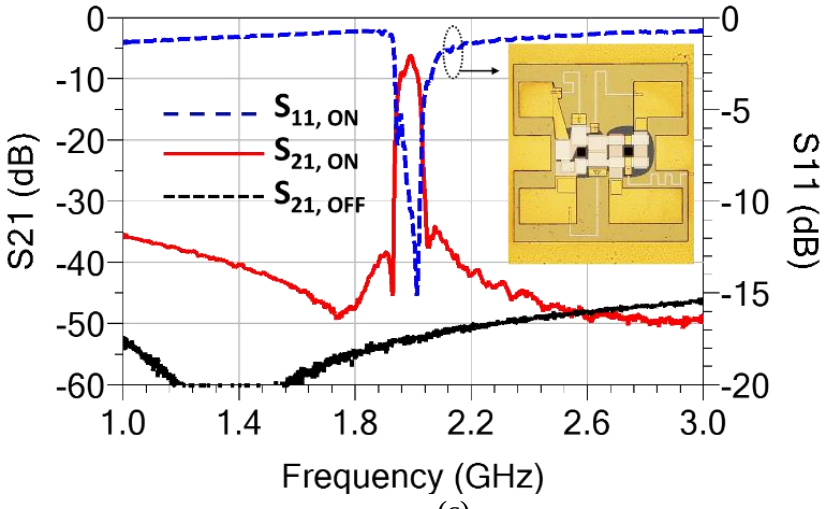

(c)

Fig. 3.15 Measured transmission and reflection response of the BST FBAR (a) ladder, (b) lattice, and (c) ladder-lattice filters, respectively. The OFF state isolation response is also provided for the three filters in a black dotted line.

ladder structure. This work represents the first demonstration of the intrinsically switchable balanced ferroelectric BAW filters.

3.4 Intrinsically Switchable Ferroelectric Stacked Crystal Filters

3.4.1 BST SCF Structure and Design

Stacked crystal filters are composed of multiple transduction and metal layers, as shown in Fig. 3.16 [30], [44]–[46]. The single-pole SCF of Fig. 3.16 is formed from two transducers vertically stacked on top of each other, creating one thickness mode resonator. Under an RF excitation, the signal applied between the top electrode and ground electromechanically excites the input transducer, which then couples acoustic energy to the bottom transducer.

By employing ferroelectric BST and its voltage-dependent piezoelectricity as a transduction layer in this structure, the SCF can also be turned on and off with a DC bias voltage applied across the electrodes. The resonator of Fig. 3.16 supports a fundamental mode of resonance, where there is a half-wavelength standing wave across the entire structure (mode 1), along with other higher-order modes. For the most efficient transduction, largest electromechanical coupling coefficient, and widest bandwidth,

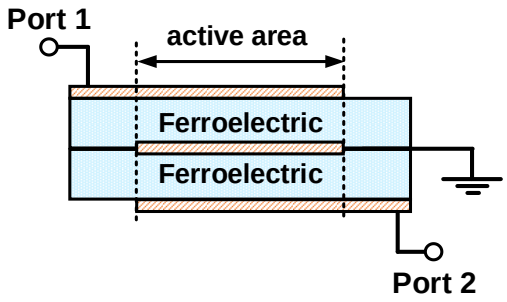

Fig. 3.16 A single pole ferroelectric stacked crystal filter configuration.

however, the SCF in this work is designed to operate in mode 2, where there is a half wavelength standing acoustic wave across each transducer [45].

The simplified lumped element model for the BST SCF in the ON and OFF states are shown in Fig. 3.17. Unlike a standard FBAR, the lumped element model for an SCF filter does not have a parallel resonance, as the SCF does not have an electrical capacitance directly in shunt to the motional branch. Hence, the response of the SCF is determined solely by the acoustic branch and its associated series loss. Without any DC bias, the resonator is off, and the model simplifies by excluding the motional branch, as shown in Fig. 3.17 (b). The parasitic capacitance C_f represents the stray capacitance between the input and output ports, which should be as low as possible. Due to the low stray capacitance between the input and output ports in this structure, a BST SCF is capable of providing high isolation between the ports in its OFF state.

It has been shown that when the reactance of the electrical capacitance ($1/(\omega C_e)$) is equivalent to the device input and output impedances at the designed frequency, the SCF exhibits its minimum insertion loss and maximum bandwidth [45]. Accordingly, a mode 2 BST SCF is designed for a 50 Ω system impedance at 3.6 GHz. The thickness of each layer

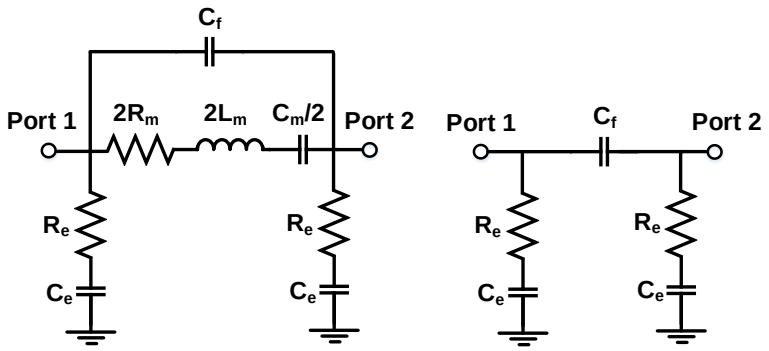

Fig. 3.17 Lumped element model for a single pole stacked crystal filter in its (a) ON and (b) OFF states.

of the structure is designed with the 1-D acoustic wave transmission line model [17], [47]. In this model, the thickness of the Pt electrodes is set to 100 nm, and a 100 nm-thick SiO_2 diffusion barrier layer is also used underneath the bottom electrode. The finalized thickness of all the layers in the BST SCF design is summarized in Table 3.7. The calculated C_e value for a 50 Ω system is 0.88 pF, and the remainder of the lumped element model component values are established through (3.6)-(3.8), as shown in Table 3.8. Mechanical and electrical quality factors are set as Q_m = 300, and Q_e = 50, from [37]. Finally, through full-wave simulation of the total structure in HFSS, the expected value of the stray capacitance between the coupled ports is also obtained.

Table 3.7
The thickness of the Layers in The BST SCF Structure

Device	**Thickness (nm)**
Pt: top electrode	100
BST: top transducer	370
Pt: middle electrode	100
BST: bottom transducer	370
Pt: bottom electrode	100
SiO_2: diffusion barrier layer	100

Table 3.8
BST SCF Lumped Element Model Parameters

Parameter	**Value**	**Parameter**	**Value**
L_m (nH)	28.4	R_e (Ω)	1
R_m (Ω)	2.1	R_s (Ω)	2
C_m (fF)	70.7	C_f (fF)	19
C_e (pF)	0.88		

The BST based SCF with parameters listed in Table 3.8 is simulated in the ADS, and simulation results for the transmission and reflection responses in both the ON and OFF states are displayed in Fig. 3.18. As shown in the figure, the filter is expected to provide a minimum insertion loss (IL) and 3-dB bandwidth (BW) of 1.3 dB and 148 MHz, respectively, while also providing an isolation level greater than 30 dB in the OFF state.

3.4.2 Experimental Results for BST based SCF

The BST based SCF is fabricated following a process similar to [48], and a photograph of the fabricated device, as well as a simplified cross-sectional view, is provided in Fig. 3.19. The active area of the fabricated BST SCF occupies only 19 μm × 19 μm, due to the large permittivity of BST and the vertical structure of stacked crystal filters. DC bias voltages are applied through bias tees connected at the input and the output ports of the filter. The measured transmission and reflection responses of the filter in its ON and OFF states are displayed in Fig 3.20.

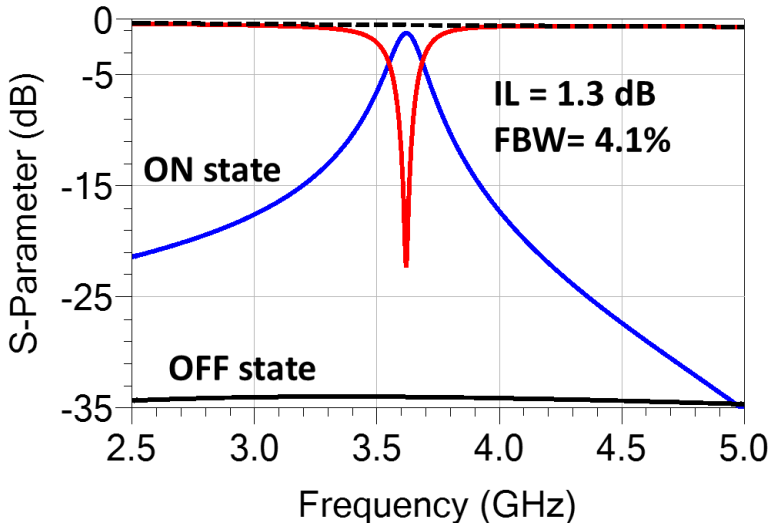

Fig. 3.18 Simulated S-parameters of the single pole intrinsically switchable BST SCF.

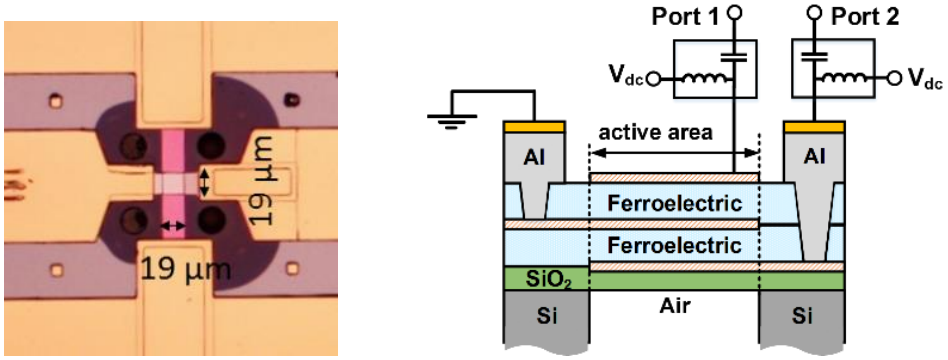

(a) (b)

Fig. 3.19 (a) A photograph of the fabricated single pole BST SCF and (b) corresponding cross-sectional view of the design.

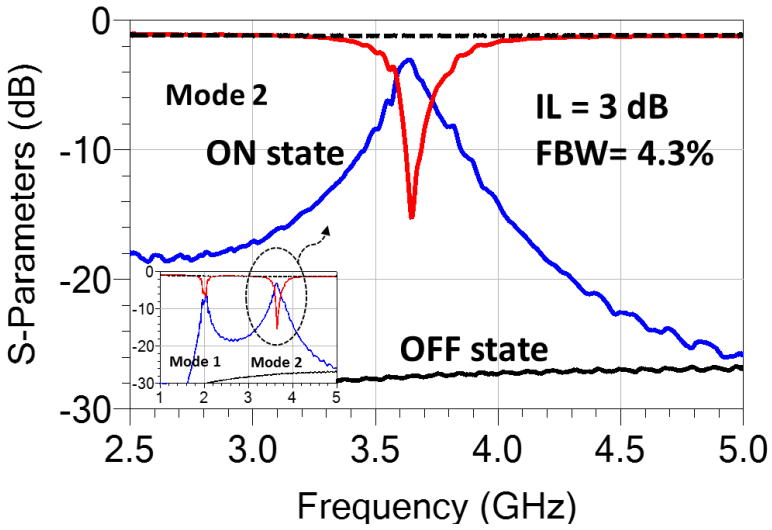

Fig. 3.20 Measured S-parameters of the intrinsically switchable BST SCF. The inset shows the response of filter over a wider range of frequency, which includes mode 1 and 2. In this paper, the device is optimized for the mode 2 operation.

As expected, the BST SCF provides a high out-of-band rejection and OFF state isolation between the input and the output ports with a small form factor. The IL and 3-dB BW of the filter are measured to be 3 dB and 158 MHz, respectively, at a center frequency of 3.6 GHz (4.3 % FBW). Compared with the simulation results, the minimum insertion loss of the BST SCF increased by 1.7 dB. This is attributed to the larger than expected mechanical and electrical losses. For reference, the mechanical quality factor of the resonator is measured to be 180 versus the simulated value of 300. The series resistance is

measured to be 7 Ω rather than the expected value of 2 Ω, which is speculated to be due to the large step at the top electrode lead area. This can be reduced by optimizing the device layout to cover the step with a thicker metal layer or using a sputter deposited top electrode for better step coverage. Furthermore, misalignment during the lithography process for the platinum electrodes created unwanted active regions with slightly thinner thicknesses, leading to excitation of spurious resonances that cause additional losses. The IL and the BW of the BST SCF can be further extended through inductor tuning or introducing an additional coupling layer between the two resonators, as described in [30].

The work described herein is the first demonstration of an intrinsically switchable stacked crystal filter. Taking advantage of the stacked crystal filter's characteristics, a hybrid structure combining both a BST SCF with a standard ladder-type filter can also be implemented to improve the overall filter response. The near-in selectivity of the filter improves with a ladder-type filter, while also maintaining the high out-of-band rejection and OFF state isolation of BST SCF.

3.5 Chapter Conclusion

A variety of intrinsically switchable acoustic wave filters based on BST have been developed and presented in this chapter. Reduced loss intrinsically switchable FBAR filters based on ferroelectric BST have been designed and fabricated in a systematic approach, using the BST FBARs with a relatively high $Q_m \times K_t^2$. Minimum IL of 2.25 dB for a 1.5 stage ladder-type BST filter unit cell with 58 MHz bandwidth at 2.08 GHz has been achieved. Two 1.5-stage filter unit cells are cascaded to implement a 2.5-stage switchable FBAR filter. Minimum rejection level and isolation of more than 25 dB have been

obtained. The IIP_3 for the filter has also been measured to be 47 dBm. These switchable filters will be used to design multi-frequency switchless filter banks.

Furthermore, for differential circuit applications, an intrinsically switchable ladder-lattice balanced filter based on BST FBARs is demonstrated. A ladder-type filter and a 2-pole lattice-type filter work together to form a band-pass filter at 2 GHz with high out-of-band and near-in rejection level with a small form factor. In the OFF-state, the device presents a high isolation level between the two ports. The fabricated device demonstrates the potential of ferroelectric based reconfigurable compact, balanced filters for simplifying the future RF front ends.

Finally, to further miniaturize the filter structures and reduce the insertion loss for a given out of band rejection, an intrinsically switchable ferroelectric BST based stack crystal filter is designed and fabricated for the first time. The filter provides switchability through DC bias control, with increased isolation exceeding 30 dB. The 3-dB fractional BW and out-of-band rejection of the 1 pole BST SCF filter is 4.3% and >25 dB. The footprint of the BST SCF is less than 400 μm^2. The minimum insertion loss of the measured SCF is also 3 dB at a center frequency of 3.6 GHz. This filter is the smallest acoustic wave filter in the literature.

CHAPTER IV:

Switchless Ferroelectric FBAR Filter Banks

4.1 Chapter Motivation

To accommodate for demands for higher data rates, new frequency bands are being allocated for communications by governments across the world [49]. The incremental addition of new frequency bands with the limited space designated for RF circuits and the technologies, such as LTE-Carrier Aggregation (CA) and Multiple-Input Multiple-Output (MIMO), compels RF designers to investigate new and more practical methods of multi-band operation [50].

The integration of frequency-agile resonators and filters onto the RF front-end offers a potential solution to address these aforementioned challenges. Frequency-agile devices are capable of altering their frequency response. For filters, the adjustment of the passband characteristics allows a single component to operate in multiple communication channels that would have required multiple standard filters and switches. The resulting reduction of the overall occupied hardware area significantly reduces both the complexity and cost of RF front-end.

To realize frequency-agile resonators and filters, a promising technology incorporates ferroelectric barium strontium titanate ($Ba_{(x)}Sr_{(1-x)}TiO_3$) as the transduction layer into the design of acoustic wave devices, such as thin film bulk acoustic resonators (FBARs) [15]–[17], [25]–[28], [36], [51]–[54] and solidly mounted resonators (SMRs) [10], [11], [13], [14], [18], [20], [34], [35]. Preliminary results on intrinsically switchable filters comprised of BST FBARs have been demonstrated in previous chapters. In this chapter multiple BST FBAR filters operating at different frequencies are integrated into a switchless filter bank structure [55]. The filter bank presented here is implemented based on three 2.5 stage BST FBAR filters in series with BST varactors that are fabricated on the same silicon wafer. This chapter also presents a detailed design procedure, simulations, and fabrication process for intrinsically switchable BST filter banks. Furthermore, the multi-band operation of the ferroelectric filter bank is presented, providing the opportunity for aggregating different combinations of frequency bands.

4.2 Design and Simulation of a Switchless BST FBAR Filter Bank

An intrinsically switchable filter bank structure consists of several ferroelectric filters, covering the desired frequency band, as shown in Fig. 4.1. The transfer function of the filter bank is controlled through a DC bias network designed around the filters. Ferroelectric filter bank implementation involves the design of standalone filters and the DC biasing control, which is elaborated upon in the following parts.

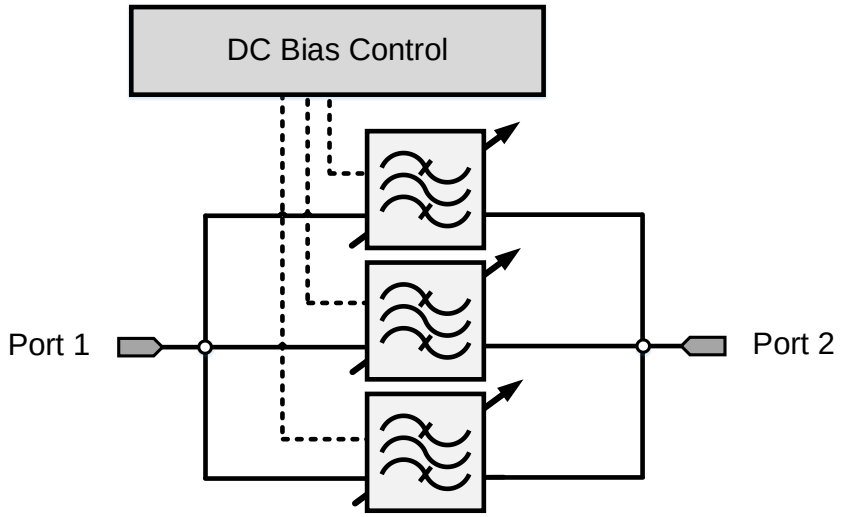

Fig. 4.1 Block diagram of a three channel intrinsically switchable filter bank.

4.2.1 Standalone BST Filter Design

The ferroelectric filter bank here is designed to operate at three frequency bands centered at 1.8, 1.9, and 2 GHz. Each filter comprises of multiple BST FBARs connected in a 2.5 stage ladder-type configuration, as shown in Fig. 4.2 (a). The electrical behavior of an individual ON state BST FBAR in this structure is represented by the lumped element mBVD model provided in Fig. 4.2 (b). In the OFF state, the resonators are simply modeled by a capacitor, as shown in the same figure.

The filters provide 2.5% fractional bandwidth (FBW) at the desired center frequencies (1.8, 1.9, and 2 GHz) for a 50 Ω system impedance (Z_0), through the image parameter method described in the previous chapter. The calculated capacitance values for the three frequency bands are provided in Table 4.1.

The resonators that make up the filters are then designed using a 1-D acoustic wave transmission line model in order to achieve the desired specifications, following the procedure is provided in chapter 2. The structure of the BST FBARs is shown in Fig. 4.3,

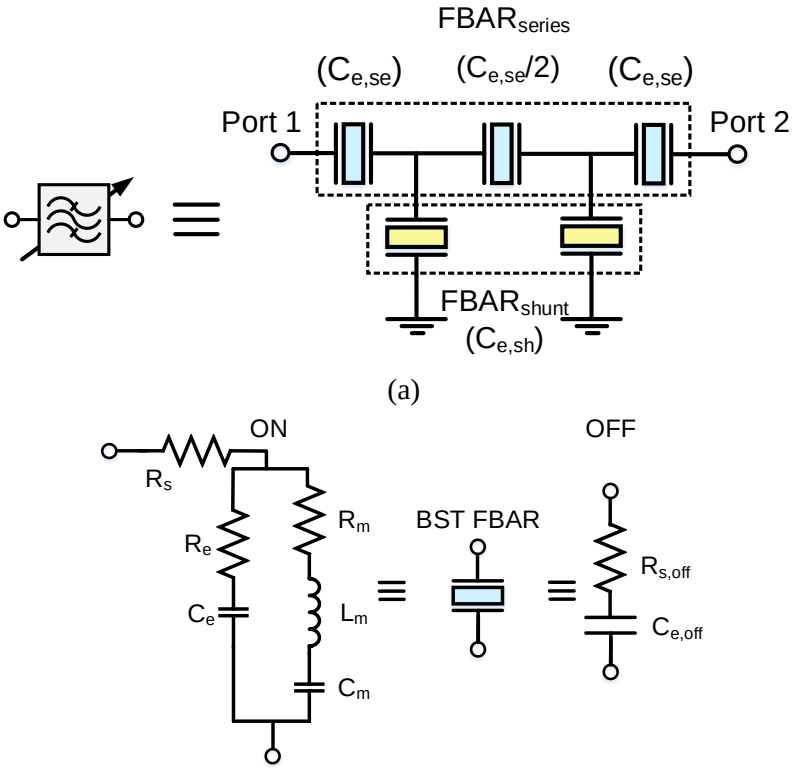

Fig. 4.2 (a) Schematic of the 2.5 stage BST FBAR filter and (b) lumped element models for describing the electrical behavior of a BST FBAR in its ON and OFF states. In the ON state, the mBVD model is used.

Table 4.1
Electrical Capacitances of the BST FBARs in Multi-band Filter

Channel #	1st: 1.8 GHz	2nd: 1.9 GHz	3rd: 2 GHz
Series FBAR Capacitance (pF)	1.40	1.32	1.26
Shunt FBAR Capacitance (pF)	4.23	4.01	3.81

consisting of platinum electrodes, a thin layer of ferroelectric BST ($Ba_{0.5}Sr_{0.5}TiO_3$), and a layer of SiO_2 beneath the bottom electrode. The thickness of each layer is selected to provide a resonance frequency at 2 GHz. The calculated BST and SiO_2 thicknesses are d_{BST} = 770 nm and d_{SiO2} = 300 nm, respectively. Also, referring to chapter 3, Q_m and K_t^2 BST FBARs are expected to be 350 and 6%, respectively.

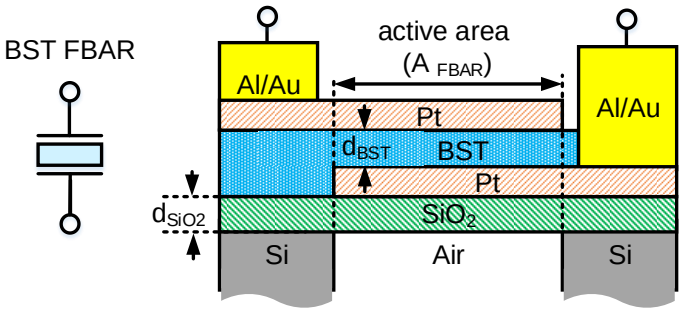

Fig. 4.3 Simplified cross-sectional view of the designed BST FBAR.

In order to downshift the operating frequency of the filters centered at 1.8 and 1.9 GHz, extra Pt layers with thicknesses calculated using 1-D transmission line simulations are added to their corresponding BST FBARs' structure. Next, the anti-resonance frequency of the shunt FBARs is set to the resonance frequency of the series FBARs, in order to obtain the typical band-pass response of ladder-type filters ($f_c = f_{a,shunt} = f_{r,series}$). Therefore, the new resonance frequency of the shunt FBARs is calculated with (3.4), where Pt mass loading layers are used to downshift their resonance frequencies. Finally, the series and shunt FBAR areas (A) for all the three filters are calculated by (3.5) to provide the required capacitances of Table 4.1. All the designed physical parameters for the intrinsically switchable BST filter bank are provided in Table 4.2. As an example, the transmission response of the standalone BST FBAR filter for 2 GHz center frequency in its ON and OFF states are plotted in Fig. 4.4. When switched on, the device provides an insertion loss (IL) of 4 dB in the passband with a FBW of 2.5%. In its OFF state, the isolation between the input and the output ports is more than 30 dB. The lumped element mBVD model is used to simulate the filter response, where the lumped element values for each BST FBAR in the ON state are calculated using the equations provided in chapter 2.

Table 4.2
Series and Shunt BST FBARs' Designed Physical Parameters

Channel #	**1st: 1.8 GHz**		**2nd: 1.9 GHz**		**3rd: 2 GHz**	
FBAR	series	shunt	series	shunt	series	shunt
A (μm)^2	974	2944	918	2791	877	2651
d_{BST} (nm)	770	770	770	770	770	770
d_{SiO2} (nm)	300	300	300	300	300	300
d_{Pt} (nm)	100	100	100	100	100	100
d_{mass1} (nm)	63	63	30	30	0	0
d_{mass2} (nm)	0	23	0	17	0	17

4.2.2 Triple Band BST Filter Bank Implementation

The intrinsically switchable triple-band filter bank is implemented by arranging the filters in parallel. In order to account for the adjacent channels' capacitive loading and improve the matching, two metal-insulator-metal (MIM) BST varactors are added in series with each 2.5 stage filter. Two inductors are also used at the input and output ports of the filter bank to further improve the matching, as shown in Fig. 4.5. The series BST varactors, biased at their lowest capacitance, provide high isolation for the filter path in its switched OFF mode. Conversely, when one of the filters is switched on, their relevant varactors' bias voltage is removed, providing the highest capacitance value, hence minimally affecting the filter's response. The performance of the filter bank can be further enhanced by selecting BST varactors with large tunability ratios (α). BST varactor tunability is

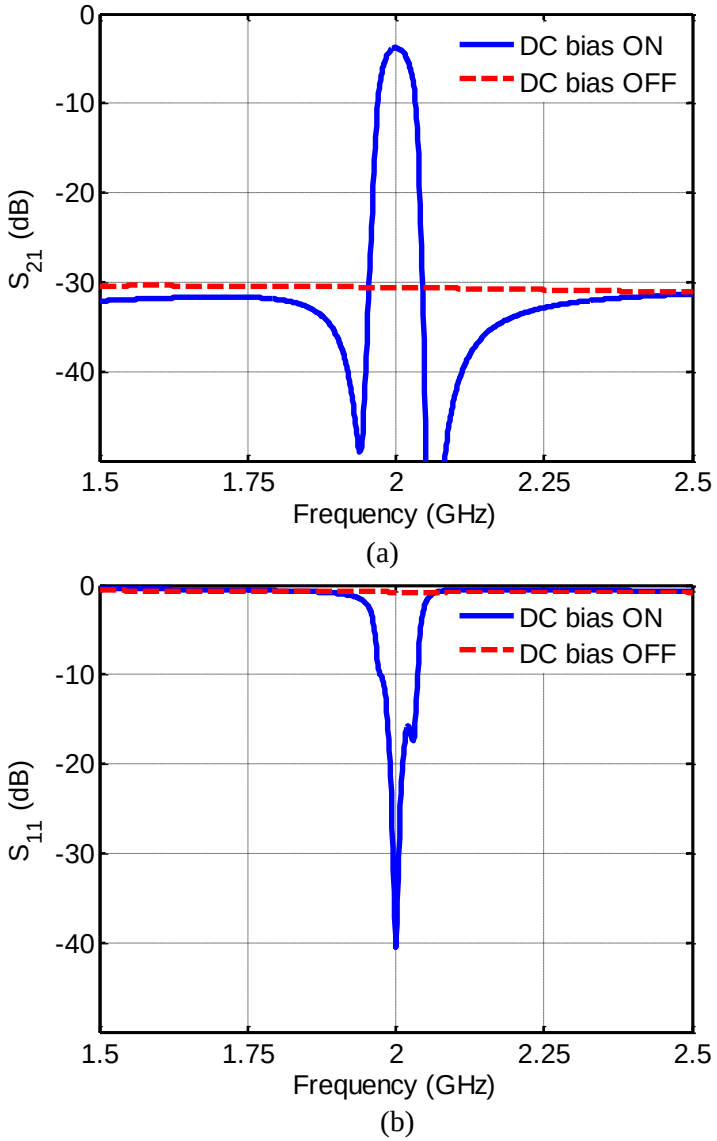

Fig. 4.4 Simulation results for (a) transmission and (b) reflection of a 2.5 stage BST FBAR filter. The out-of-band rejection and isolation levels are more than 30 dB.

typically within the 2:1 to 5:1 range [22]; however, tunability higher than 10:1 has also been demonstrated [21]. It should be noted that the implementation of the BST varactors in the filter bank does not increase the number of required processing steps, and the entire filter bank is fabricated on a single silicon substrate.

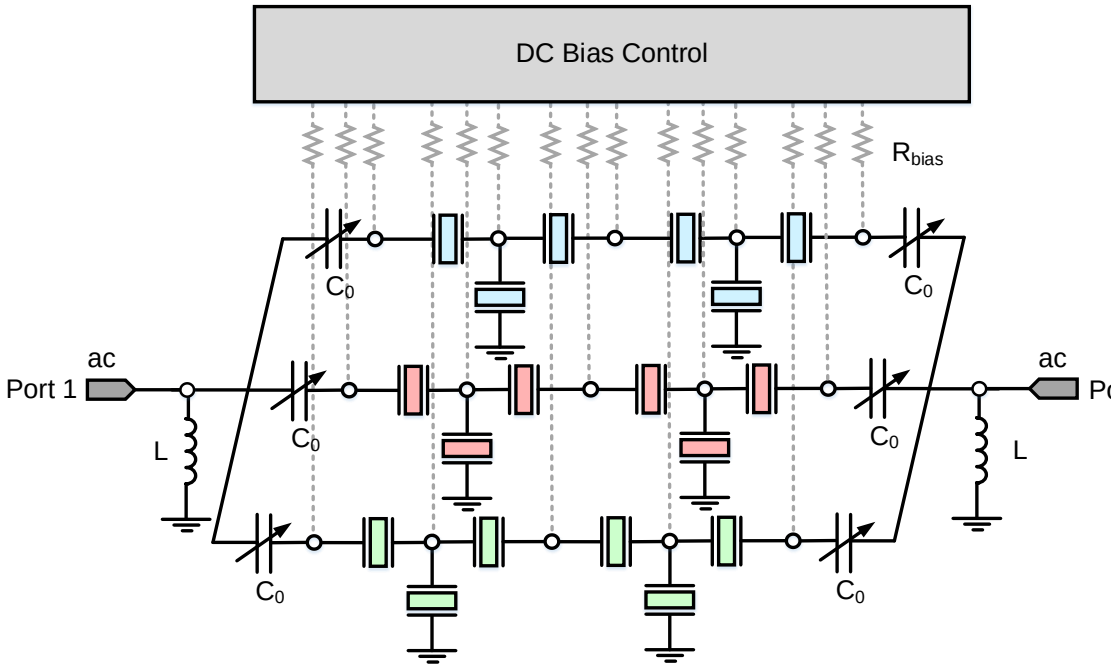

Fig. 4.5 Schematic of the designed multi-band 2.5 stage BST FBAR filter. The simplified DC biasing network is represented by dashed lines.

In order to simplify the DC biasing network, the center series FBAR is replaced with two cascaded larger FBARs. Nodes with similar DC bias voltages are also connected together through high resistivity biasing lines in order to reduce the number of DC biasing control voltages required for each filter, as shown in Fig. 4.6 (a). To turn on one of the filters (filter number *i*, where *i* = 1, 2, or 3 in Fig. 4.5) in the filter bank, all corresponding resonators of the selected filter are switched on, while the bias voltage applied to varactors along that path is set to zero. This is achieved by setting $V_{DC,i1}$ = 0 V and $V_{DC,i2}$ = V_{ON}, as seen in Fig. 4.6 (a). Conversely, to turn off a filter, the four middle resonators are switched off, and the relevant series varactors are tuned to their lowest capacitance. This can be done by setting $V_{DC,i1}$ = V_{ON} and $V_{DC,i2}$ = 0 V, as shown in Fig. 4.6 (b). To further reduce the capacitive loading effect due to the adjacent off channels, the first series resonators within the OFF state filters remain on (shown in Fig. 4.6 (b)).

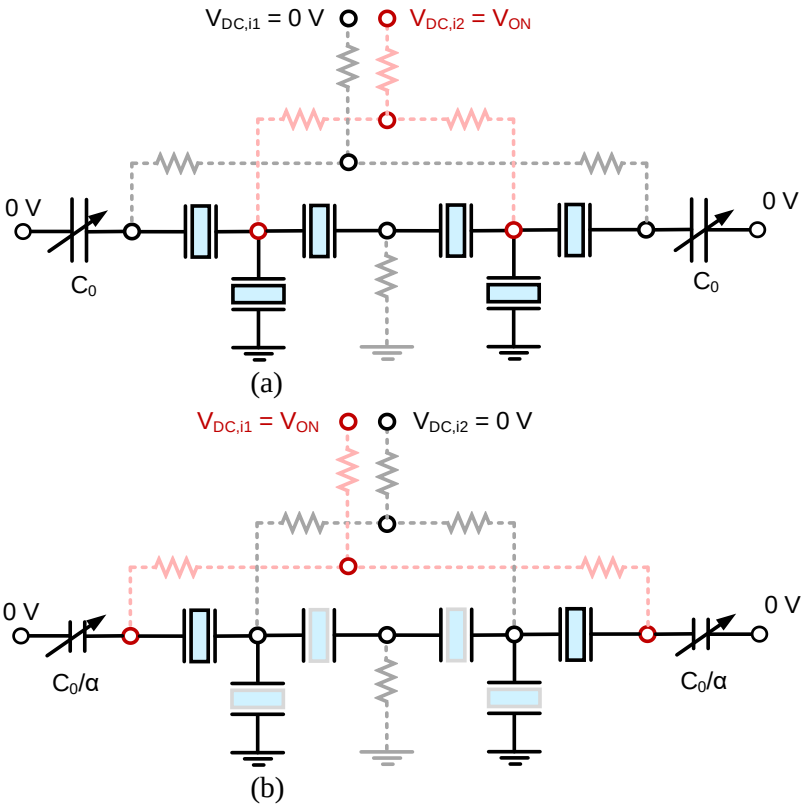

Fig. 4.6 Schematic of a filter path in the filter bank structure in its (a) ON and (b) OFF states. Implemented DC biasing network is represented in red (non-zero DC bias voltage: V_{ON}) and gray (0 V) dashed lines.

The transmission response of a single filter path corresponding to Fig. 4.6 in its ON and OFF states is shown in Fig. 4.7 (a). The OFF state isolation for a single filter path is improved by more than 15 dB after adding the varactors to reduce the loading effect on the ON state filter. The simulated frequency response of the implemented reconfigurable triple-band filter is provided in Fig. 4.7 (b), where the S_{21} of the three bandpass filters, as well as the OFF state response (when all the filters are turned off), are shown. In these simulations, BST varactors with zero bias capacitance of 2.3 pF (Q_{var} = 100) and tunability of 3:1 are used. To improve the matching, two shunt inductors (L=4 nH, Q_L=40) are used at the input and the output ports of the multi-band filter bank. DC biasing resistances should

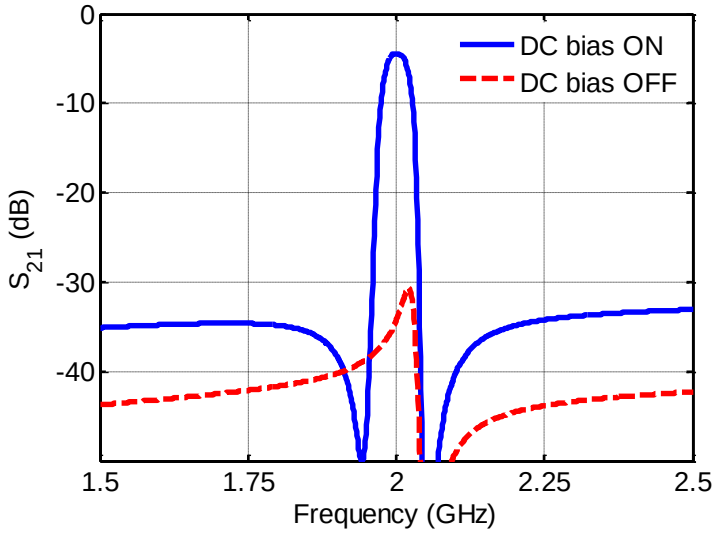

(a)

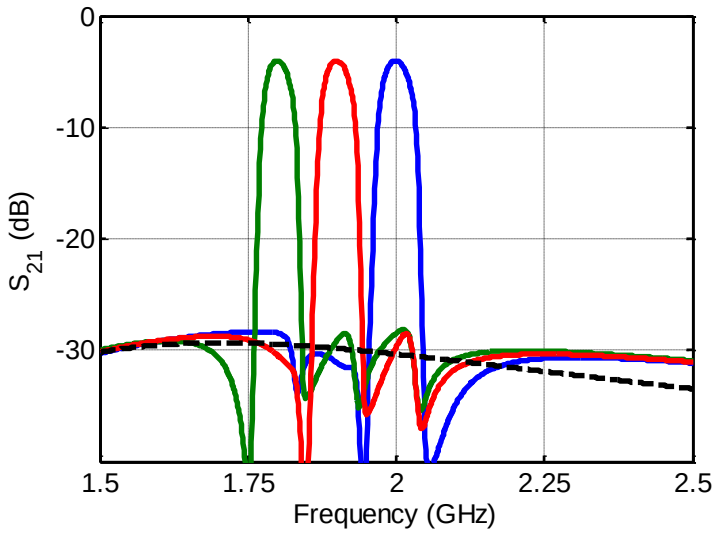

(b)

Fig. 4.7 Simulation results for (a) a single filter path shown in Fig. 6, in its ON and OFF states, and (b) the implemented triple-band filter bank with three varying ON states. The OFF state response of the filter bank is also provided in a dashed line.

be large enough to avoid degradation of the filter IL in its ON state. On the other hand, a very high R_{bias} can reduce the switching speed of the filter. Accordingly, R_{bias} is designed to provide 2000 Ω having a negligible effect on IL. In this case, for a resonator with the electrical capacitance of 1 pF (a typical value for BST FBARs in the filter structure), the RC time constant is 2 nsec, allowing a switching speed that is comparable to solid-state RF

switches. The switching speed of ferroelectric materials associated with polarization and depolarization is expected to be in the order of several Pico seconds according to [56], where they have demonstrated BST tuning at THz frequencies; based on this study, BST FBARs are expected to achieve switching speeds required for communication systems. A preliminary measurements demonstrating switching speed of less than 100 nsec for BST resonators has been reported in [57], which was restricted by the limited time constant of the biasing circuitry and measurement setup.

4.3 Fabrication Procedure for Switchless BST FBAR Filter Banks

The reconfigurable multi-band BST FBAR filter is fabricated using a process described in chapter 2. Fabrication starts by thermally growing a 300 nm SiO_2 layer on a high resistivity (100) oriented silicon wafer with a thickness of 500 μm. In the next step, a 100 nm thick Pt bottom electrode is deposited and patterned by evaporation and lift-off. A 3.0 nm-thick layer of Ti is used for the adhesion of Pt bottom electrode to the SiO_2 layer. A 770-nm of BST is then deposited by an RF magnetron sputtering system at 650°C in a 45 mTorr Ar and O_2 (4:1) environment. Two sputtering guns with RF power levels of 300 Watts are used for BST deposition. A 100 nm thick layer of Pt is then deposited and patterned with evaporation and lift-off to serve as the top electrode. After annealing the chip at 500 °C for 30 minutes in an O_2 environment, BST is etched in buffered HF (BHF) to create the release holes and a via to the bottom electrode. Additional steps include the deposition of a thin layer of NiChrome to form the DC biasing network and deposition of several thin layers of Pt, used for mass loading of the resonators. A layer of Ti/Al/Ti/Au (50/1300/50/100 nm) is then deposited and patterned using evaporation and lift-off as a contact layer. Filters are released by etching the Si substrate beneath the device in 3 Torr

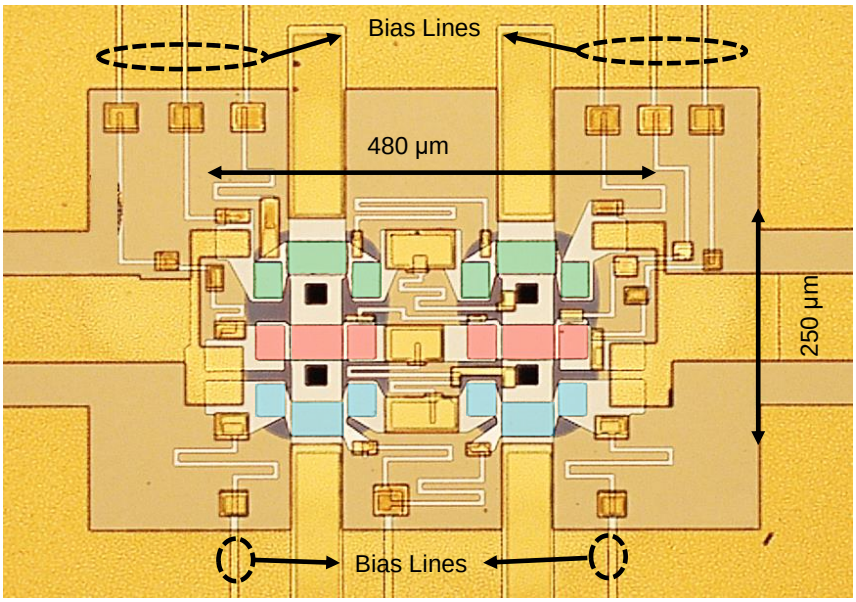

Fig. 4.8 Photograph of a fabricated multi-band 2.5 stage BST FBAR filter bank. The size of the active area for the filter bank is 0.12 $(mm)^2$.

XeF_2 environment. A photograph of the fabricated reconfigurable triple-band BST FBAR filter is shown in Fig. 4.8, where the size of the filter bank's active area (excluding the inductors) is 480 µm × 250 µm.

4.4 Switchless Filter Bank Measurement Results and Discussion

The S-parameters of the fabricated devices are measured using a vector network analyzer with 250 µm-pitch ground-signal-ground (GSG) probes. Short-open-load-thru (SOLT) calibration is performed from 0.2 to 5 GHz for a 50 Ω system impedance, and DC bias voltages are applied to the filters through a Cascade Microtech multi-contact DCQ probe. The DC bias controlling configuration for all states of the filter bank is listed in Table 4.3.

In order to verify the characteristics of the BST FBARs used in the filters, BST FBARs on the same wafer are first measured, exhibiting Q_m and K_t^2 of 340 and 6%, respectively, with a resonance frequency at 2 GHz. A standalone 2.5 stage ladder-type BST filter (similar

Table 4.3
DC Biasing Configuration for Different Channel Responses of the Filter Bank

Channel	1.8 GHz	1.9 GHz	2.0 GHz
$V_{DC,11}$ (V)	0	60	0
$V_{DC,12}$ (V)	60	0	60
$V_{DC,21}$ (V)	60	0	60
$V_{DC,22}$ (V)	0	60	0
$V_{DC,31}$ (V)	60	60	60
$V_{DC,32}$ (V)	0	0	0

to Fig. 4.2) is also measured, providing an IL of 5 dB, as shown in Fig. 4.9. The measured transmission and reflection responses for a fabricated triple-band 2.5 stage filter, utilizing BST FBARs, are depicted in Fig. 4.10. In the case where all the filters are switched off, the signal transmission is less than -27 dB over the frequency range of 1.5 to 2.5 GHz. Turning on each of the three individual filters provides band-pass responses with the center frequencies of 1.85, 1.96, and 2.04 GHz, respectively. The measured specifications for the triple band filter are summarized in Table 4.4. The fabricated ferroelectric multi-band filter bank can transition between different frequency bands of operation only by reconfiguring the applied DC bias voltages. For carrier aggregation applications, multiple bands can also be turned on simultaneously, where the DC bias voltage across the resonators and varactors are adjusted accordingly. As an example, the measured transmission response of the fabricated filter bank is shown in Fig. 4.10 (c), when both channels 1 and 3 are turned on simultaneously.

The measurement results are in close agreement with the simulated results for the switchless triple-band filter bank. The discrepancies between the center frequency of the

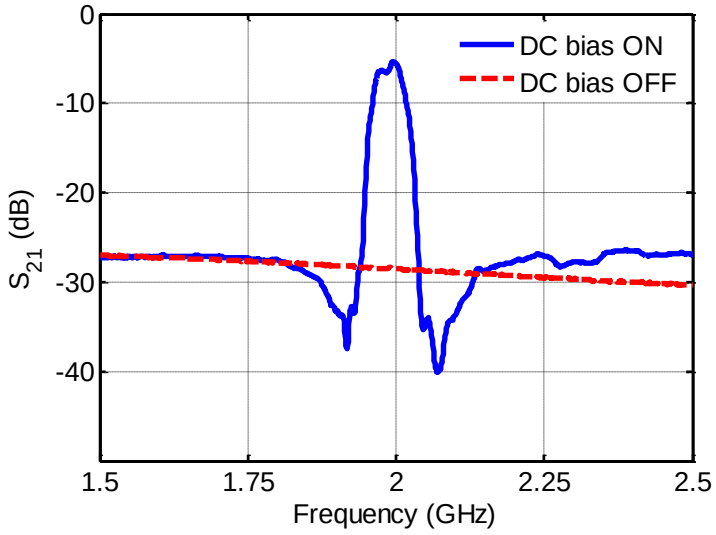

(a)

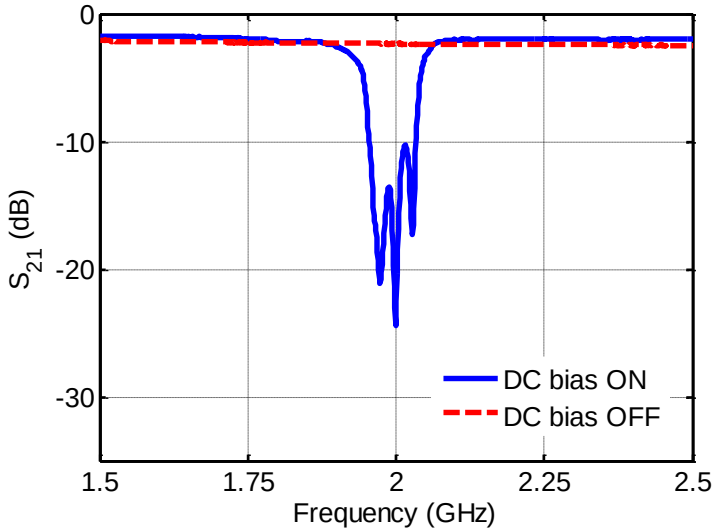

(b)

Fig. 4.9 Measurement results for (a) the transmission and (b) reflection of the standalone 2.5 stage BST FBAR filter of Fig. 2.

simulation and measurement results can be attributed to errors in the deposition of the mass loading layers and BST thickness variation throughout the wafer. The larger insertion loss of the measured filter bank, compared to the standalone filter of Fig. 4.9, is mostly attributed to the series varactors' losses having a quality factor of 30 and tunability of 2:1. This is due to the fact that the BST deposition conditions are not optimized for varactor

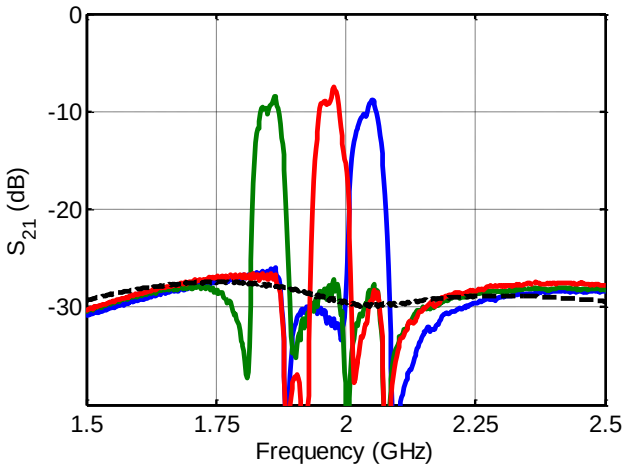

(a)

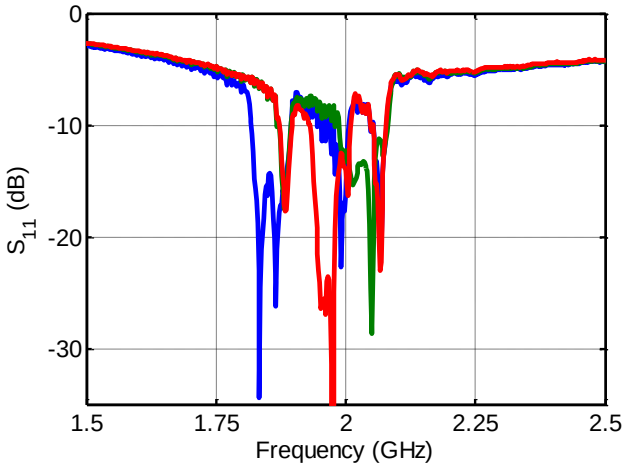

(b)

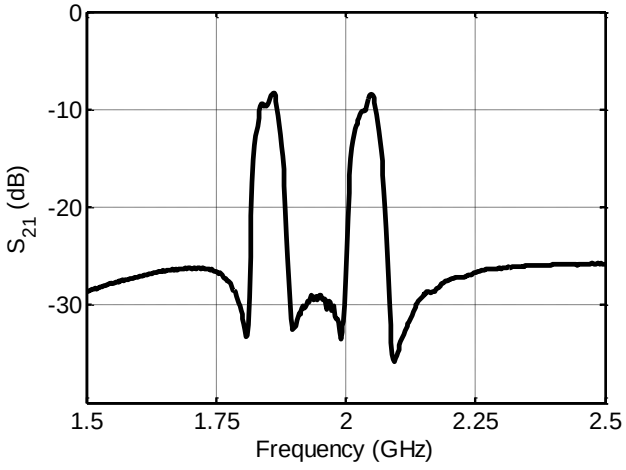

(c)

Fig. 4.10 (a) Transmission and (b) reflection responses of the measured 2.5 stage triple-band filter bank when the filters are turned on individually. (c) The transmission response of the filter bank when channel 1 and 3 are turned on simultaneously is also provided.

Table 4.4
Measured Specifications for the BST Multiband Filter

Channel #	1st: 1.8 GHz	2nd: 1.9 GHz	3rd: 2 GHz
Center Frequency (GHz)	1.85	1.96	2.04
Minimum Insertion Loss (dB)	8.4	7.4	8.7
Out-of-band Rejection Level (dB)	>27	>27	>27
Return Loss (dB)	>15	>15	>13
Fractional 3-dB BW (%)	2.7	2.4	2.5
OFF state Transmission (dB)	<-27	<-27	<-27

fabrication. The effect of the added loss from the varactors is also noticeable on the return loss of the filter bank over the operating frequency band, as shown in Fig. 4.10 (b). Small ripples in the passband of the filters are speculated to be due to the spurious lateral modes, which can be eliminated by carefully designing a ring structure around the perimeter of the resonators [28], [58] or smoothened out by apodizing the resonators [59]. The loading effect of the adjacent channels can be further reduced by creating out of band transmission zeros, similar to the approach for multiplexer design [60]. In should be noted that, in comparison to previous work on reconfigurable filters [61], [62], a significant advantage of the presented filter in this work is its compact size of less than 0.12 mm^2, due to the high permittivity of BST and the switchless nature of ferroelectric filter banks.

4.5 Chapter Conclusion

Frequency agile resonators and filters are essential for the future of multi-band, multi-standard radios. For the first time, a frequency reconfigurable triple-band 2.5 stage filter

comprised of BST FBARs is demonstrated, providing the capability to switch on and off three frequency bands individually or together without using any switches along the RF signal path. Using the inherent electrostriction property of ferroelectric BST, intrinsically switchable filters are fabricated and integrated into a filter bank with a reduced circuit area. The demonstrated intrinsically switchable filter bank consists of three BST based FBAR filters, which can be switched on or off by applying DC bias voltages to the filters. Future work will focus on the improvement of the BST FBAR filter banks' performance by optimizing its configuration for minimizing the reactive loading effect of the OFF state filters without using the varactors. A possible way is to employ the approaches developed for the synthesis of multiplexers with the manifold configuration, as described in [63], [64].

CHAPTER V:

Bandwidth Reconfigurable BST FBAR Filters

To address current limitations on mobile devices' hardware space, the investigation into frequency-agile filters continues to increase, as it promises greater functionality, reduced size, and high performance in future wireless communication systems. Frequency agility in filters typically provides either center frequency or bandwidth tuning [65]. Examples of center frequency shifting by using switchable filter banks are provided in the previous chapter. In this chapter, a novel approach to reconfigure a filter's bandwidth is presented. The adjustment of the filter's passband response provides a method to implement multi-band operation in wireless devices and reduces the number of filters required for intra-band carrier aggregation in mobile communications. Furthermore, bandwidth reconfigurable filters would address the inconsistency of frequency standards between regions across the world. For example, the majority of Asia and the Pacific use the frequency band from 470 MHz to 698 MHz for digital broadcasting, while Japan and Korea use up to 710 MHz [66]. A single bandwidth reconfigurable filter simplifies the RF front-end by replacing the original set of conventional filters and provides operation in both regions.

A common approach in designing frequency reconfigurable filters utilizes components such as varactors or switches. In [66], Matsutani et al. reported frequency agility in a surface acoustic wave (SAW) duplexer with switches for operation in the UHF spectrum for Band 28. Another example is presented in [67], where a RF SAW filter was developed with a bandwidth variation from 3.25 MHz to 6.25 MHz. However, frequency agile filters often require either a complex fabrication process or external off-chip components. In this chapter, a bandwidth reconfigurable filter based on intrinsically switchable ferroelectric BST FBARs has been introduced [68]. The presented BST based filters provide frequency reconfigurability without additional fabrication process or external off-chip components. Furthermore, the inherent high permittivity of BST leads to a large reduction in the circuit real estate.

5.1 Bandwidth Reconfigurable BST FBAR Filter's Principle of Operation

5.1.1 Multi-state BST Resonators

The electrical behavior of a typical thin film ferroelectric BST resonator in its OFF and ON states, when a DC bias voltage is applied across the resonator electrodes, is represented by their corresponding lumped element models shown in Fig. 5.1 (a). In this section, two BST FBARs are connected in series and shunt configurations to realize multi-state acoustic resonators, as shown in Fig. 5.1 (b) and (c), respectively. The BST resonators in these schematics have the same electrical and mechanical characteristics. The relationship between the resonance, f_r, and anti-resonance frequency, f_a, of each resonator is described by (5.1).

$$f_r = f_a / \sqrt{1+\gamma}$$

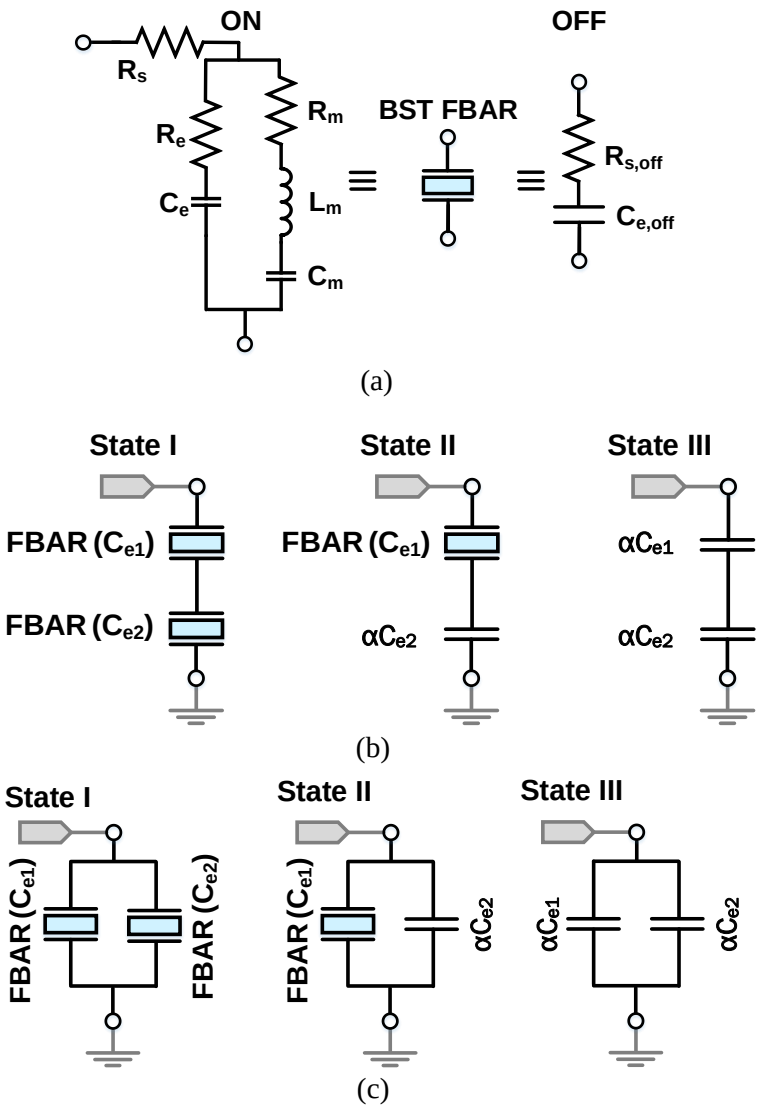

Fig. 5.1 (a) The circuit model for an individual BST FBAR (ON: mBVD, OFF: capacitor) and equivalent circuit schematic for the (b) series and (c) shunt connected BST resonators at different states [28].

(5.1)

where γ is approximately proportional to the FBARs' K_t^2 [30]:

$$\gamma \cong 8K_t^2/\pi^2 \tag{5.2}$$

The behavior of series and shunt connected BST FBARs in their ON and OFF states is described here. The series-connected BST resonators of Fig. 5.1 (b) provide a resonance

and anti-resonance frequency similar to a standalone resonator when both resonators are turned on, as shown in Fig. 5.2 (a). When one of the resonators is turned off, their equivalent electrical impedance is represented by a resonator in series with a capacitor αC_{e2}; where, α is the BST FBARs' off to on capacitance ratio. In this state, the anti-resonance frequency remains unchanged, but the resonance frequency increases, as shown in Fig. 5.2 (a). One can show that the new resonance frequency, f_r', is given by (5.3).

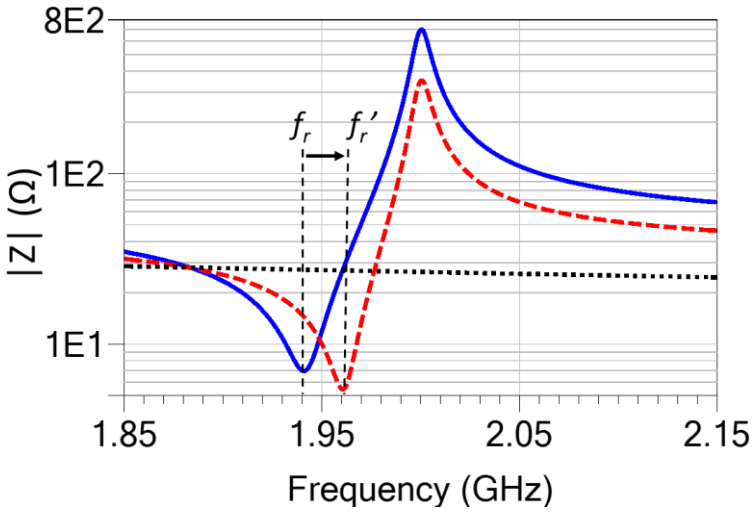

(a)

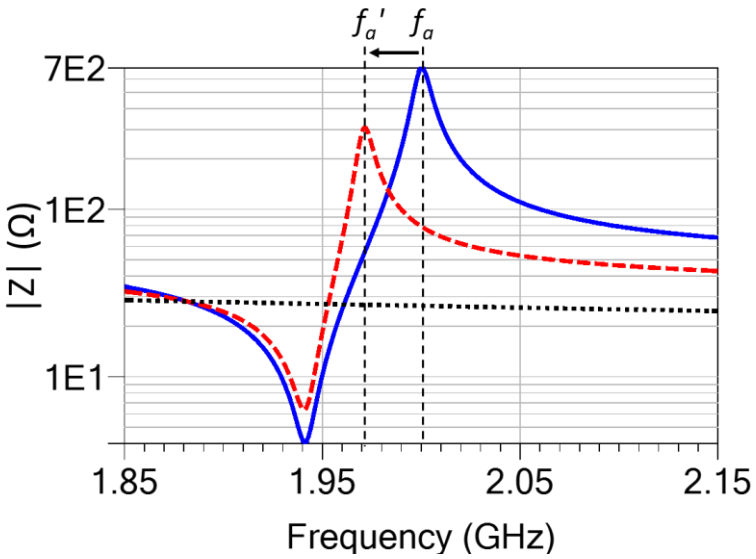

(b)

Fig. 5.2 Magnitude of the input impedance for the (a) series and (b) shunt configurations. The red dashed line denotes when one of the resonators is switched off, and the black dotted line represents the multi-state resonator's OFF response (both FBARs are switched off).

$$f'_r = f_r\sqrt{1+\gamma/(1+\alpha C_{e2}/C_{e1})} \tag{5.3}$$

Similarly, the response of the shunt connected BST resonators in Fig. 5.1 (c), when both resonators are turned on, is represented in Fig. 5.2 (b) by a solid line. However, when one resonator is turned off, the resonance frequency remains constant while the anti-resonance frequency (f_a') decreases, as shown in Fig. 5.2 (b). It can be shown that f_a' can be calculated by (5.4). In the OFF state, when both resonators are turned off for either configuration, the overall impedance resembles a simple capacitor, shown by the dotted line.

$$f_a' = f_a\sqrt{1-\frac{\gamma}{\gamma+1}/(1+C_{e1}/\alpha C_{e2})} \tag{5.4}$$

5.1.2 Intrinsically Switchable, Bandwidth Reconfigurable BST FBAR Filters

A ladder-type filter composed of the multi-state BST resonators provides a bandpass response with adjustable transmission zeros. A general schematic of a ladder-type filter unit-cell based on these multi-state resonators is shown in Fig. 5.3. For clarity purposes, dc bias lines are not presented. The anti-resonance frequency of the resonators in the shunt branch is set to match the resonance frequency of the series branch. Under this condition, the resulting filter provides typical bandpass characteristics, where $f_c = f_{a,shunt} = f_{r,series}$, and transmission zeros are located at $f_{r,shunt}$ and $f_{a,series}$.

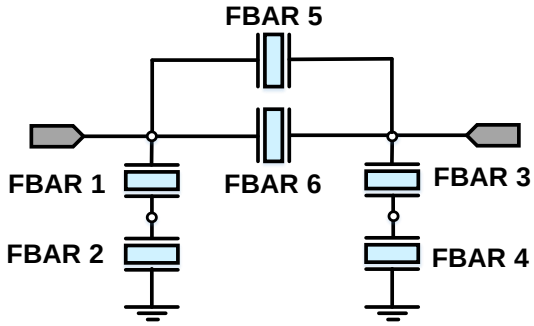

Fig. 5.3 The schematic of the intrinsically switchable and BW reconfigurable BST FBAR filter unit cell.

When all the BST FBARs switched on, the filter response is represented in Fig. 5.4 with a solid line. If BST FBAR 1 and 3 are switched off, the frequency of the lower transmission zero increases (red dashed line in Fig. 5.4 (a)). In the same manner, the upper transmission zero is controlled by turning off the BST FBAR 5 (green dotted line in Fig. 5.4(a)). For a greater bandwidth tuning and simultaneous adjustment of both transmission zeros, BST FBARs 1, 3, and 5 are all turned off at once, as shown by the dotted line in Fig.

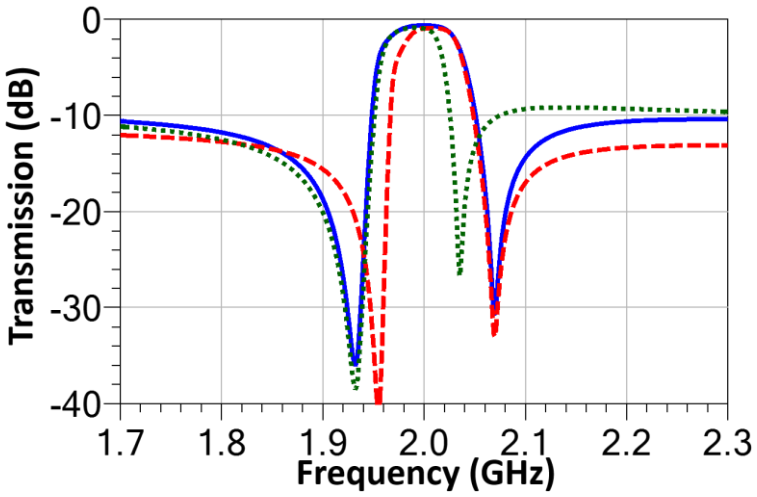

(a)

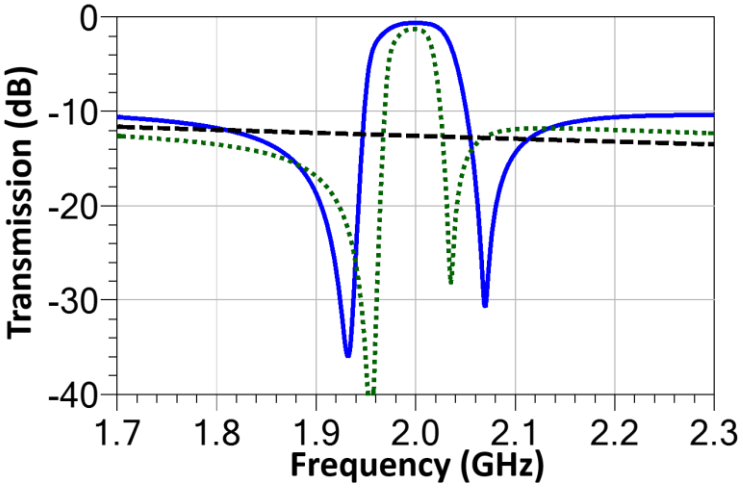

(b)

Fig. 5.4 (a) Simulated S_{21} response for the filter with all resonators on (solid line) and when transmission zeros are shifted individually. (b) Simulated S_{21} response for the filter with all resonators on (solid line) compared with the response of the filter when both transmission zeros (dotted) are simultaneously shifted, along with its OFF state response (dashed).

5.4 (b). The amount of frequency variation of the lower and upper transmission zeros is set by the capacitance ratio of the two resonators in shunt and series branches, respectively. The OFF state of the filter occurs when all BST FBARs are switched off in order to isolate the input and output ports (dashed line in Fig. 5.4(b)).

Further bandwidth reconfigurability can be attained by cascading either additional series resonators in the shunt branch or parallel resonators in the series branch of the acoustic filter, as shown in the design examples.

5.2 Bandwidth Reconfigurable BST FBAR Filter Demonstration

Two BW reconfigurable and intrinsically switchable ferroelectric filters are designed, fabricated, and measured as proof of concept. Design examples include reconfigurable filters with two and three BW states, based on a varying lower cutoff frequency.

5.2.1 Design of a BST FBAR Filter with Two BW States

Schematic of a 1.5 stage FBAR filter with multi-state resonators of section 4.1 (Fig. 4.1 (b)) in its shunt branches is presented in Fig. 5.5. In the first step, a 1.5 stage filter is designed using the image parameter method, described in [39], for a system impedance of 50 Ω. In this design $C_{e,se}$ and $C_{e,sh}$ are calculated to provide 3% fractional bandwidth (FBW) using the formulas in [39] ($C_{e,se}$ = 0.8 pF, and $C_{e,sh}$ = 1.5 pF). The K_t^2 and Q_m of the resonators, following the process described in [37], are expected to be 6% and 300. The original shunt FBARs are replaced with two series-connected larger FBARs with an equivalent electrical capacitance to the original ($C_{e1} = C_{e2} = 2C_{e,sh}$), providing a secondary

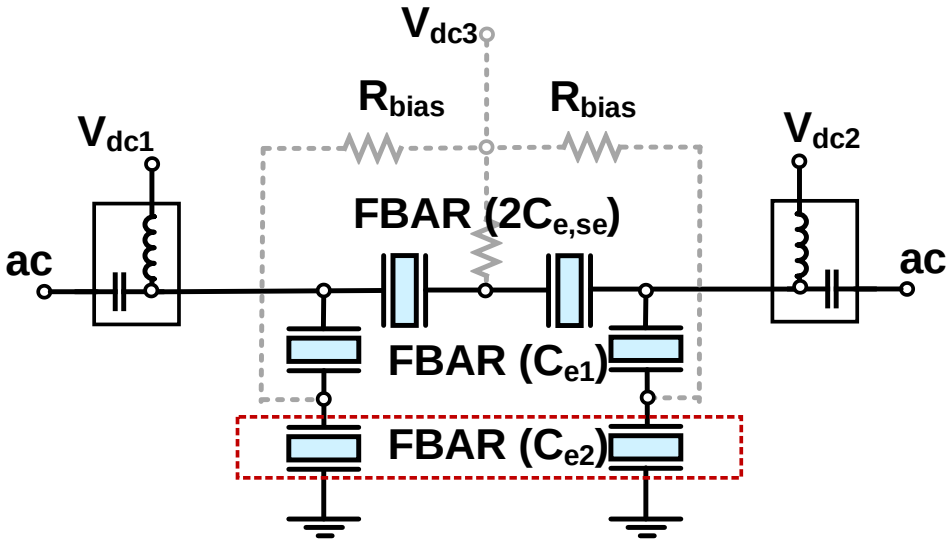

Fig. 5.5 The schematic of the intrinsically switchable FBAR filter unit cell for lower cutoff frequency tuning. The ON state response of the filter is adjusted by alternating the DC bias across the resonators highlighted in red dashed box.

state with a FBW of 2.2%. The center BST FBAR of the structure with an electric capacitance of $C_{e,se}$ is also replaced by two FBARs with twice the original capacitance ($2C_{e,se}$) to simplify the DC biasing network.

The filter's simulated transmission response for all three states is plotted in Fig. 5.6.

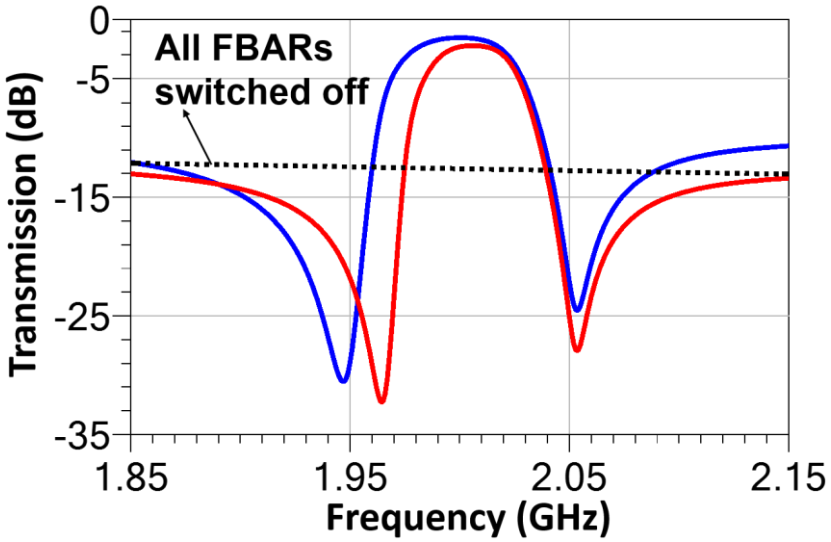

Fig. 5.6 Transmission response for the simulated reconfigurable FBAR filter with two BW states.

The filter transitions between two different BW states by turning on or off the resonators denoted in a red dashed box. Also, with zero DC bias across all resonators, the filter unit cell provides more than 12 dB of isolation between the ports (state 3). The small variation in the minimum insertion loss between the two ON states of the filter is due to the change in the impedance of the device.

5.2.2 Design of a Ferroelectric FBAR Filter with Three BW States

The idea is extended to the design of a reconfigurable filter with three BW states. The schematic of the designed filter is shown in Fig. 5.7. In this schematic, each shunt branch of the filter includes three series-connected BST FBARs. Similar to the design outlined in part A, each of the FBARs in the filter's shunt branch is individually switched on or off based on the desired state of operation, where the filter now contains an intermediate state for more versatility in frequency tuning. All three BST FBARs in the shunt branches have

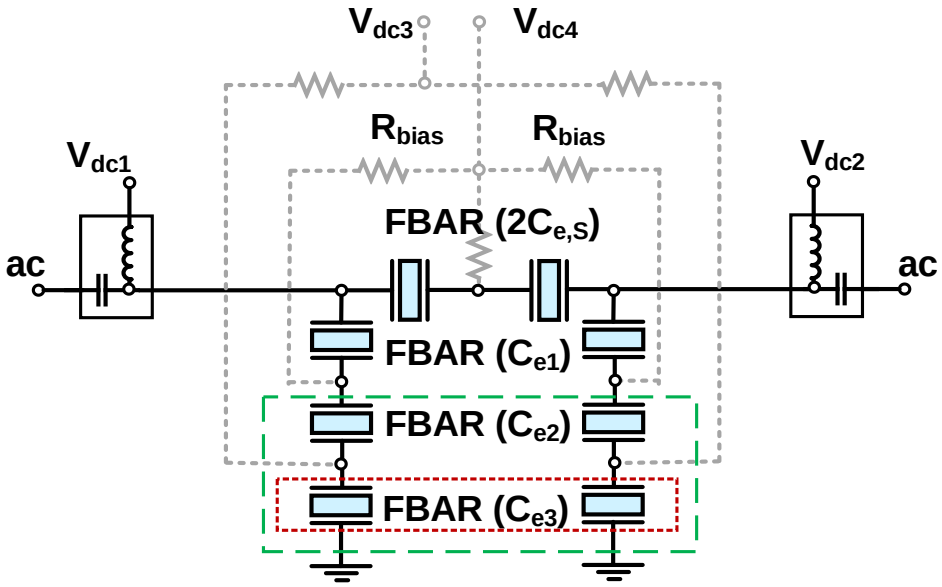

Fig. 5.7 The schematic of the BW reconfigurable FBAR filter for lower cutoff frequency tuning. The ON state response of the filter is adjusted by alternating the dc bias across the shunt resonators indicated in red and green, where the OFF state resonators are replaced with their equivalent OFF state capacitances ($\alpha\, C_{e2}$ and $\alpha\, C_{e3}$).

the same size with an overall equivalent capacitance of $C_{e,sh}$. Thus, the filter offers a passband response with three different lower cutoff frequencies and FBW of 2%, 2.5%, and 3 % based on the number of ON state resonators on the shunt branches.

By turning off the set of BST FBARs inside the red dotted box, the filter moves from an initial state with a passband response of 60 MHz to an intermediate state with a BW of 50 MHz, as shown in Fig. 5.8. The device transitions to the third state with a BW of 40 MHz by switching off another pair of the BST FBARs (highlighted in a green dashed box). Finally, when all bias voltages are set to 0 V, the device isolates the input and the output ports.

5.3 Fabrication and Measurement of the Bandwidth Reconfigurable Filters

BST filters are fabricated by following a procedure described in chapter 2, and characterized using a vector network analyzer and a Cascade Microtech probe station with 250 µm-pitch ground-signal-ground (GSG) probes. Bias voltages are applied through

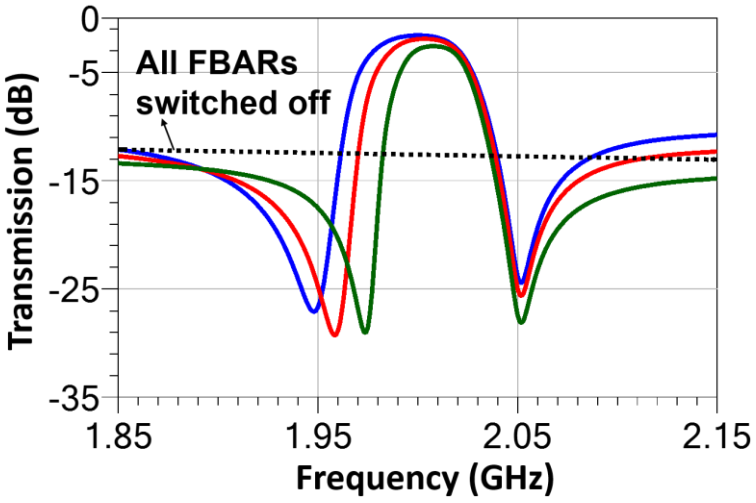

Fig. 5.8 Transmission response for the simulated reconfigurable BST FBAR filter with three BW states.

external DC probes and bias tees connected to the ports in order to record measurements of the resonators and filters during each of their respective states. Individual BST FBAR measurements show Q_m and K_t^2 of 340 and 6%, respectively, which are in line with the values used in the simulation. By increasing the DC voltage applied across the BST FBAR electrodes from 0 V, an electric signal at the design frequency excites a thickness mode resonance. The effective K_t^2 of the resonator increases as a function of the applied DC bias. In order to achieve the required K_t^2 for the resonator of Fig. 5.9, one can increase the bias voltage to V_{ON} = 70 V; however, the required DC bias voltage for maximum K_t^2 in BST resonators can be reduced to less than 20 V by optimizing the resonator stack up for a thinner BST film [11], [15]. The BST thin film relative permittivity and loss tangent in ON state are measured at 2 GHz to be 220 and 0.02 using the method described in [69]. On wafer short-open-load-thru (SOLT) calibration is performed from 0.2 to 5 GHz for a 50 Ω system impedance. The effect of bias tees is de-embedded through the calibration as they are located between GSG probes and VNA port.

The magnitude of the impedance for a measured series-connected multi-state resonator (Fig. 5.1 (a)) along with its photograph are provided in Fig. 5.9. By switching one of the resonators from its ON to OFF state, the device resonance frequency switches from 1899 MHz to 1912 MHz. These resonators are then integrated onto 1.5 stage reconfigurable filters with two and three BW states with varying lower cutoff frequencies. Photographs of the fabricated filters are provided in Fig. 5.10 with an active area of 120 μm × 220 μm and 200 μm × 230 μm for the filters with two and three BW states, respectively.

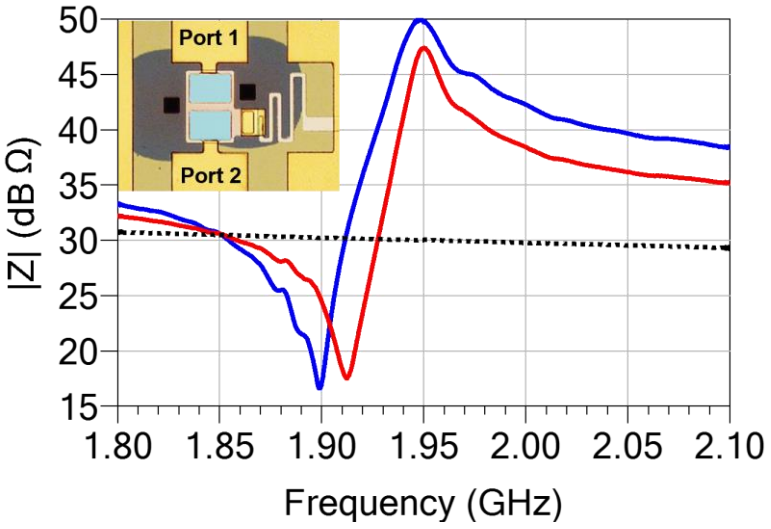

(a)

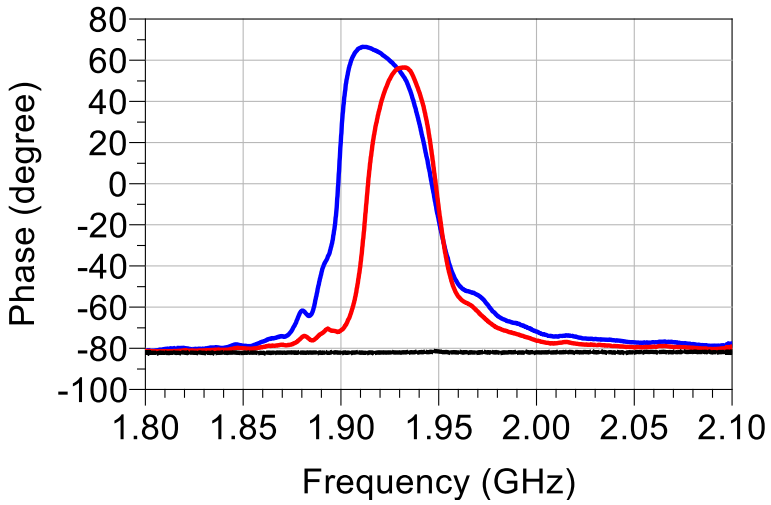

(b)

Fig. 5.9 Photograph of a two series connected resonators and its impedance (a) magnitude in dB and (b) phase when: both are on (blue), only one is on (red), and both are off (black dotted line).

5.3.1 BST FBAR Filter with Two Bandwidth States

Biasing conditions to transition between the two BW states of the filter are provided in Table 5.1. In state one, which is characterized with the widest bandwidth, DC bias voltages ($V_{dc3} = V_{ON}$, $V_{dc1} = V_{dc2} = 0$ V) are applied to switch on all the resonators, leading to a bandpass response with 3% fractional bandwidth, as shown in Fig. 5.11. In order to switch to the second state, V_{ON} is now applied through bias tees (i.e., $V_{dc1} = V_{dc2} = V_{ON}$),

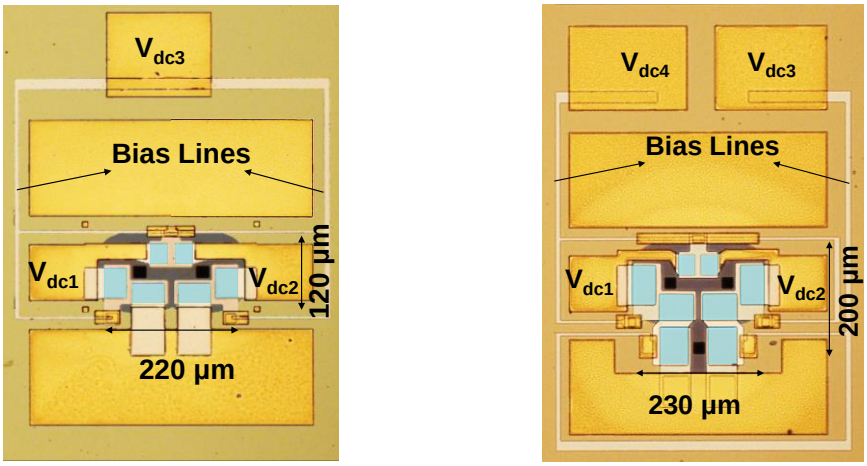

(a) (b)

Fig. 5.10 Photographs of the fabricated BST FBAR filters with (a) two and (b) three BW state.

and V_{dc3} is set to 0 V. At this state, the filter fractional BW reduces from 3% to 2.2%. The resulting filter comprises of shunt branches with a resonator in series with a capacitor, which causes the lower frequency band edge to shift from 1908 MHz (state 1) to 1953 MHz (state 2). For the case where zero dc bias voltage is applied to all three nodes, the BST thin film no longer exhibits piezoelectricity, and the 1.5 stage filter switches off, providing isolation greater than 12 dB between the input and output ports. The measured characteristics of the filter are summarized in Table 5.2.

There is a small discrepancy in the frequency of transmission zeros of the measured filter as compared to the simulation results, which can be attributed to the variation of thicknesses for the deposited layers. The minimum insertion loss of the measured filter is

Table 5.1
DC Bias Voltage Values for the Filter with Two BW States

Filter State	V_{dc1} (V)	V_{dc2} (V)	V_{dc3} (V)
OFF State	0	0	0
ON State 1: FBW = 3%	0	0	V_{ON}
ON State 2: FBW = 2%	V_{ON}	V_{ON}	0

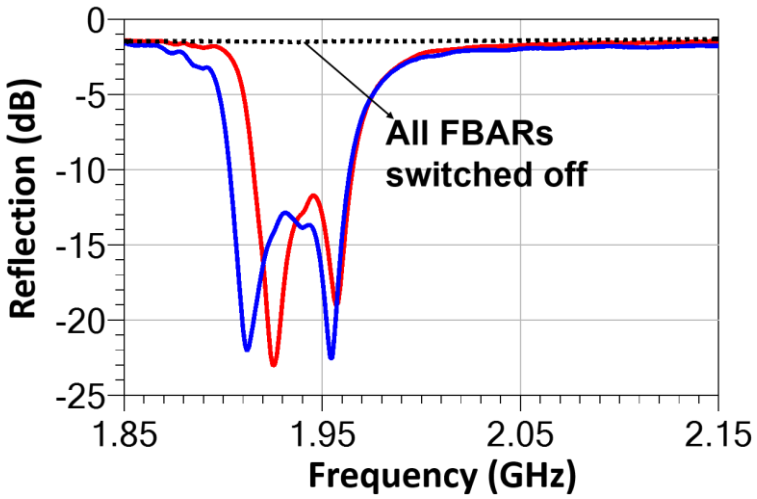

(a)

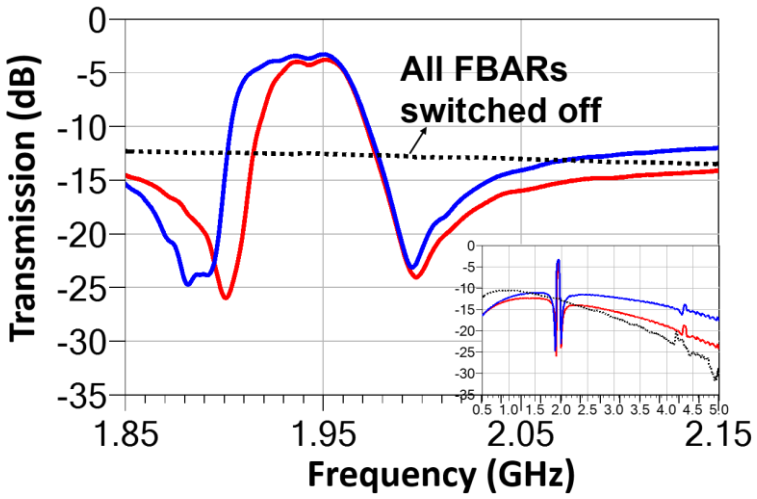

(b)

Fig. 5.11 (a) Reflection and (b) transmission responses for the measured BW reconfigurable BST FBAR filter unit cell in state 1 and state 2. OFF (state 3) response of the filter is also plotted in black dotted line.

Table 5.2
Measured Filter Specifications for the Reconfigurable BST Filter with Two BW States

Device	*State 1*	*State 2*
Fractional 3-dB BW (%)	3.0	2.2
Minimum Insertion Loss (dB)	3.2	3.7
Out-of-band Rejection Level (dB)	>14	>12
Return Loss (dB)	>13	>12
OFF state Isolation (dB)	>12	>12

slightly increased due to the conductor loss of the interconnecting lines in between the resonators. Despite the variation, the overall measured frequency shift of the lower transmission zero of the filter remains consistent with simulation results.

5.3.2 BST FBAR Filter with Three Bandwidth Reconfigurable States

The second fabricated filter example contains three states of bandwidth reconfigurability. Table 5.3 lists the biasing conditions of the reconfigurable filter with three BW states, which also requires an additional DC probe to transition between all the three states.

The measurement results for the filter in three different configurations, as well as the OFF state response of the filter, as shown in Fig. 5.12, demonstrate good agreement with the simulated results. The results for each filter state are separately measured based on the biasing setup described in Table 5.3. The filter specification in three different BW states and the OFF state is summarized in Table 5.4. The measured filter unit-cell can provide three different fractional BW values of 3%, 2.5%, and 2% under different biasing conditions. It also provides more than 13 dB isolation between the ports in its OFF state.

Table 5.3
DC Bias Voltage Values for the Filter with Three BW States

Filter State	V_{dc1} (V)	V_{dc2} (V)	V_{dc3} (V)	V_{dc4} (V)
OFF State	0	0	0	0
ON State 1: FBW = 3%	V_{ON}	V_{ON}	V_{ON}	0
ON State 2: FBW = 2.5%	0	0	0	V_{ON}
ON State 3: FBW = 2%	V_{ON}	V_{ON}	0	0

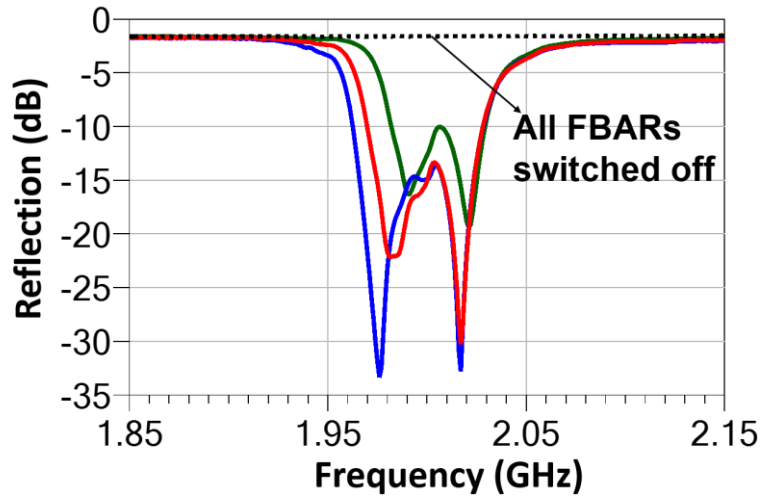

(a)

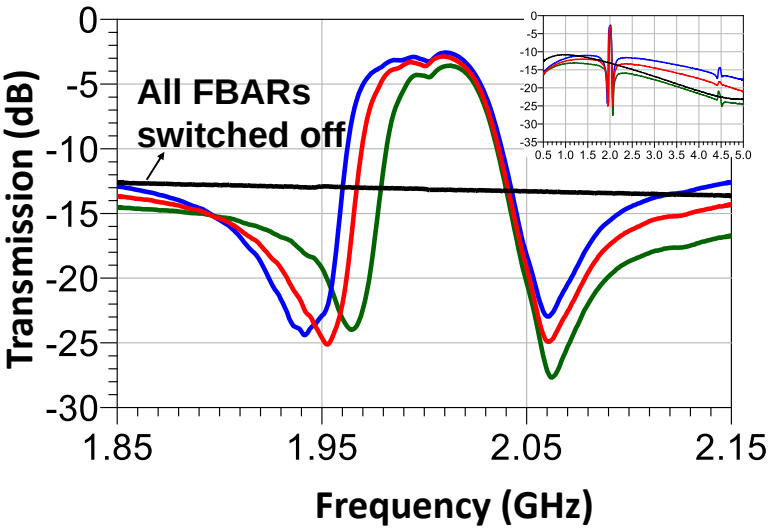

(b)

Fig. 5.12 (a) Reflection and (b) transmission response for the measured bandwidth reconfigurable FBAR filter unit cell across all of its states.

The out-of-band rejection and OFF state isolation level of the filter can be increased by using a higher-order filter. As mentioned in the previous section, small discrepancies in the 3 dB cutoff frequencies between simulated and measured results are attributed to BST and mass loading layer thickness variation during the fabrication process. For both filters, the measured results show some fluctuation in the insertion loss across the passband. This occurs due to spurious resonance modes, which can be alleviated through the apodization

Table 5.4
Measured Filter Specifications for the Reconfigurable BST Filter with Three BW States

Device	*State 1*	*State 2*	*State 3*
Fractional 3-dB BW (%)	3.0	2.5	2
Minimum Insertion Loss (dB)	2.5	2.8	3.5
Out-of-band Rejection Level (dB)	>13	>14	>17
Return Loss (dB)	>15	>15	>10
OFF state Isolation (dB)	>13	>13	>13

[30] of the BST resonators, hence improving the filter response. In order to improve the BST filter performance and reduce the filter IL, BST resonators' Q need to be enhanced.

Based on theoretical calculations for a single crystal $SrTiO_3$, it is expected that BST resonators achieve quality factors higher than 1000 at sub 6 GHz [20]. Improved Q factors can be achieved through optimization of BST ferroelectric deposition conditions, such as the deposition temperature, partial pressure, and annealing process, which has been shown to significantly affect the film quality and composition [11], [70]. Also, the design features need to be optimized in terms of resonator shape, lateral boundaries, and optimization of acoustic dispersion.

5.4 Chapter Conclusion

The design and fabrication of intrinsically switchable and bandwidth reconfigurable FBAR filters based on ferroelectric BST are presented in this chapter. Key advantages of the presented ferroelectric filters include achieving bandwidth reconfigurability without employing external tunable components, such as varactors and switches. BST also

possesses high relative permittivity compared to conventional piezoelectric materials, which significantly decreases the overall circuit area for these devices. Using multi-state resonators, lower cutoff frequency adjustment of the filter is demonstrated. For further reconfigurability, multi-state resonators can be employed in both the series and shunt branch of a ladder-type bandpass filter to adjust both transmission zeros. Such bandwidth reconfigurable filters would address the inconsistency of frequency standards between regions across the world, and reduce the number of required filters for intra band career aggregation.

CHAPTER VI:

Mode-Switchable Ferroelectric FBARs Exploiting Negative Piezoelectricity in Multilayer Ferroelectrics

6.1 Chapter Motivation

With each generation of communication networks, now transitioning to 5G, the complexity and cost of radio frequency (RF) front-end in mobile devices have been rapidly increasing. Frequency band proliferation is the biggest contributor to the added RF front-ends complexity in the design of future radios. To operate at various frequency bands, a complex combination of switches and acoustic wave filters are needed in current mobile devices. The number of filters in mobile phones is expected to exceed 100 with the advent of 5G networks [2], [71], further exasperating the design complexity of radios in current mobile devices. Alternative techniques, including reconfigurable and agile frequency selective components, are being considered to reduce the complexity and cost of RF front-end circuitry.

Agile frequency-selective components can simplify the design of future radios with their reconfigurable response. Multiple reconfigurable filters based on intrinsically

switchable BST resonators have been demonstrated in previous chapters. For instance, reconfigurable bulk acoustic wave filters with an adjustable center frequency and bandwidth, using BST FBARs, have been described in chapters 3 and 4, respectively. In this chapter, a mode switchable BST FBAR and a multi-band FBAR filter based on electric field induced positive and negative piezoelectric coefficients in multilayer thin film BST capable of extending the operating frequency of conventional BAW devices are presented.

Ferroelectric BST, incorporated into a structure with multiple transduction layers, allows for the design of a new class of reconfigurable bulk acoustic wave devices. A multilayer ferroelectric structure can form a mode-switchable bulk acoustic wave resonator, selectively switching between its different Eigen frequencies. The first experimental demonstration of a mode-switchable FBAR based on a bilayer ferroelectric BST is presented in this chapter [48], [72]. As presented here theoretical calculations show that the higher-order even and odd resonance modes of multi-layer ferroelectric FBARs can individually be turned on by controlling the sign and magnitude of the effective piezoelectric coefficient independently in each layer of the ferroelectric FBAR. What is more significant is that the individual higher-order modes exhibit effective electromechanical coupling coefficients (K_{eff}^2) equal to the K_{eff}^2 of the fundamental mode, which is contrary to the trend $K_{eff}^2 \propto 1/n^2$ exhibited by conventional piezoelectric bulk acoustic wave resonators. The mode-switching capability and the mode insensetive K_{eff}^2 of higher-order mode FBARs allow for the design of high microwave frequency band-switching filters with large fractional bandwidths. Such filters not only can eliminate the need for external switches but also reduce the number of required filters in RF front-ends.

As an experimental validation of this idea, a dual-band-switching filter based on bilayer BST FBARs is implemented for the first time.

6.2 Mode-switchable Multilayer Ferroelectric FBARs

Ferroelectric BST has a centrosymmetric cubic perovskite unit-cell in its paraelectric phase (above phase transition temperature T_c), and the components of its piezoelectric tensor are all zero. However, a DC electric field, applied to BST shifts the center titanium ion along the field direction, which breaks centrosymmetry and induces piezoelectricity in BST (i.e., electric-field-induced piezoelectricity), as shown in Fig 6.1 (a)-(b). In order to further explain ferroelectric BST's acoustic properties and its applications, a simplified form of the constitutive equations are adopted. The induced strain (S) and electrical polarization (P) in BST are related by the electrostriction equation (6.1). The electric polarization under an applied electric field E can be expressed by (6.2) [23].

$$S = \alpha P^2 \tag{6.1}$$

$$P = P_s + \chi E \tag{6.2}$$

where α is the electrostriction coefficient, P_s is spontaneous polarization, and χ is the susceptibility of the material. Substituting (6.2) in (6.1) results in:

$$S = \alpha P_s^2 + (2\alpha P_s \chi + \alpha \chi^2 E)E \tag{6.3}$$

In paraelectric phase BST, where the spontaneous polarization is zero (P_s = 0), the electromechanical transduction occurs primarily through the E-field-induced piezoelectric effect (second term in the parentheses) that originates from BST's large electrostriction coefficient. The typical quadratic strain (S)-electric field (E) curve for BST in the

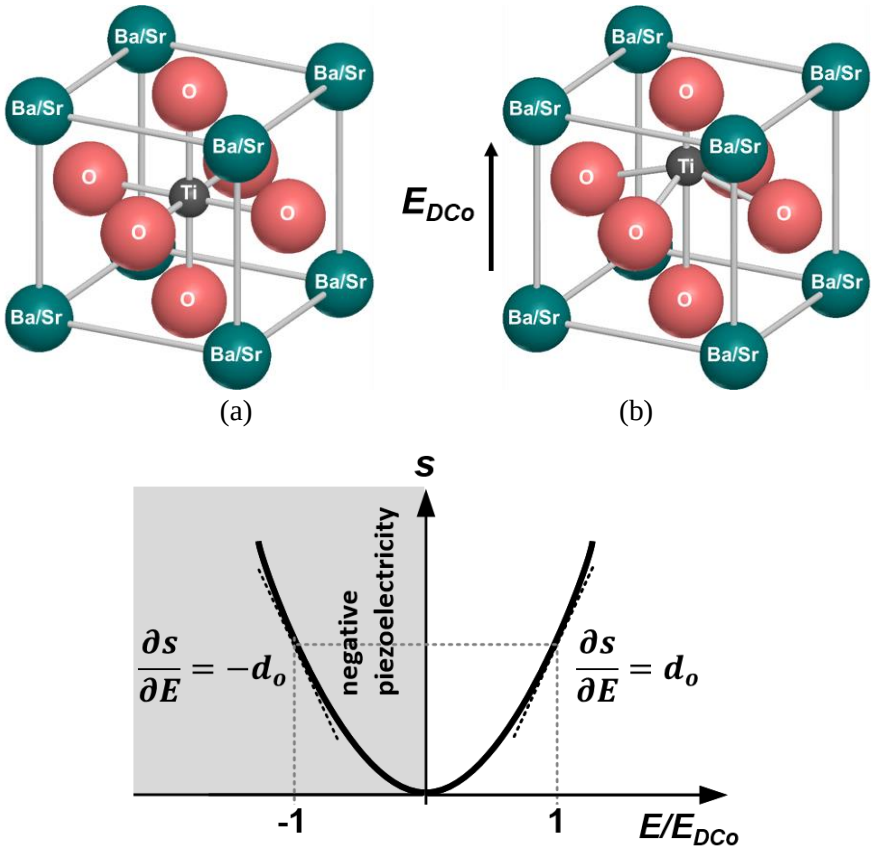

Fig. 6.1 (a) BST's centrosymmetric crystal unit-cell under no DC bias electric field. (b) After applying E_{DCo} bias, the center Ti ion shifts and induces piezoelectricity. (c) Typical strain (***S***)-normalized electric field (***E***) curve for BST; the slope of the ***S***-***E*** curve at each bias point represents the effective piezoelectric coefficient in the material.

paraelectric phase is shown in Fig. 6.1 (c), where its effective piezoelectric coefficient is determined by the slope of the curve at a particular DC bias point (E_{DC}):

$$d_{eff} = \frac{dS}{dE}|_{E_{DC}} = 2\alpha\chi^2 E_{DC} \tag{6.4}$$

Based on (6.4), the sign and value of the effective piezoelectric coefficient are functions of the polarity and magnitude of the applied DC electric field ($E_{DC} = \frac{V_{DC}}{t_{BST}}$, where V_{DC} is the voltage across the BST film and t_{BST} is the BST film thickness). As shown in Fig. 6.1 (c), BST thin film not only provides E-field induced piezoelectricity but also exhibits an E-field-induced 'negative' piezoelectricity, when biased to the left side of the curve, under a

negative DC bias voltage.

This unique property of BST (i.e., E-field induced piezoelectric and negative piezoelectric effect) can be leveraged to control the pattern of effective piezoelectric coefficient in bulk acoustic wave resonators containing multi-layers of BST. An example of such structure is shown in Fig 6.2 (a), where the control of piezoelectricity in individual BST layers allows for the generation of different patterns of non-uniform piezoelectric coefficients, leading to selective excitation of different resonance modes with a constant electromechanical coupling coefficient. In such a mode-switchable FBAR, each resonance mode can be selected through a set of DC bias voltages applied across the BST layers to generate the appropriate pattern of the piezoelectric coefficients for that particular mode.

The multilayer device in Fig. 6.2(a) contains N BST layers, each having a thickness of t (total membrane thickness is Nt). In order to simplify the explanation of the behavior of such resonator, it is assumed that electrodes' thickness is infinitesimal, and only the longitudinal thickness modes are excited. At a certain bias point, the general piezoelectric constitutive equations that relate the electrical and mechanical fields together are (6.5) and (6.6).

$$T = cS - eE \tag{6.5}$$

$$D = eS + \epsilon E \tag{6.6}$$

where $S = \frac{\partial u}{\partial z}$ (u is the particle displacement), T is stress, E is the small-signal electric field, D is electric displacement, c is elasticity, ϵ is the material permittivity, e is equal to $c\frac{ds}{dE}|_{E_{DC}}$, and ρ is material density. Calculating E from (6.5) and substituting into (6.6) leads to the wave equation of (6.7).

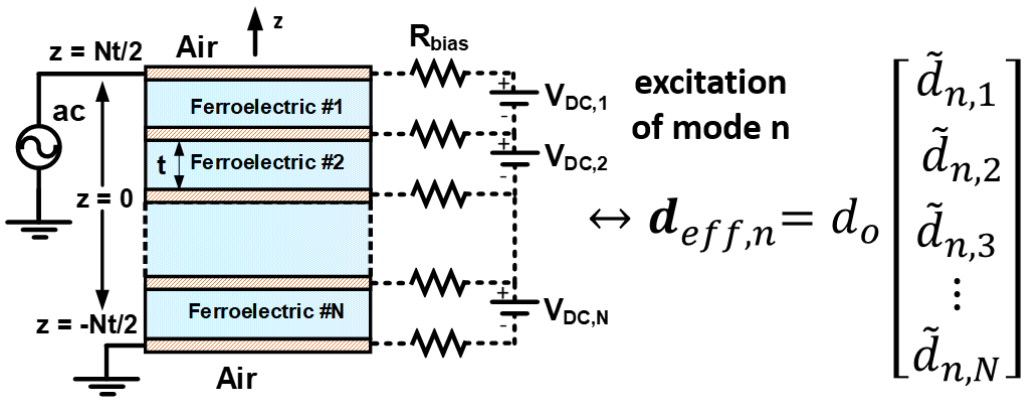

(a)

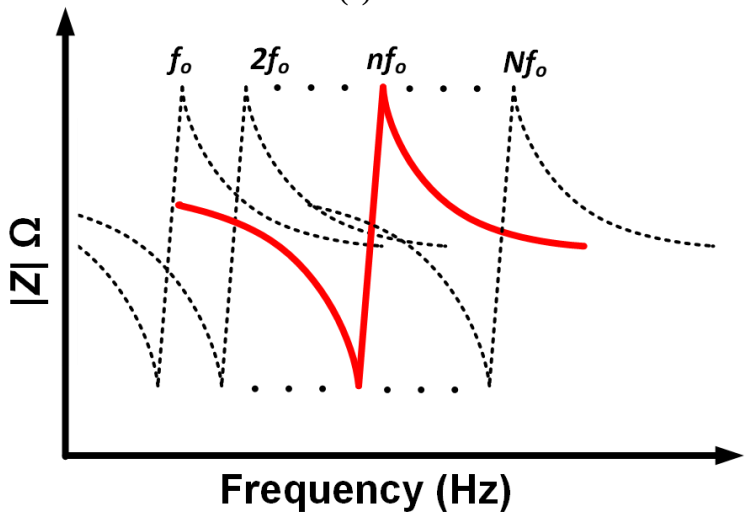

(b)

Fig. 6.2 Multi-layer ferroelectric resonator (a) structure and (b) magnitude of the impedance for different states of the device. Piezoelectricity in each BST layer is a function of the magnitude and polarity of the applied DC bias voltage.

$$\frac{\partial^2 u}{\partial z^2} + \frac{\epsilon\rho}{(c\epsilon + e^2)}\omega^2 u = 0 \tag{6.7}$$

The solution of (6.7) for the particle displacement field in the bulk of the device can be shown to be in the form of (6.8).

$$u(z) = \mathrm{a}.\sin(k_f z) + b.\cos(k_f z) \tag{6.8}$$

where k_f is the acoustic propagation constant (wavenumber) in the ferroelectric:

$$k_f = \frac{\omega}{\sqrt{\frac{c}{\rho}\left(1+\frac{e^2}{c\epsilon}\right)}} \tag{6.9}$$

Assuming stress-free boundaries ($\frac{\partial u}{\partial z}|_{z=\pm\frac{Nt}{2}} = 0$), the particle displacement field is simplified to (6.10) for odd and even modes, with resonance conditions given in (6.11).

$$u_n(z) = u_o \tilde{u}_n(z) = \begin{cases} u_o \sin(k_{f,n} z), n = 1, 3, 5, \dots \\ u_o \cos(k_{f,n} z), n = 2, 4, 6, \dots \end{cases} \tag{6.10}$$

$$k_{f,n} \frac{Nt}{2} = n.\frac{\pi}{2} \tag{6.11}$$

The effective electromechanical coupling coefficient for each of these modes in an acoustic wave resonator is defined by Berlincourt formula (6.12) [30], [58].

$$K_{eff}^2 = \frac{U_m^2}{U_e U_d} \tag{6.12}$$

Where U_m is mutual energy, U_e is elastic energy, and U_d is electrical energy stored in the dielectric material calculated by:

$$U_m = \frac{1}{2}\int_V d_{eff}(TE)dV, U_e = \frac{1}{2}\int_V sT^2 dV, U_d = \frac{1}{2}\int_V \epsilon E^2 dV \tag{6.13}$$

and s is compliance, V is the volume of the resonator, d_{eff} is the effective piezoelectric coefficient throughout the bulk of the resonator defined by:

$$d_{eff}(z) = d_o \tilde{d}(z) \tag{6.14}$$

where $\tilde{d}(z)$ is the normalized pattern function for piezoelectric coefficient versus z, the axis normal the membrane. By substituting (6.10) and (6.13) into (6.12), and simplifying the results one can show that the K_{eff}^2 for the nth harmonic mode is equal to (6.15).

$$K_{eff}^2 = \frac{\left(\int_A \int_{-\frac{Nt}{2}}^{\frac{Nt}{2}} d_{eff}(z) ET(z) dz\right)^2}{\int_V \epsilon E^2 dV \int_V sT^2(z) dV} = \frac{\pi^2 K_{effo}^2}{16\left(\frac{Nt}{2}\right)^2}\left(\int_{-\frac{Nt}{2}}^{\frac{Nt}{2}} \tilde{d}\,(z)\tilde{u}_n'(z) dz\right)^2 \quad (6.15)$$

where K_{effo}^2 is the electromechanical coupling coefficient of the fundamental mode for a conventional piezoelectric membrane resonator (i.e., $\tilde{d}\,(z) = 1$):

$$K_{effo}^2 = \frac{8}{\pi^2}\frac{d_o^2}{s\epsilon} \quad (6.16)$$

Since all the longitudinal thickness modes u_n and their derivatives are orthogonal to each other:

$$\int_{-Nt/2}^{Nt/2} u_n' u_m' \, dz = \begin{cases} 1, m = n \\ 0, m \neq n \end{cases} \quad (6.17)$$

a single resonance mode n ($1 < n < N$) can be turned on by creating an appropriate pattern of non-uniform piezoelectric coefficient proportional to stress field of that mode (e.g., for nth harmonic mode: $\tilde{d}_n(z) = \tilde{u}_n'(z)$). Under this condition, only a single mode n (e.g., mode number n = 1, 2, 3, …) is excited with a constant electromechanical coupling coefficient equal to (6.18).

$$K_{eff,n}^2 = \frac{\pi^2}{16} K_{effo}^2 \quad (6.18)$$

This is in contrast to single-layer piezoelectric resonators (i.e., $\tilde{d}\,(z) = 1$), where all odd harmonic modes simultaneously coexist with rapidly decreasing effective electromechanical coupling coefficients that are inversely proportional to the square of mode numbers (i.e. $K_{eff,n} = \frac{1}{n^2} K_{effo}^2$, n = 1, 3, 5, …) [30].

As an example, in a 6-layer ferroelectric FBAR, the required pattern of the non-uniform piezoelectric coefficient to excite only 2nd harmonic mode (represented by dashed lines) is shown in Fig. 6.3. In reality, however, the piezoelectricity in each layer is a constant value; thus, one needs to find the step function pattern close to the ideal sinusoidal

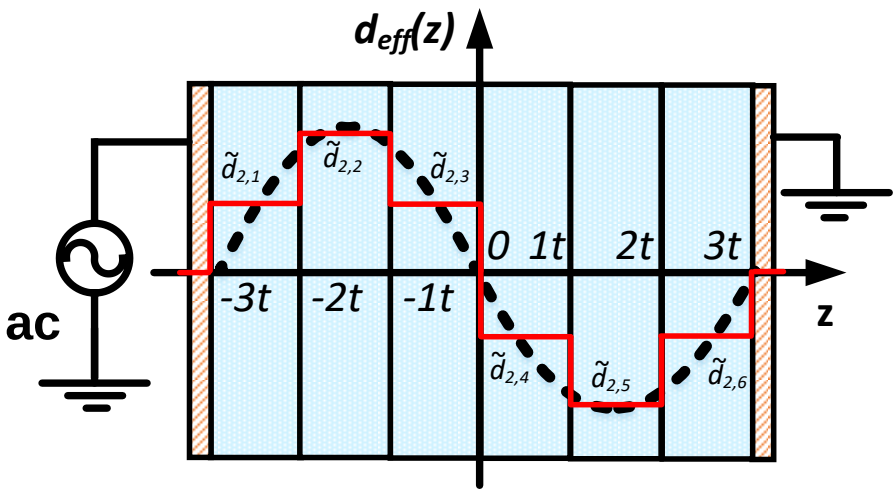

Fig. 6.3 Ideal non-uniform pattern of effective piezoelectric coefficient (represented by the dashed lines) for the selective excitation of a single mode (mode 2) in a 6-layer ferroelectric bulk acoustic wave resonator. The stepwise solidline function is the actual realization of such pattern. The piezoelectric coefficient in the last three layers is negative.

mode shape, as shown in a red solid line in Fig. 6.3. This can be achieved by solving a set of N equations (6.19), (step function version of (6.15)), to find an optimized $\tilde{d}_n(z) = [\tilde{d}_{n,1}, \tilde{d}_{n,2}, \ldots, \tilde{d}_{n,N}]$ that maximizes the $K^2_{eff,i=n}$ and minimizes $K^2_{eff,i\neq n}$, where $\tilde{d}_{n,i}$ is the normalized effective piezoelectric coefficient in each layer.

$$K^2_{eff,n} = \frac{K^2_{effo}}{4n^2}\left(\sum_{i=1}^{N} \tilde{d}_{n,i}\left[\sin\left(k_{f,n}\left((-N+2i)\frac{t}{2}\right)\right) - \sin\left(k_{f,n}\left((-N+2i-2)\frac{t}{2}\right)\right)\right]\right)^2, \qquad n = 1,3,5,\ldots$$

(6.19 - a)

$$K_{eff,n}^2 = \frac{K_{effo}^2}{4n^2}\left(\sum_{i=1}^{N} \tilde{d}_{n,i}\left[\cos\left(k_n\left((-N+2i)\frac{t}{2}\right)\right) - \cos\left(k_n((-N+2i-2)\frac{t}{2}\right)\right]\right)^2, n = 2,4,6,\ldots$$

(6.19 - b)

Accordingly, a set of DC bias voltages can be applied to the BST layers to realize the optimum $\tilde{d}_n(z)$ = [$\tilde{d}_{n,1}$, $\tilde{d}_{n,2,}$ … , $\tilde{d}_{n,N}$] for each mode. Thus, the mode-switchable FBARs based on multi-layers of ferroelectric BST can selectively resonate at the desired harmonic modes as shown in Fig. 6.2 (b), allowing for the design of a new class of band-switchable devices, like filters and oscillators. These mode-switchable resonators not only eliminate the need for external switches but also reduce the number of required frequency selective components in RF modules.

A one-dimensional physical model based on the Mason model arranged in a configuration shown in Fig. 6.4, can be used to analyze and optimize the performance of the mode-switchable resonators. This model allows to design the thickness of different layers and predict the device parameters such as its impedance. The harmonic resonance frequencies of the structure and their K_{eff}^2 can be estimated for different patterns of non-

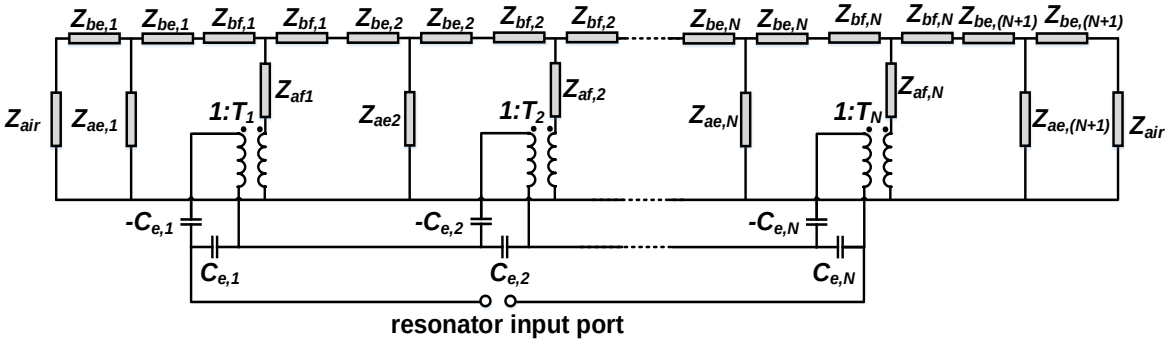

Fig. 6.4 Mason equivalent circuit model for a switched-mode ferroelectric FBAR containing N ferroelectric layers.

uniform piezoelectric coefficients. In this model, Z_{air} is the acoustic impedance of the air, Z_e and Z_f are the acoustic impedance of the electrodes and the ferroelectric layers; also, the acoustic to electrical domain transformation ratio (T_i), for each BST layer is related to the effective piezoelectric coefficient in that layer through equation (6.20).

$$T_i = \frac{cd_{eff}C_{e,i}}{\epsilon} \tag{6.20}$$

In the model of Fig. 6.4, $C_{e,i}$ is the electrical capacitance of each BST layer, and the rest of the parameters are calculated by (6.21)-(6.24).

$$Z_{be,i} = jZ_eA \times tan(k_e \times t_{e,i}) \tag{6.21}$$

$$Z_{ae,i} = \frac{-jZ_eA}{\sin(k_e \times 2t_{e,i})} \tag{6.22}$$

$$Z_{bf,i} = jZ_fA \times tan(k_f \times t_{f,i}) \tag{6.23}$$

$$Z_{af,i} = \frac{-jZ_fA}{\sin(k_f \times 2t_{f,i})} \tag{6.24}$$

Where A is the resonator area, k_e and k_f are the wavenumbers ($2\pi f$/acoustic velocity (v)) in electrodes and the ferroelectric layers, and $t_{e,i}$ and $t_{f,i}$ are the thickness of i^{th} electrode and ferroelectric layer.

The electrical response of a mode-switchable resonator can also be represented by an mBVD model [29] with multiple switchable motional branches, as shown in Fig. 6.5. This model helps to further study and predict the performance of filters as a function of the resonators' overall electromechanical coupling coefficient and quality factors, and eventually design reconfigurable filters based on mode-switchable resonators. In this model, $C_{e,n}$ and $R_{e,n}$ account for the effective electrical capacitance and loss of the multi-layer structure calculated by (6.25) and (6.26). The capacitance ($C_{e,i}$) and quality factor ($Q_{e,i}$) in each layer is a function of the tunability of the deposited ferroelectric material and

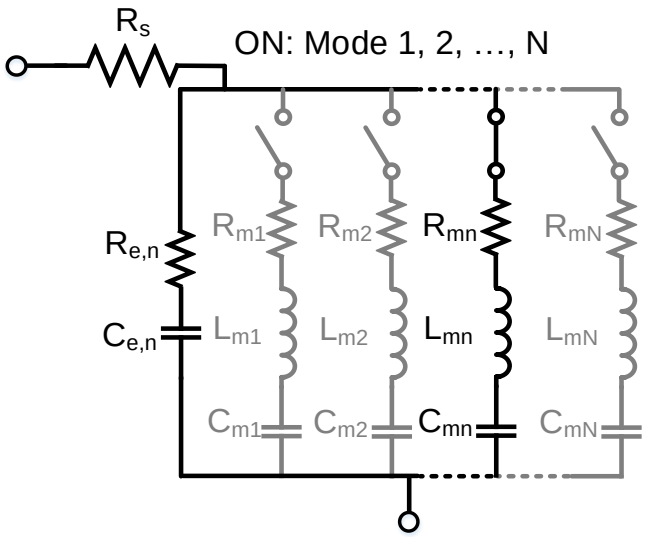

Fig. 6.5 The lumped element model for multi-layer BST resonator in (a) ON (e.g. only mode *n* is excited) and (b) OFF states.

the applied voltage across that layer. The motional branch for mode *n* includes $R_{m,n}$, $L_{m,n}$, and $C_{m,n}$ that can be calculated with (6.27) - (6.29).

$$\frac{1}{C_{e,n}} = \sum_{i=1}^{N} \frac{1}{C_{e,i}(V_{DC,i})} \tag{6.25}$$

$$R_{e,n} = \sum_{i=1}^{N} \frac{1}{C_{e,i}(V_{DC,i})Q_{e,i}} \tag{6.26}$$

$$C_{m,n} = C_{e,n}\left[\left(\frac{f_{a,n}}{f_{r,n}}\right)^2 - 1\right] \tag{6.27}$$

$$L_{m,n} = \frac{1}{C_{m,n}(2\pi f_{r,n})^2} \tag{6.28}$$

$$R_{m,n} = \frac{2\pi f_{r,n} L_{m,n}}{Q_{m,n}} \tag{6.29}$$

In these equations, the resonance (f_r) and anti-resonance frequency (f_a) and accordingly the effective electromechanical coupling coefficient of each harmonic mode are employed from the Mason model calculations, where the effect of the electrodes with finite thickness

value are considered.

A mode-switchable FBAR based on bilayer ferroelectric BST is designed and fabricated to validate the theoretical analysis. The resonators are then used to implement a reconfigurable band-switching ferroelectric FBAR filter.

6.3 Design and Simulation of a Mode-Switchable FBAR and a Band-switching Filter

A mode-switchable FBAR based on a bilayer ferroelectric thin film BST membrane structure, shown in Fig. 6.6, is intrinsically switchable and can resonate at its even or odd

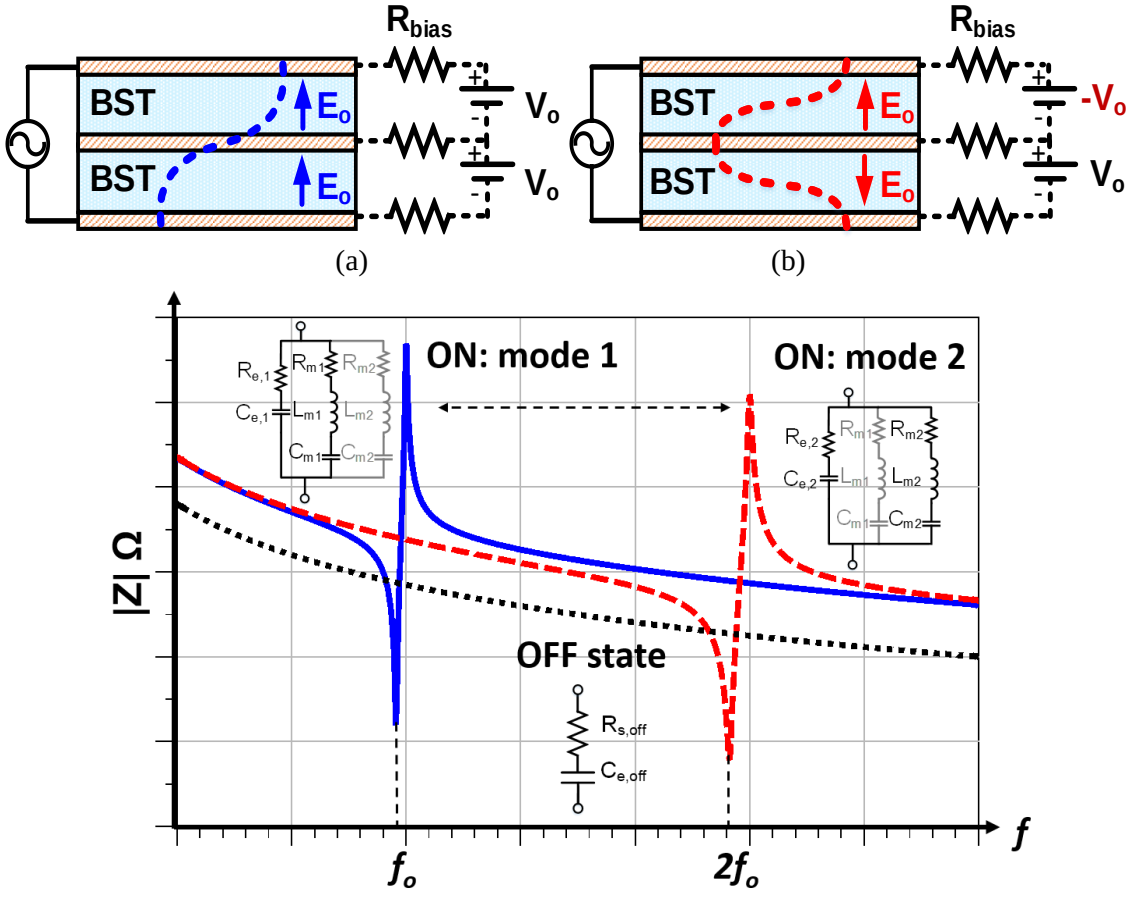

(c)

Fig. 6.6 Bilayer BST resonator particle displacement distribution for (a) mode 1 with DC bias of $V_{DC} \times [1, 1]$ and (b) mode 2 with DC bias of $V_{DC} \times [1, -1]$, and (c) their corresponding impedance response.

harmonic modes selectively. When DC bias voltage with a similar polarity and magnitude applied across both BST layers, the sign and magnitude of the induced effective piezoelectric coefficient in BST films are similar; the entire structure forms a simple FBAR operating at its fundamental mode (f_o) with a half-wavelength acoustic standing wave across the resonator (mode 1), as shown in Fig. 6.6 (a). However, when the two DC bias voltages with opposite polarities are applied to the bilayer BST FBAR, the effective piezoelectric coefficients in BST films are opposite in sign, according to (6.4), and two BST films vibrate in antiphase direction; only the second mode is excited as shown in Fig. 6.6 (b). Therefore, by alternating between negative and positive polarities of DC bias voltages applied to only one of the BST films, the device can resonate at even or odd harmonic modes. Based on (6.15), both mode 1 and 2 are expected to provide the same K_{eff}^2. The typical electrical impedance response of a bilayer stacked BST FBAR operating at modes 1 and 2, as well as its OFF state, is displayed in Fig 6.6 (c).

A bilayer BST FBAR is designed to have its first and second harmonic modes at 2 GHz and 3.6 GHz, respectively. The cross-sectional view of the device is shown in Fig. 6.7. The device contains two BST layers sandwiched between three Pt electrodes. An extra 100-nm-thick SiO_2 is grown beneath the bottom electrode as a diffusion barrier layer. The

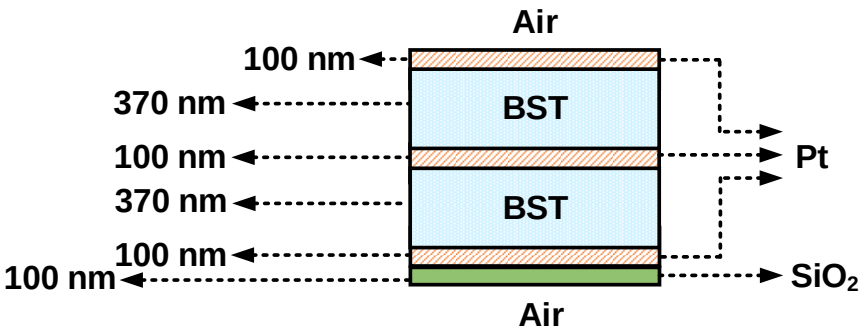

Fig. 6.7 The bilayer BST resonator structure and the finalized thickness values for each layer.

thickness of the Pt electrodes is set to 100 nm, and the thickness of the BST layers is determined based on the Mason model of the device to meet the design frequency. The electrical and acoustic parameters of the materials used to develop the Mason model are provided in [15]. The finalized thickness of all the layers is shown in Fig 6.7. Based on these simulations, the electromechanical coupling coefficient (K_{eff}) for mode 1 and mode 2 are expected to be 8% and 7 %, respectively. The small variation in the K_{eff}^2 of the two modes is due to the finite thickness of the electrodes and the addition of the oxide layer.

The mode-switchable BST FBAR is then employed to design a 1.5-stage ladder-type network filter. The schematic of the designed filter is provided in Fig. 6.8 (a). The device is expected to provide a reconfigurable transfer function with three transmission states: band-pass response at 2 GHz and 3.6 GHz, along with OFF state isolation. The filter is simulated based on the model provided in Fig. 6.5, and its transmission response in all three states is provided in Fig. 6.8 (b). In this model, the C_e values for the shunt and series resonators are set as 3, and 3.2 pF with the rest of the lumped components in mBVD model are determined by (6.26) – (6.29).

6.4 Fabrication Process

The fabrication procedure for the bilayer BST resonator structure is depicted in Fig. 6.9. Devices are fabricated on high resistivity silicon wafers. The process starts by thermally growing a 100 nm diffusion barrier oxide layer on the silicon wafers. After that, the bottom electrodes are deposited and patterned by evaporation and lift-off. Next, the first ferroelectric BST transduction layer is sputter deposited at 650 ^{o}C in a 45 mTorr Ar and O_2 environment (with a 4 to 1 partial pressure ratio). The ferroelectric BST thin film here has a composition ratio of x = 0.5, which corresponds to a Curie temperature of -20°C

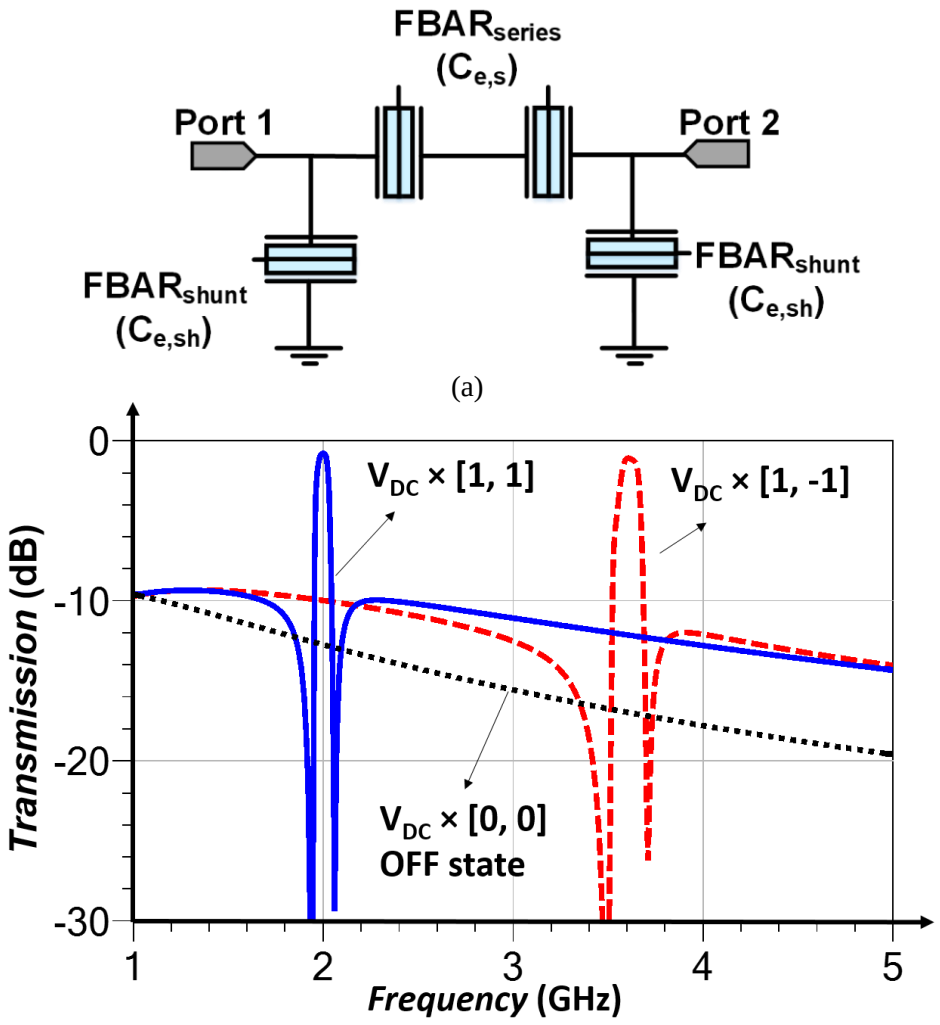

Fig. 6.8 (a) Schematic of the 1.5- stage ladder-type network filter based on mode-switchable BST FBARs and (b) its transmission response for mode 1 (2 GH), mode 2 (3.6 GHz), and OFF state.

and a paraelectric phase at room temperature. The middle electrode and the second BST layer are then deposited with a process similar to the first set of layers. A 100 nm-thick Pt layer is deposited and patterned with evaporation and lift-off to form the top electrodes. Afterward, the BST films and SiO_2 layers are selectively etched in buffered hydrofluoric acid (BHF) to form the releasing windows and the vias to the middle and bottom electrodes. Biasing lines are realized by a 50 nm-thick NiChrome film. A 1.5 μm Al/Au layer is

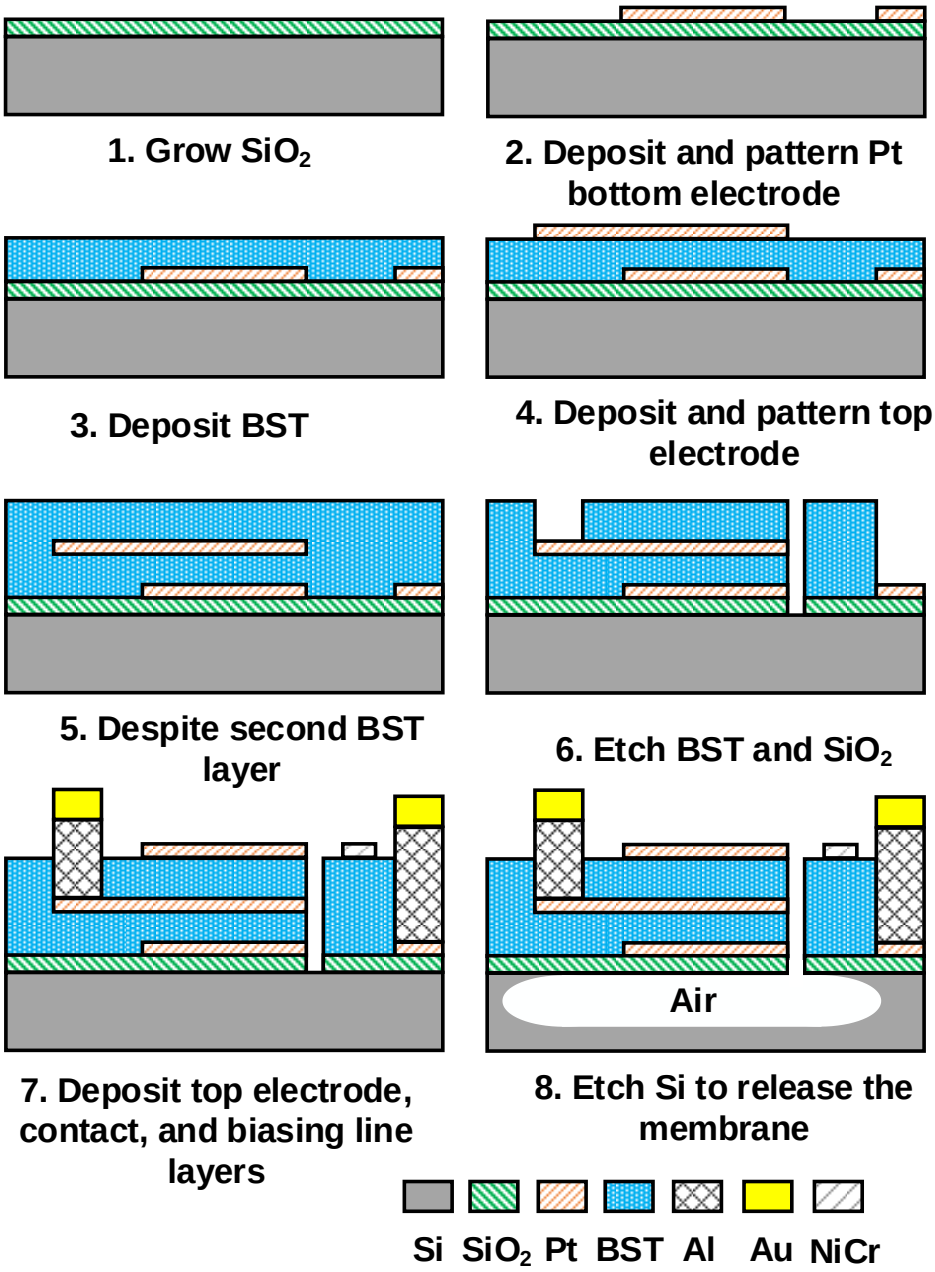

Fig. 6.9 The fabrication process for the mode-switching bilayer BST resonators.

deposited and patterned with evaporation and lift off to create the contact layer for probing the device. Finally, to release the devices' membrane, the silicon substrate beneath them is dry-etched using gaseous XeF_2.

The S-parameters of the fabricated devices are measured using a vector network analyzer with 250 µm-pitch ground-signal-ground (GSG) probes. On-wafer short-open-load-thru (SOLT) probe calibration is performed from 0.2 to 5 GHz for a 50 Ω system impedance.

6.5 Experimental Results and Discussion

Photographs of a mode-switchable BST FBAR with an active area of 38 µm × 38 µm and a 1.5 stage band-switching filter are shown in Fig. 6.10 (a) and (c). The filter unit-cell occupies only 90 µm × 110 µm. The cross-sectional view and the measurement setup for the resonator and the filter are provided in Fig. 6.10 (b) and (d), respectively. Bias voltages

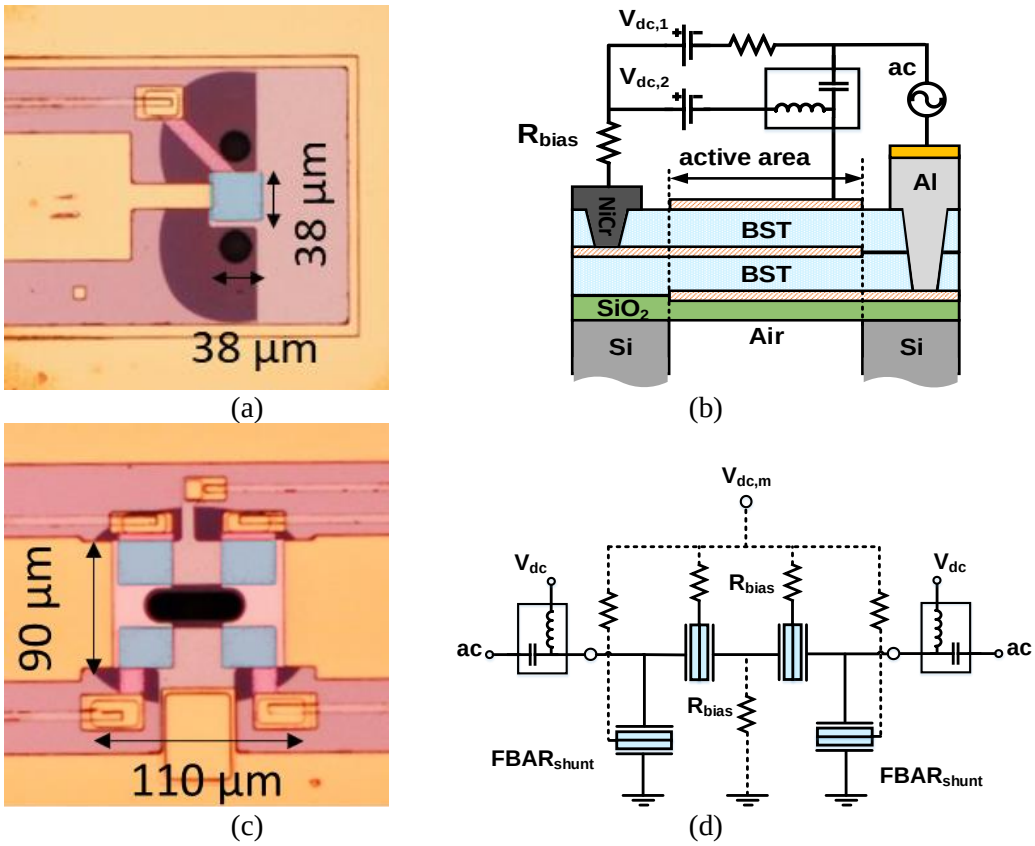

Fig. 6.10 (a) A photograph and (b) the cross-sectional view of a bilayer BST FBAR with its biasing circuit as well as a (c) band-switchable 1.5 stage filter with its bias circuit (d) are presented. Highlighted blue rectangles in the photographs are the resonators' active area.

are applied through bias tees connected to the ports and a DC probe connected to the middle electrodes of the resonators through a high resistivity NiChrome line. The resonator switches between 2 GHz and 3.6 GHz resonance modes by alternating the DC biasing control voltage polarity across one of the BST films. In practice, this can be done by using polarity inverting circuits like differential amplifiers or Buck-Boost converters. The magnitude of the input impedance for a measured 1-port bilayer stacked BST FBAR under both resonance modes is displayed in Fig. 6.11 (a) with the OFF state response. Mode 1 turns on by applying a 40 V DC bias voltage to each BST layer with a similar polarity ($40\ \mathrm{V} \times\ [1, 1]$), which excites a resonance at 1.96 GHz. The device switches to mode 2 by changing the polarity of the bias voltage in one of the BST layers (i.e., $40\ \mathrm{V} \times\ [1, -1]$), exciting a resonance at 3.6 GHz. Furthermore, as shown in Fig. 6.11 (a), when one of the two resonance modes are turned on, the other mode is entirely suppressed, resulting in a smooth out-of-band response. The device turns off when no DC bias voltage is applied to the BST layers and acts as a simple capacitor, as shown in the figure. The mechanical quality factor and electromechanical coupling coefficient are estimated by (6.30) and (6.31) using the mBVD model parameters extracted from the measurements (provided in Table 6.1). The measured Q_m and K_{eff}^2 for mode 1 are 110 and 7.9%, and for mode 2 are 120 and 6.9%, respectively. As expected from (6.15), the K_{eff}^2 of the second mode is comparable with the fundamental mode.

$$Q_m = \frac{\omega_r L_m}{R_m} \tag{6.30}$$

$$K_{eff}^2 = \frac{\pi^2}{4} \frac{f_r (f_a - f_r)}{f_a^2} \tag{6.31}$$

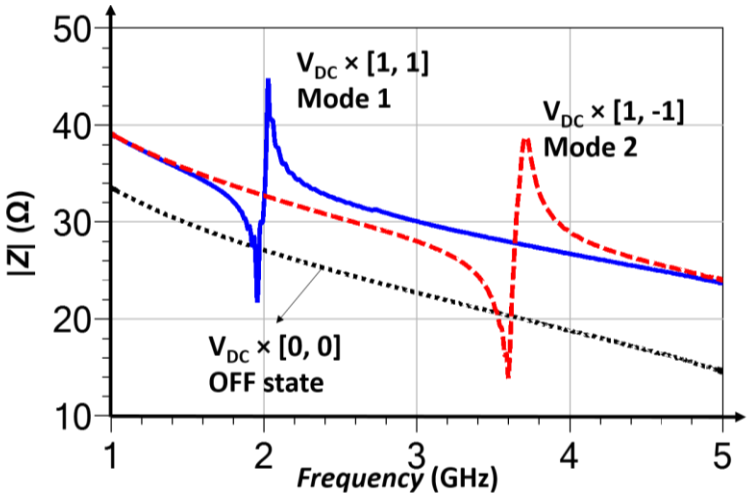

(a)

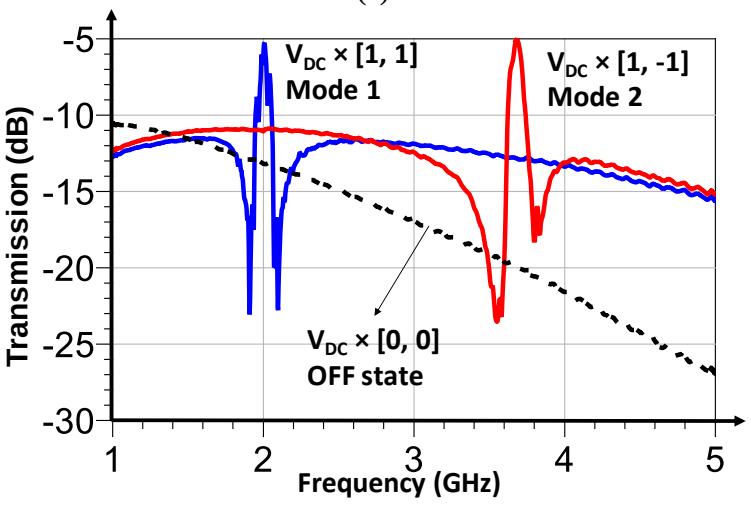

(b)

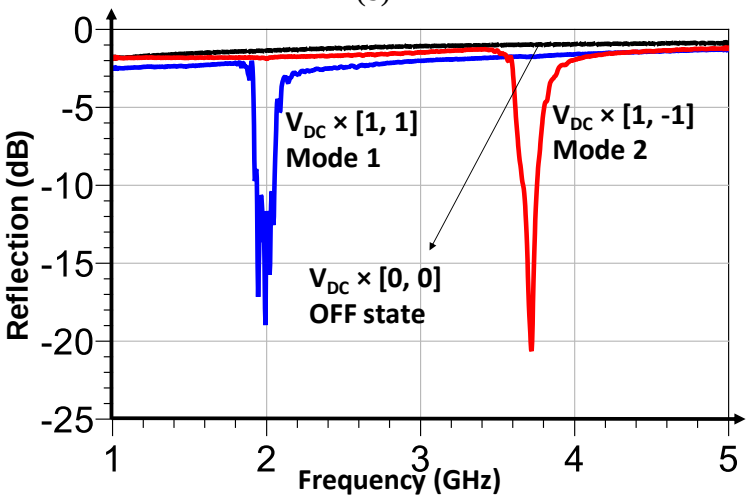

c)

Fig. 6.11 (a) The magnitude of the measured electrical impedance for mode 1, mode 2, and the OFF state, and the corresponding (b) transmission and (c) reflection response of 1.5 stage ladder-type filter.

Table 6.1
The mBVD Model Parameters

Parameter	Mode 1	Mode 2
L_m (nH)	62.9	23.2
R_m (Ω)	8.12	4.4
C_m (fF)	105	84
C_e (pF)	1.60	1.64
R_e (Ω)	4.76	1.74
R_s (Ω)	1.3	1.5
L_s (nH)	0.15	0.15

The measured transmission and reflection response of a ladder-type filter comprised of bilayer BST FBARs, under different biasing control voltage configurations, are provided in Fig. 6.11 (b) and (c), respectively. The transfer function of the filter is electrically controlled to select a passband centered at 2 GHz or 3.6 GHz or isolate the input and output ports (OFF state). The insertion loss of the measured filter is larger than predicated values, due to several reasons including its lower than expected mechanical quality factor, excitation of some spurious lateral modes, and excessive mass loading of filter's shunt resonators. This is the first demonstration of a band-switching ladder-type filter; its performance needs to be enhanced by improving the multilayer BST resonator parameters (Q_m and K_{eff}^2) through optimization of the device structure and the multilayer ferroelectric thin film deposition. For instance, the thickness of the middle electrodes, which are used only for DC biasing, can be reduced to limit the acoustic loss in the conductor layers and confine the acoustic energy into the BST transduction layers, thereby improving the

resonator quality factor and its electromechanical coupling coefficient. Furthermore, the lateral wave spurious modes, which are more noticeable in the lower frequency band, can be eliminated through the design of raised frame structures, as discussed in [28], [58].

6.6 Conclusion

New mode-switchable multilayer ferroelectric FBARs are presented. The electromechanical coupling coefficient of the longitudinal thickness modes for a multi-layer ferroelectric resonator is calculated, demonstrating selective excitation of higher-order modes with constant K_{eff}^2 values. This is accomplished by exploiting the electric-field-induced piezoelectricity and negative piezoelectricity in multilayer BST. Such multi-layer technology enables the development of resonators operating at high microwave and millimeter-wave frequencies with large K_{eff}^2 values. Mode-switchable resonators can also simplify the RF frontend modules by eliminating the need for external switches and reducing the overall number of required filters. The idea is experimentally validated through the fabrication and measurement of a bilayer BST resonator that selectively resonates at its first or second harmonic modes. A band-switching 1.5 stage ladder-type filter is also integrated based on such resonators for the first time.

CHAPTER VII:

Conclusion and Future Work

Sales of RF front-ends are expected to reach 18 billion US dollars by the end of 2020, and the growing number of required RF filters, as shown in Fig. 7.1, is the main driver for this business opportunity [71]. For multi-band operation, the RF filters are currently used in conjunction with switchplexers to select the desired bands and mode of operation. The switches within the RF modules can be eliminated by employing reconfigurable filters to

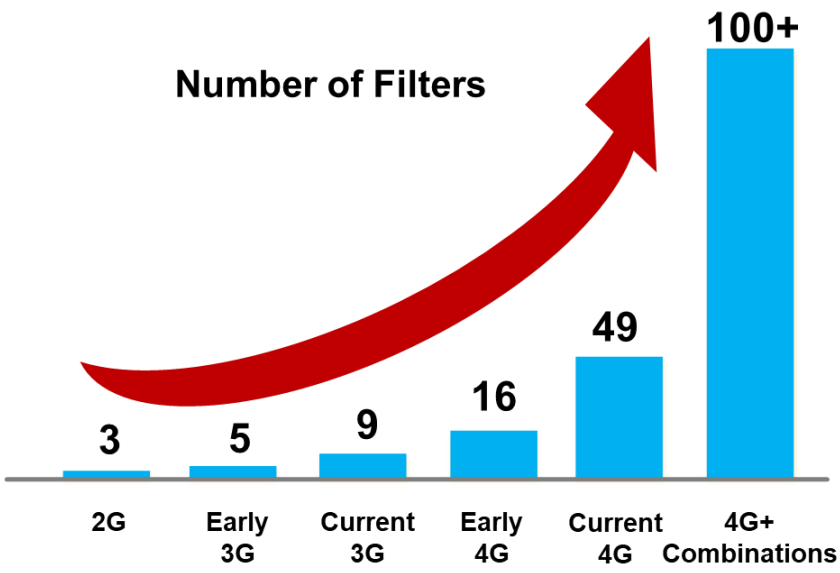

Fig. 7.1 The number of frequency bands and accordingly the number of required filters in mobile phones is exponentially growing with each generation of communication networks. [61]

reduce the size, complexity, and cost of the future RF-front-ends considerably. Reconfigurable RF acoustic wave devices based on thin film ferroelectric BST as a potential solution was presented in this dissertation. Ferroelectric BST possesses several unique characteristics, including electric-field-induced piezoelectricity and 'negative' piezoelectricity, E-field-dependent permittivity, and high relative permittivity, which were employed in the design of reconfigurable RF devices. The BST devices presented herein demonstrate the feasibility of fabricating intrinsically switchable and mode switchable resonators, filters, and filter banks, aimed at simplifying the future RF front-ends by eliminating the need for external switches and also reducing the number of required filters.

7.1 Switchless BST Filter Bank

The intrinsically switchable ferroelectric filter bank example presented in chapter 4 demonstrates the feasibility of BST based switchable filter banks. However, optimized BST filter banks are yet to be designed to meet state of the art RF front-end specifications. Future work involves the enhancement of the BST FBAR figure of merit ($Q_m \times K_t^2$) as well as the development of a design methodology for the switchless filter banks. Improving the BST FBARs' parameters (Q_m and K_t^2) is essential for designing low loss switchable filters and is part of the ongoing research efforts. For example, optimization of the BST thin film deposition conditions, including the annealing process and the gas composition during the BST deposition, is currently under investigation. The structure of the BST FBARs can also be further improved by apodization, which smoothens out the resonators' spurious lateral modes, and subsequently, small ripples in the passband and near-in rejection area. Moreover, it should be noted that the required DC bias voltage values for turning on the resonators are a function of the BST thin film thickness and its deposition condition. By

using a composite FBAR structure, the required DC bias voltage can be reduced to < 30 V [15], [20]. Optimization of the material quality can also reduce the FBARs' required DC bias voltage. The performance of the filter bank can be further enhanced by optimizing the filter bank configuration for minimizing the reactive loading effect of the OFF state filters without using the varactors. A possible way is to employ the approaches developed for the synthesis of multiplexers with the manifold configuration, as described in [63], [64]. The simulation results of a switchable filter bank with a circuit topology similar to the conventional manifold multiplexers, as shown in Fig. 7.2, based on BST FBARs with a K_t^2 and Q_m of 8% and 800, respectively, are shown in Fig. 7.3. Based on these parameters, the intrinsically switchable filter bank provides a minimum insertion loss of 2 dB, out-of-band rejection and isolation levels more than 30 dB, and a fractional bandwidth of 4% at center frequencies of 1.7, 1.8, 1.9, and 2.0 GHz. The phase shifters in this simulation are composed of series capacitors followed by shunt inductors. All the shunt inductors can be combined into one inductor connected to the antenna node.

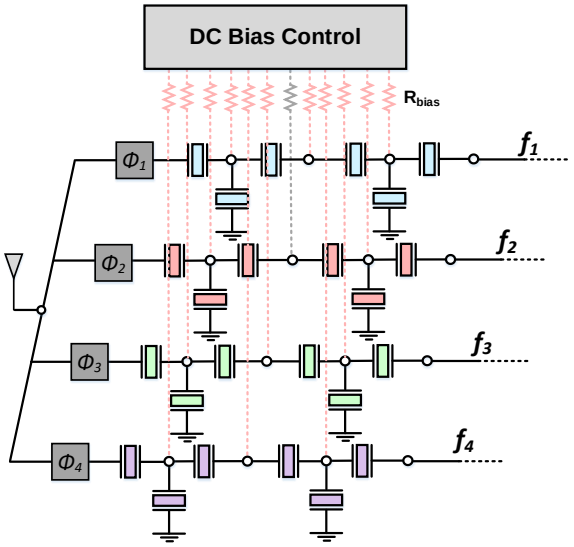

Fig. 7.2 Schematic of a switchless filter bank; phase shifters are employed to reduce the capacitive loading effect and improve the antenna matching.

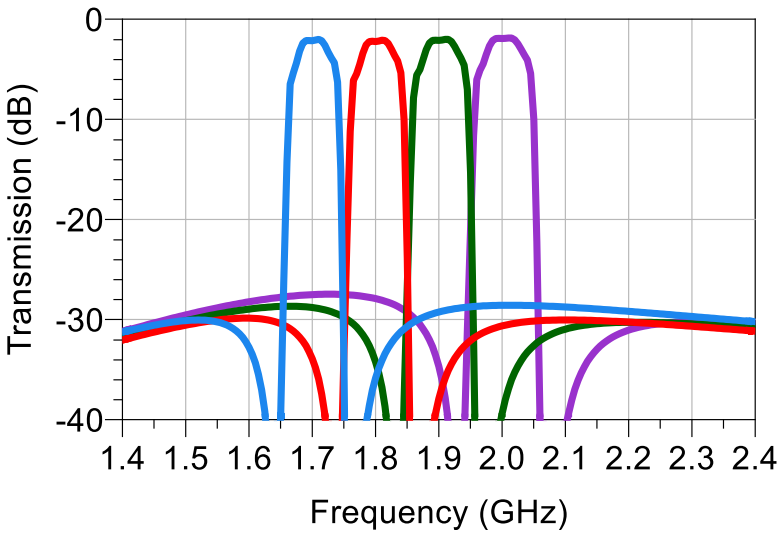

Fig. 7.3 Simulation results for a switchable filter bank consisting of four 2.5-stage filters in their ON state, superimposed in one figure.

7.2 Extremely High Frequency Bulk Acoustic Wave Resonators for 5G

With the advent of the 5G, multiple mm-wave frequency bands are also designated for personal communications, causing the number of required filters in each mobile device to exceed 100. However, the classical SAW and BAW technologies cannot support mm-wave frequency bands. This is because current SAW or BAW resonators cannot achieve high Q and large K_t^2 above 6 GHz, required for designing low loss and large bandwidth (BW) filters. In the following, a new class of multilayer BAW resonator is described by expanding the idea presented in the previous chapter. Such resonators are made of piezoelectric materials having positive and negative piezoelectric coefficients and are capable of meeting the requirements of emerging mm-wave frequency communication standards. The calculations provided in the previous chapter indicate that BAW resonators containing multiple layers of materials with positive piezoelectric effect and negative piezoelectric effect can be designed to operate at mm-wave frequencies to achieve high effective K_t^2 values comparable to that of high performance acoustic resonators at much

lower frequencies. Furthermore, such new multilayer BAW resonator structures are expected to be mechanically robust, providing high manufacturing yields commensurate to low-cost commercial applications. Such resonators can be used as building blocks for designing RF filters with large bandwidths and low insertion losses at high microwave and millimeter-wave frequencies, currently not achievable by the available piezoelectric based technologies.

The resonance frequency of BAW resonators is dictated by the device membrane thickness (Fig. 7.3 (a)). In such a structure, in order to maintain a low ohmic loss, the electrode to piezoelectric thickness ratio is large in very thin resonator membranes at mm-wave frequencies. In such resonators, the acoustic energy ratio in the metal electrodes is increased, causing high acoustic losses and reduced K_t^2. Moreover, such thin membranes are not mechanically robust, suffering from low manufacturing yields. Therefore, the

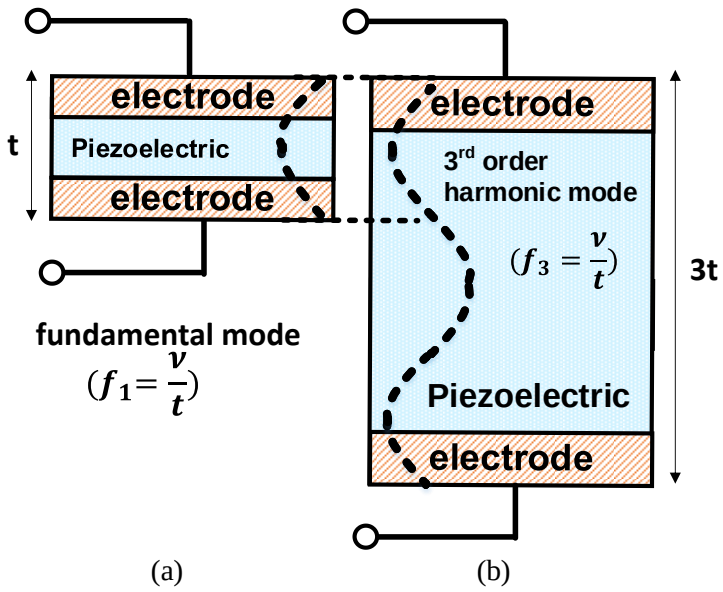

Fig. 7.4 Two resonators with (a) fundamental and (b) 3rd order harmonic resonance modes at f_1. In this figure, for simplicity, the acoustic wave velocity in metal and piezoelectric material is assumed to be similar (v); but in general form they are not necessary similar.

conventional thickness scaling of acoustic resonators applied at lower frequencies is no longer practical at mm-wave frequencies.

To address the above challenges, one can consider designing mm-wave frequency bulk acoustic resonators operating the higher-order harmonic resonance modes in thick membranes. For instance, a resonator, excited by its 3rd order harmonic frequency equal to the fundamental resonance frequency of the resonator shown in Fig. 7.3 (a), is shown in Fig 7.3 (b). In this structure, the ratio of acoustic energy inside the electrodes to the energy inside the piezoelectric material is reduced, which at first glance seems promising. However, in such bulk acoustic wave resonators, the electromechanical coupling coefficient of harmonic resonance modes also drops with a ratio of $1/ f_n^2$ (i.e., for nth harmonic mode ($f_n = nf_1$) the electromechanical coupling coefficient is $K_{eff,n}^2 = \frac{1}{n^2} K_{eff,1}^2$) [30]. Hence ultimately, the lower electromechanical coupling coefficient of resonators described above limits their utility in filters for future radios. The drawbacks of the above approaches are remedied by the new resonator structure described in the following paragraphs.

The structure of a resonator taking advantage of negative and positive piezoelectricity presented in this section is detailed in Fig. 7.4. As shown, multiple layers of alternating piezoelectric materials with negative and positive piezoelectric coefficients sandwiched between two electrodes, forming a BAW resonator. Based on the general electromechanical coupling coefficient equation [30], provided in (7.1), it is possible to excite harmonic resonance mode of such structure with an electromechanical coupling coefficient equal to the fundamental mode in single layer structures (i.e., $K_{eff,n}^2 = K_{eff,1}^2$,

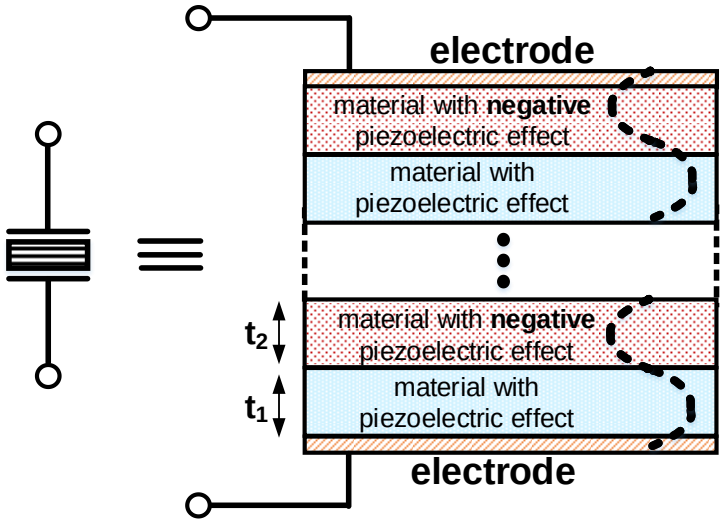

Fig. 7.5 Multi-layer piezoelectric/ferroelectric resonator structure.

contrary to the trend ($K_{eff,n}^2 = \frac{1}{n^2} K_{eff,1}^2$ **)** exhibited by conventional piezoelectric bulk acoustic wave resonators). For example, the electromechanical coupling coefficient for the n[th] harmonic mode of the resonator described herein, with n piezoelectric layers, is approximated to be $K_{eff,n}^2 = \frac{8}{\pi^2}\frac{d_o^2}{s\epsilon}$, which is equal to the one for fundamental resonance mode in single layer structures. (For simplicity, in the calculations, the thickness of electrodes is assumed to be negligible. Also, the magnitude of positive and negative piezoelectric coefficients for both layers is assumed to be equal to d_o, which can be different in the actual device; these approximations, however, do not affect the main conclusion drawn.). Such a multilayered resonator can maintain a high electromechanical coupling coefficient for higher order modes at mm-wave frequencies, an important achievement required for 5G and beyond.

$$K_{eff,n}^2 = \frac{\left(\int_A \int_{-\frac{t_{total}}{2}}^{\frac{t_{total}}{2}} d_{eff}(z) E T(z) dz\right)^2}{\int_V \epsilon E^2 dV \int_V s T^2(z) dV} = \frac{d_o^2}{2s\epsilon\left(\frac{t_{total}}{2}\right)^2}\left(\int_{-\frac{t_{total}}{2}}^{\frac{t_{total}}{2}} \tilde{d}(z)\tilde{u}_N'(z) dz\right)^2 = \frac{8}{\pi^2}\frac{d_o^2}{s\epsilon} \qquad (7.1)$$

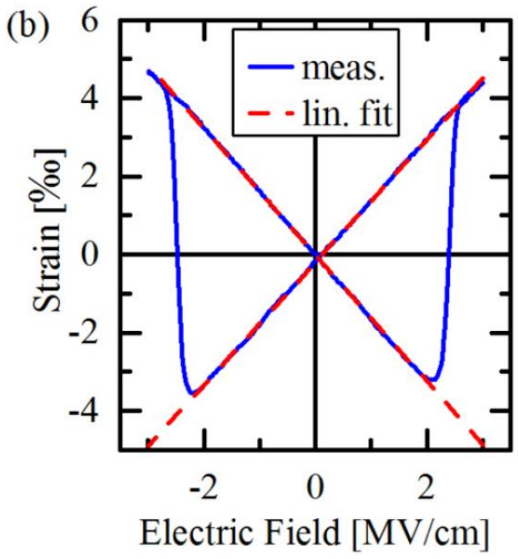

Fig. 7.6 Converse piezoelectric effect: longitudinal strain response of $Al_{0.64}Sc_{0.36}N$ [65].

where s, and ϵ are the average elasticity and permittivity of the piezoelectric layers. Also, $\tilde{d}\,(z)$ is the normalized piezoelectric coefficient in each layer, and $\tilde{u}'_N(z)$ is the normalized stress distribution throughout the bulk of the resonator.

In the proposed structure of Fig. 7.4, two types of materials with positive and negative piezoelectric coefficients are utilized: positive piezoelectric coefficient layers can be made of conventional piezoelectric materials, like AlN, ZnO, LNO, PZT, BTO, etc., while the negative piezoelectric coefficient layers can be made of BST, Sc doped AlN in its ferroelectric phase, $CuInP_2S_6$ (CIPS), etc. [73]–[75]. For instance, the longitudinal displacement butterfly curve of the inverse piezoelectric effect for $Al_{0.64}Sc_{0.36}N$ has broad linear regimes with almost equal slopes, corresponding to an effective longitudinal piezoelectric coefficient d_{33} of 15.7 Pico meter per volt (pm/V) and a negative piezoelectric coefficient of -16.2 pm/V, as shown in Fig. 7.5 [73].

The proposed resonator structure can be constructed using conventional bulk acoustic wave fabrication technologies and can be in the form of a thin film bulk acoustic wave

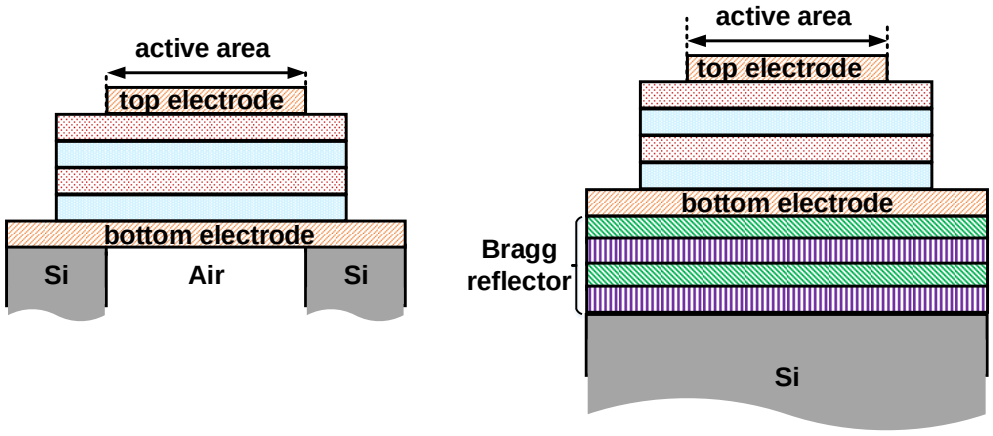

(a) (b)

Fig. 7.7 Realization of the proposed multilayer resonators through (a) thin film bulk acoustic wave resonator (FBAR), and (b) solidly mounted resonator (SMR) technologies,.

resonator (FBAR) as well as a solidly mounted resonator (SMR), as shown in Fig 7.6. In SMR structure, the acoustic wave reflection at the bottom of the resonator is provided through a Bragg reflector instead of an air interface.

Multiphysics simulations have been performed for FBAR structures, validating the theoretical calculations presented here. The stress field distribution of 8 alternating layers of AlN/ScAlN, each having a thickness of 216 nm with 123 nm-thick Mo electrodes (total thickness of 2 μm), is shown in Fig. 7.7. The membrane structure resonates at 26 GHz (10^{th}

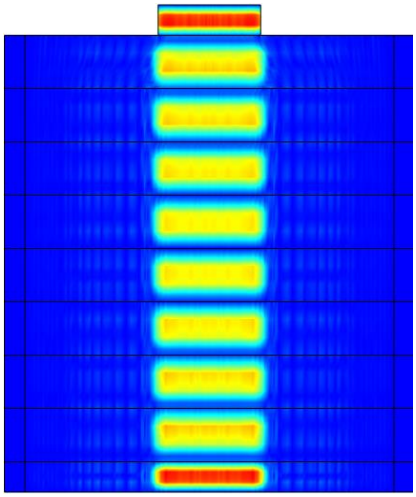

Fig. 7.8 Stress distribution in an eight-layer ScAlN/AlN resonator with Mo electrodes.

harmonic mode of the structure) with an electromechanical coupling coefficient of 6% (for reference fundamental mode AlN resonators at sub-6 GHz frequencies exhibit similar electromechanical coupling coefficient values.) Thus, multilayer BAW resonators can achieve a large electromechanical coupling coefficient at mm-wave frequencies while maintaining membrane thickness values that provide substantial structural robustness. Such resonators allow the design of BAW filters with bandwidths required at mm-waves (e.g., Fig. 7.8 (a)). The expected transmission response of a ladder-type 2.5 stage filter based on the simulated resonator is provided in Fig. 7.8 (b). The filter achieves an unprecedented operation frequency of 26 GHz with a very sharp roll-off only exhibited by acoustic filters at low GHz frequencies.

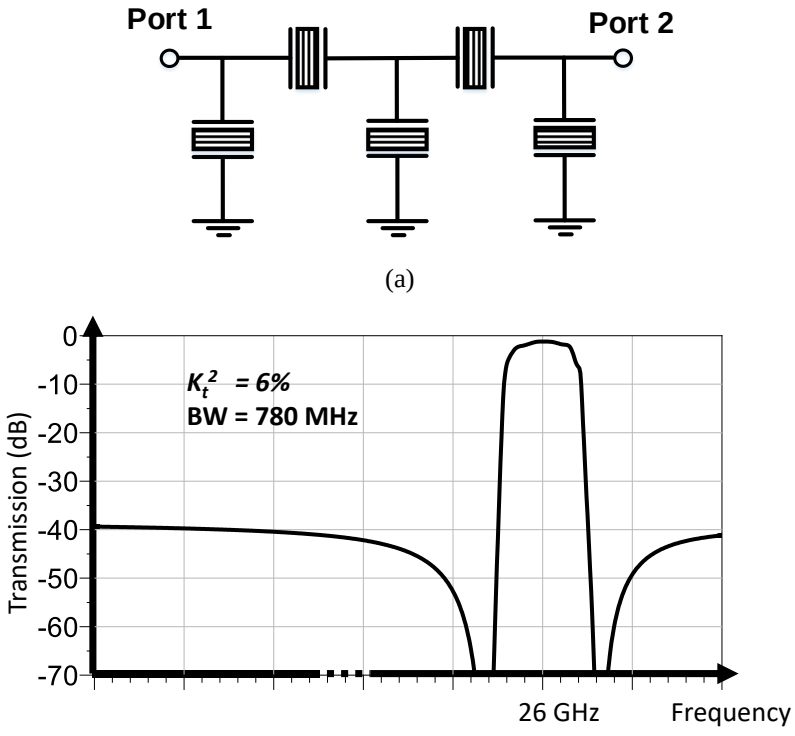

Fig. 7.9 (a) Schematic of a ladder-type filter based on the proposed resonator, and (b) the transmission response of a filter based on the simulated FBARs of Fig 7.7.

Finally, the presented multilayer mm-wave resonators are expected to have high quality factors. This is due to the fact that the total thickness of the transduction layer in such resonators is multiple wavelengths, which: 1) reduces the fraction of acoustic energy lost in electrodes, 2) allows minimizing the RF loss by increasing the electrodes' thickness.

7.3 Publications

Based on the work in this dissertation, the following peer-reviewed journal and conference publications have been published. Some work are currently under review or to be submitted for publication.

7.3.1 Published Journal Articles

1. **M. Zolfagharloo Koohi**, A. Mortazawi, "Negative Piezoelectric Based Electric-field-actuatedMode-switchable Multilayer BST FBARs for Selective Control of Harmonic Resonances withoutDegrading K^2_{eff}," in *IEEE Transactions on Ultrasonics, Ferroelectrics, and Frequency Control(TUFFC)*, Early Access.
2. **M. Zolfagharloo Koohi**, A. Mortazawi, "Towards Reconfigurable Radios Employing Multifunctional Ferroelectrics," in *IEEE Microwave Magazine*, May 2020.
3. **M. Zolfagharloo Koohi**, S. Nam, A. Mortazawi, "Intrinsically Switchable and Bandwidth Reconfigurable Ferroelectric Bulk Acoustic Wave Filters," in *IEEE Transactions on Ultrasonics, Ferroelectrics, and Frequency Control (TUFFC)*, December 2019.
4. **M. Zolfagharloo Koohi**, S. Lee, A. Mortazawi, "Compact Intrinsically Switchable FBAR Filters Utilizing Ferroelectric BST," in *IEEE Transactions on Ultrasonics, Ferroelectrics, and Frequency Control (TUFFC)*, May 2018.
5. **M. Zolfagharloo Koohi**, A. Mortazawi, "Intrinsically Switchable Filter Bank Employing Ferroelectric Barium Strontium Titanate," in *IEEE Transactions on Microwave Theory and Techniques (TMTT)*, September 2018.

7.3.2 Conference Proceedings

1. **M. Zolfagharloo Koohi**, Wenhao Peng, A. Mortazawi, "An Intrinsically Switchable BalancedFerroelectric FBAR Filter at 2 GHz,"IEEE International Microwave Symposium (IMS), LosAngeles, CA, June 2020.

2. **M. Zolfagharloo Koohi,** A. Mortazawi, "Switched Mode Thin Film Bulk Acoustic Wave Resonators," *IEEE International Microwave Symposium (IMS),* Boston, MA, June 2019.

3. **M. Zolfagharloo Koohi,** S. Nam, A. Mortazawi, "Intrinsically Switchable Miniature Ferroelectric Stacked Crystal Filters," *IEEE International Microwave Symposium (IMS),* Boston, MA, June 2019.

4. **M. Zolfagharloo Koohi**, A. Mortazawi, "On the Linearity of BST Thin Film Bulk Acoustic Resonators," *IEEE MTT-S International Microwave Workshop Series on Advanced Materials and Processes,* Ann Arbor, MI, July 2018.

5. **M. Zolfagharloo Koohi,** S. Nam, A. Mortazawi, "Linearity Measurements of Intrinsically Switchable BST FBAR Filters," *IEEE European Microwave Conference (EuMC),* Madrid, September 2018.

6. **M. Zolfagharloo Koohi**, S. Lee, A. Mortazawi, "A Compact Intrinsically Switchable Filter Bank Employing Multifunctional Ferroelectric BST," *IEEE International Microwave Symposium (IMS),* Philadelphia, PA, June 2018.

7. **M. Zolfagharloo Koohi**, S. Nam, A. Mortazawi, "Intrinsically Switchable and Bandwidth Reconfigurable FBAR Filter Employing Electrostriction in Ferroelectric BST," *IEEE International Microwave Symposium (IMS),* Philadelphia, PA, June 2018.

8. **M. Zolfagharloo Koohi,** A. Mortazawi, "BST Thin Film Bulk Acoustic Resonator Optimization for Un-cooled IR Sensors Application," *IEEE European Microwave Conference (EuMC),* Nuremberg, 2017.

9. **M. Zolfagharloo Koohi,** S. Lee, A. Mortazawi, "Fabrication of a Low Insertion Loss Intrinsically Switchable BAW Filter Based on BST FBARs," *IEEE International Microwave Symposium (IMS),* Honolulu, HI, June 2017.

10. **M. Zolfagharloo Koohi,** S. Lee, A. Mortazawi, "High $Q_m \times K_t^2$ Intrinsically Switchable BST Thin Film Bulk Acoustic Resonators," *IEEE International Microwave Symposium (IMS),* Honolulu, HI, June 2017.

11. **M. Zolfagharloo Koohi,** S. Lee, A. Mortazawi, "Design of BST-on-Si Composite FBARs for Switchable BAW Filter Application," *IEEE European Microwave Conference (EuMC),* London, October 2016.

12. **M. Zolfagharloo Koohi,** S. Lee, S.A. Sis, V. Lee, A. Mortazawi, "Un-cooled Resonant IR Detectors Based on Barium Strontium Titanate Switchable FBARs," *IEEE The 45th European Microwave Conference (EuMC),* Paris, September 2015.

13. S. Lee, **M. Zolfagharloo Koohi,** A. Mortazawi, "Elimination of Lateral Mode Spurious Resonance in Switchable Ferroelectric BST-on-Si Composite FBARs," *IEEE International Microwave Symposium (IMS),* San Francisco, CA, May 2016.

14. S. Lee, **M. Zolfagharloo Koohi,** S.A. Sis, V. Lee, A. Mortazawi, "Temperature Dependent Characteristics of Intrinsically Switchable Ferroelectric Composite

FBARs," *IEEE International Microwave Symposium (IMS)*, Pheonix, AZ, May 2015.

References

[1] Ericsson, “Ericsson Mobility Report November 2018,” 2018. Accessed: Aug. 06, 2020. [Online]. Available: www.ericsson.com/mobility-report.

[2] R. Ruby, “A snapshot in time: The future in filters for cell phones,” *IEEE Microw. Mag.*, vol. 16, no. 7, pp. 46–59, Aug. 2015, doi: 10.1109/MMM.2015.2429513.

[3] A. Hagelauer, G. Fattinger, C. C. W. Ruppel, M. Ueda, K. Y. Hashimoto, and A. Tag, “Microwave Acoustic Wave Devices: Recent Advances on Architectures, Modeling, Materials, and Packaging,” *IEEE Trans. Microw. Theory Tech.*, vol. 66, no. 10, pp. 4548–4562, Oct. 2018, doi: 10.1109/TMTT.2018.2854160.

[4] I. J. Busch-Vishniac, “Trends in Electromechanical Transduction,” *Phys. Today*, vol. 51, no. 7, pp. 28–34, Jul. 1998, doi: 10.1063/1.882325.

[5] A. Ozgurluk, M. Akgul, and C. T. C. Nguyen, “RF Channel-Select Micromechanical Disk Filters-Part I: Design,” *IEEE Trans. Ultrason. Ferroelectr. Freq. Control*, vol. 66, no. 1, pp. 192–217, 2018, doi: 10.1109/TUFFC.2018.2881727.

[6] J. Wang, Z. Ren, and C. T. C. Nguyen, “1.156-GHz self-aligned vibrating micromechanical disk resonator,” *IEEE Trans. Ultrason. Ferroelectr. Freq. Control*, vol. 51, no. 12, pp. 1607–1627, Dec. 2004, doi: 10.1109/TUFFC.2004.1386679.

[7] S. Pourkamali, A. Hashimura, R. Abdolvand, G. K. Ho, A. Erbil, and F. Ayazi, “High-Q single crystal silicon HARPSS capacitive beam resonators with self-aligned sub-100-nm transduction gaps,” *J. Microelectromechanical Syst.*, vol. 12, no. 4, pp. 487–496, Aug. 2003, doi: 10.1109/JMEMS.2003.811726.

[8] F. D. Bannon, J. R. Clark, and C. T. C. Nguyen, “High-Q HF Microelectromechanical Filters,” *IEEE J. Solid-State Circuits*, vol. 35, no. 4, pp. 512–526, 2000, doi: 10.1109/4.839911.

[9] X. Zhu, J. D. Phillips, and A. Mortazawi, “A DC voltage dependant switchable thin film bulk wave acoustic resonator using ferroelectric thin film,” in *IEEE MTT-S International Microwave Symposium Digest*, 2007, pp. 671–674, doi: 10.1109/MWSYM.2007.380009.

[10] J. Berge, A. Vorobiev, W. Steichen, and S. Gevorgian, “Tunable solidly mounted thin film bulk acoustic resonators based on Ba xSr1-xTiO3 films,” *IEEE Microw. Wirel. Components Lett.*, vol. 17, no. 9, pp. 655–657, Sep. 2007, doi:

10.1109/LMWC.2007.903445.

[11] A. Vorobiev, S. Gevorgian, M. Löffler, and E. Olsson, “Correlations between microstructure and Q-factor of tunable thin film bulk acoustic wave resonators,” in *Journal of Applied Physics*, Sep. 2011, vol. 110, no. 5, p. 054102, doi: 10.1063/1.3626939.

[12] X. Zhu, V. Lee, J. Phillips, and A. Mortazawi, “An intrinsically switchable FBAR filter based on barium titanate thin films,” *IEEE Microw. Wirel. Components Lett.*, vol. 19, no. 6, pp. 359–361, Jun. 2009, doi: 10.1109/LMWC.2009.2020013.

[13] A. Noeth, T. Yamada, A. K. Tagantsev, and N. Setter, “Electrical tuning of dc bias induced acoustic resonances in paraelectric thin films,” *J. Appl. Phys.*, vol. 104, no. 9, p. 094102, Nov. 2008, doi: 10.1063/1.2999642.

[14] A. Vorobiev, J. Berge, S. Gevorgian, M. Löffler, and E. Olsson, “Effect of interface roughness on acoustic loss in tunable thin film bulk acoustic wave resonators,” *J. Appl. Phys.*, vol. 110, no. 2, p. 024116, Jul. 2011, doi: 10.1063/1.3610513.

[15] S. Sis, S. Lee, V. Lee, A. Bayraktaroglu, J. Phillips, and A. Mortazawi, “Intrinsically switchable, high-Q ferroelectricon-silicon composite film bulk acoustic resonators,” *IEEE Trans. Ultrason. Ferroelectr. Freq. Control*, vol. 61, no. 2, pp. 231–238, 2014, doi: 10.1109/TUFFC.2014.6722609.

[16] S. Lee, V. Lee, S. A. Sis, and A. Mortazawi, “Large-signal performance and modeling of intrinsically switchable ferroelectric FBARs,” *IEEE Trans. Microw. Theory Tech.*, vol. 61, no. 1, pp. 415–422, 2013, doi: 10.1109/TMTT.2012.2225442.

[17] S. A. Sis, “Ferroelectric-on-Silicon Switchable Bulk Acoustic Wave Resonators and Filters for RF Applications,” 2014.

[18] S. Gevorgian, *Ferroelectrics in Microwave Devices, Circuits and Systems*, no. 1. London: Springer London, 2009.

[19] R. A. York, “4 Tunable Dielectrics for RF Circuits,” Scitech Publishing, 2009.

[20] S. Gevorgian, A. K. Tagantsev, and A. Vorobiev, “Tuneable Film Bulk Acoustic Wave Resonators,” Springer London, 2013, pp. 1–15.

[21] N. K. Pervez, P. J. Hansen, and R. A. York, “High tunability barium strontium titanate thin films for rf circuit applications,” in *Applied Physics Letters*, Nov. 2004, vol. 85, no. 19, pp. 4451–4453, doi: 10.1063/1.1818724.

[22] A. Tombak *et al.*, “Tunable barium strontium titanate thin film capacitors for RF and microwave applications,” *IEEE Microw. Wirel. Components Lett.*, vol. 12, no. 1, pp. 3–5, Jan. 2002, doi: 10.1109/7260.975716.

[23] D. Y. Chen and J. D. Phillips, “Electric field dependence of piezoelectric coefficient in ferroelectric thin films,” in *Journal of Electroceramics*, Dec. 2006, vol. 17, no. 2–4, pp. 613–617, doi: 10.1007/s10832-006-9335-0.

[24] M. Zolfagharloo Koohi and A. Mortazawi, “Reconfigurable Radios Employing Ferroelectrics: Recent Progress on Reconfigurable RF Acoustic Devices Based on Thin-Film Ferroelectric Barium Strontium Titanate,” *IEEE Microw. Mag.*, vol. 21, no. 5, pp. 120–135, May 2020, doi: 10.1109/MMM.2020.2971376.

[25] V. Lee, S. A. Sis, J. D. Phillips, and A. Mortazawi, “Intrinsically switchable ferroelectric contour mode resonators,” *IEEE Trans. Microw. Theory Tech.*, vol. 61, no. 8, pp. 2806–2813, 2013, doi: 10.1109/TMTT.2013.2271756.

[26] M. Z. Koohi, S. Lee, and A. Mortazawi, “High Qm×K2t intrinsically switchable BST thin film bulk acoustic resonators,” in *IEEE MTT-S International Microwave Symposium Digest*, Oct. 2017, pp. 296–299, doi: 10.1109/MWSYM.2017.8059101.

[27] V. C. Lee, “Switchable and Tunable Ferroelectric Devices for Adaptive and Reconfigurable RF Circuits,” University of Michigan, 2014.

[28] S. Lee, M. Z. Koohi, and A. Mortazawi, “Lateral-wave spurious-modes elimination in switchable ferroelectric BST-on-Si composite FBARs,” in *IEEE MTT-S International Microwave Symposium Digest*, Aug. 2016, vol. 2016-August, doi: 10.1109/MWSYM.2016.7540120.

[29] J. D. Larson, P. D. Bradley, S. Wartenberg, and R. C. Ruby, “Modified Butterworth-Van Dyke circuit for FBAR resonators and automated measurement system,” *Proc. IEEE Ultrason. Symp.*, vol. 1, pp. 863–868, 2000, doi: 10.1109/ULTSYM.2000.922679.

[30] Ken-Ya Hashimoto, *RF bulk acoustic wave filters for communications*. Artech House, 2009.

[31] M. Z. Koohi, S. Lee, and A. Mortazawi, “Design of BST-on-si composite FBARs for switchable BAW filter application,” in *European Microwave Week 2016: “Microwaves Everywhere”, EuMW 2016 - Conference Proceedings; 46th European Microwave Conference, EuMC 2016*, 2016, pp. 1003–1006, doi: 10.1109/EuMC.2016.7824515.

[32] NXP, “DC-to-DC Boost Converters are changing the Face of Mobile Commerce.” www.nxp.com (accessed Aug. 31, 2020).

[33] R. Mahameed, N. Sinha, M. B. Pisani, and G. Piazza, “Dual-Beam Actuation of Piezoelectric AlN RF MEMS Switches Monolithically Integrated with AlN Contour-Mode Resonators Recommended Citation ‘Dual-Beam Actuation of Piezoelectric AlN RF MEMS Switches Monolithically Integrated with AlN Contour-Mode Resonators,’” 2008. Accessed: Aug. 07, 2020. [Online]. Available:

http://repository.upenn.edu/ese_papers.

[34] G. N. Saddik, D. S. Boesch, S. Stemmer, and R. A. York, “Dc electric field tunable bulk acoustic wave solidly mounted resonator using SrTiO3,” *Appl. Phys. Lett.*, vol. 91, no. 4, p. 043501, Jul. 2007, doi: 10.1063/1.2759464.

[35] G. N. Saddik and R. A. York, “An L-section DC electric field switchable bulk acoustic wave solidly mounted resonator filter based on Ba0.5Sr0.5TiO 3,” 2011, doi: 10.1109/ISAF.2011.6014000.

[36] S. Lee and A. Mortazawi, “An Intrinsically Switchable Ladder-Type Ferroelectric BST-on-Si Composite FBAR Filter,” *IEEE Trans. Ultrason. Ferroelectr. Freq. Control*, vol. 63, no. 3, pp. 456–462, Mar. 2016, doi: 10.1109/TUFFC.2016.2517643.

[37] M. Z. Koohi, S. Lee, and A. Mortazawi, “Fabrication of a Low insertion loss intrinsically switchable BAW filter based on BST FBARs,” in *IEEE MTT-S International Microwave Symposium Digest*, Oct. 2017, pp. 1480–1483, doi: 10.1109/MWSYM.2017.8058900.

[38] C. Zuo and G. Piazza, “Single-ended-to-differential and differential-to-differential channel-select filters based on piezoelectric aln contour-mode MEMS resonators,” in *2010 IEEE International Frequency Control Symposium, FCS 2010*, 2010, pp. 5–8, doi: 10.1109/FREQ.2010.5556383.

[39] S. Lee and A. Mortazawi, “BAW filter design method based on intrinsically switchable ferroelectric BST FBARs,” in *IEEE MTT-S International Microwave Symposium Digest*, Aug. 2016, vol. 2016-August, doi: 10.1109/MWSYM.2016.7540105.

[40] C. Muller and M. A. Dubois, “Effect of size and shape on the performances of BAW resonators : A model and its applications,” in *Proceedings - IEEE Ultrasonics Symposium*, 2008, pp. 1552–1556, doi: 10.1109/ULTSYM.2008.0378.

[41] M. Z. Koohi and A. Mortazawi, “On the Linearity of BST Thin Film Bulk Acoustic Resonators,” Sep. 2018, doi: 10.1109/IMWS-AMP.2018.8457167.

[42] C. D. Nordquist and R. H. Olsson, “Power handling and intermodulation distortion of contour-mode AlN MEMS resonators and filters,” 2011, doi: 10.1109/MWSYM.2011.5972814.

[43] C. Zuo, N. Sinha, and G. Piazza, “Very high frequency channel-select MEMS filters based on self-coupled piezoelectric AlN contour-mode resonators,” *Sensors Actuators, A Phys.*, vol. 160, no. 1–2, pp. 132–140, 2010, doi: 10.1016/j.sna.2010.04.011.

[44] K. M. Lakin, J. Belsick, J. F. McDonald, and K. T. McCarron, “High performance stacked crystal filters for GPS and wide bandwidth applications,” *Proc. IEEE*

Ultrason. Symp., vol. 1, pp. 833–838, 2001, doi: 10.1109/ULTSYM.2001.991849.

[45] K. M. Lakin, "Bulk acoustic wave coupled resonator filters," in *Proceedings of the Annual IEEE International Frequency Control Symposium*, 2002, pp. 8–14, doi: 10.1109/freq.2002.1075848.

[46] K. M. Lakin, "Modeling of thin film resonators and filters," in *IEEE MTT-S International Microwave Symposium Digest*, Jun. 1992, vol. 1, pp. 149–152, doi: 10.1109/mwsym.1992.187931.

[47] K. M. Lakin, "Equivalent Circuit Modeling of Stacked Crystal Filters," Sep. 2008, pp. 257–262, doi: 10.1109/freq.1981.200482.

[48] M. Z. Koohi and A. Mortazawi, "Negative Piezoelectric Based Electric-field-actuated Mode-switchable Multilayer Ferroelectric FBARs for Selective Control of Harmonic Resonances Without Degrading k2eff," *IEEE Trans. Ultrason. Ferroelectr. Freq. Control*, pp. 1–1, Apr. 2020, doi: 10.1109/tuffc.2020.2988632.

[49] P. K. Agyapong, M. Iwamura, D. Staehle, W. Kiess, and A. Benjebbour, "Design considerations for a 5G network architecture," *IEEE Commun. Mag.*, vol. 52, no. 11, pp. 65–75, 2014, doi: 10.1109/MCOM.2014.6957145.

[50] G. Yuan, X. Zhang, W. Wang, and Y. Yang, "Carrier aggregation for LTE-advanced mobile communication systems," *IEEE Commun. Mag.*, vol. 48, no. 2, pp. 88–93, Feb. 2010, doi: 10.1109/MCOM.2010.5402669.

[51] S. Lee, M. Zolfagharloo Koohi, S. A. Sis, V. Lee, and A. Mortazawi, "Temperature dependent characteristics of intrinsically switchable ferroelectric composite FBARs," Jul. 2015, doi: 10.1109/MWSYM.2015.7167036.

[52] M. Z. Koohi and A. Mortazawi, "BST thin film bulk acoustic resonator optimization for un-cooled IR sensors application," in *European Microwave Week 2017: "A Prime Year for a Prime Event", EuMW 2017 - Conference Proceedings; 47th European Microwave Conference, EuMC 2017*, Dec. 2017, vol. 2017-January, pp. 328–330, doi: 10.23919/EuMC.2017.8230861.

[53] M. Zolfagharloo Koohi, S. Lee, and A. Mortazawi, "Compact intrinsically switchable FBAR filters utilizing ferroelectric BST," *IEEE Trans. Ultrason. Ferroelectr. Freq. Control*, vol. 65, no. 8, pp. 1468–1474, Aug. 2018, doi: 10.1109/TUFFC.2018.2839756.

[54] M. Z. Koohi, S. Nam, and A. Mortazawi, "Linearity Measurements of Intrinsically Switchable BST FBAR Filters," in *2018 48th European Microwave Conference, EuMC 2018*, Nov. 2018, pp. 830–832, doi: 10.23919/EuMC.2018.8541805.

[55] M. Z. Koohi and A. Mortazawi, "Intrinsically Switchable Filter Bank Employing Ferroelectric Barium Strontium Titanate," in *IEEE Transactions on Microwave Theory and Techniques*, Dec. 2018, vol. 66, no. 12, pp. 5501–5507, doi:

10.1109/TMTT.2018.2867196.

[56] P. Kužel, F. Kadlec, H. Němec, R. Ott, E. Hollmann, and N. Klein, “Dielectric tunability of SrTiO3 thin films in the terahertz range,” *Appl. Phys. Lett.*, vol. 88, no. 10, p. 102901, Mar. 2006, doi: 10.1063/1.2183370.

[57] V. Lee, S. Lee, S. A. Sis, and A. Mortazawi, “Switching reliability and switching speed of barium strontium titanate (BST) BAW devices,” in *European Microwave Week 2014: Connecting the Future, EuMW 2014 - Conference Proceedings; EuMC 2014: 44th European Microwave Conference*, Dec. 2014, pp. 500–503, doi: 10.1109/EuMC.2014.6986480.

[58] J. Kaitila, M. Ylilammi, J. Ellä, and R. Aigner, “Spurious resonance free bulk acoustic wave resonators,” in *Proceedings of the IEEE Ultrasonics Symposium*, 2003, vol. 1, pp. 84–87, doi: 10.1109/ultsym.2003.1293361.

[59] R. Ruby, J. Larson, C. Feng, and S. Fazzio, “The effect of perimeter geometry on FBAR resonator electrical performance,” in *IEEE MTT-S International Microwave Symposium Digest*, 2005, vol. 2005, pp. 217–220, doi: 10.1109/MWSYM.2005.1516563.

[60] A. Link and P. Warder, “Golden age for filter design: Innovative and proven approaches for acoustic filter, duplexer, and multiplexer design,” *IEEE Microw. Mag.*, vol. 16, no. 7, pp. 60–72, Aug. 2015, doi: 10.1109/MMM.2015.2431236.

[61] E. R. Crespin *et al.*, “Fully integrated switchable filter banks,” 2012, doi: 10.1109/MWSYM.2012.6259652.

[62] S. Mahon, J. Zepess, and M. H. Andrews, “BAW Flip-Chip Switched Filter Bank Delivers Dramatic Form Factor Reduction,” *High Freq. Electron.*, 2008.

[63] G. G. Fattinger *et al.*, “Carrier aggregation and its challenges - Or: The golden age for acoustic filters,” in *IEEE MTT-S International Microwave Symposium Digest*, Aug. 2016, vol. 2016-August, doi: 10.1109/MWSYM.2016.7540211.

[64] B. G. Alfred Raul, “RF Filters and Multiplexers Based on Acoustic Wave Technologies with Ladder-Type and Cross-Coupled Topologies Designing Under a Systematic Strategy,” Universitat Autonoma De Barcelona, 2016.

[65] T. Komatsu, K. Y. Hashimoto, T. Omori, and M. Yamaguchi, “Tunable radio-frequency filters using acoustic wave resonators and variable capacitors,” *Jpn. J. Appl. Phys.*, vol. 49, no. 7 PART 2, pp. 7–24, Jul. 2010, doi: 10.1143/JJAP.49.07HD24.

[66] H. Hirano *et al.*, “Bandwidth-tunable SAW filter based on wafer-level transfer-integration of BaSrTiO3 film for wireless LAN system using TV white space,” in *IEEE International Ultrasonics Symposium, IUS*, Oct. 2014, pp. 803–806, doi: 10.1109/ULTSYM.2014.0197.

[67] K. Matsutani *et al.*, “A novel switchable SAW Duplexer for band 28,” in *IEEE MTT-S International Microwave Symposium Digest*, Oct. 2017, pp. 1679–1682, doi: 10.1109/MWSYM.2017.8058963.

[68] M. Z. Koohi, S. Nam, and A. Mortazawi, “Intrinsically Switchable and Bandwidth Reconfigurable Ferroelectric Bulk Acoustic Wave Filters,” *IEEE Trans. Ultrason. Ferroelectr. Freq. Control*, vol. 67, no. 5, pp. 1025–1032, May 2020, doi: 10.1109/TUFFC.2019.2958675.

[69] X. Zhu, D. Y. Chen, Z. Jin, J. D. Phillips, and A. Mortazawi, “Characterization of thin film BST tunable capacitors using a simple two port measurement technique,” in *IEEE MTT-S International Microwave Symposium Digest*, 2005, vol. 2005, pp. 611–614, doi: 10.1109/MWSYM.2005.1516674.

[70] N. K. Pervez, P. J. Hansen, and R. A. York, “High tunability barium strontium titanate thin films for rf circuit applications,” in *Applied Physics Letters*, Nov. 2004, vol. 85, no. 19, pp. 4451–4453, doi: 10.1063/1.1818724.

[71] “Qualcomm and TDK Joint Venture Slides.” https://www.qualcomm.com/media/documents/files/qualcomm-and-tdk-joint-venture-slides.pdf (accessed Aug. 07, 2020).

[72] M. Z. Koohi and A. Mortazawi, “Switched Mode Thin Film Bulk Acoustic Wave Resonators,” in *IEEE MTT-S International Microwave Symposium Digest*, Jun. 2019, vol. 2019-June, pp. 528–531, doi: 10.1109/mwsym.2019.8700959.

[73] S. Fichtner, N. Wolff, F. Lofink, L. Kienle, and B. Wagner, “AlScN: A III-V semiconductor based ferroelectric,” *J. Appl. Phys.*, vol. 125, no. 11, p. 114103, Mar. 2019, doi: 10.1063/1.5084945.

[74] L. You *et al.*, “Origin of giant negative piezoelectricity in a layered van der Waals ferroelectric,” *Sci. Adv.*, vol. 5, no. 4, p. eaav3780, Apr. 2019, doi: 10.1126/sciadv.aav3780.

[75] I. Katsouras *et al.*, “The negative piezoelectric effect of the ferroelectric polymer poly(vinylidene fluoride),” *Nat. Mater.*, vol. 15, no. 1, pp. 78–84, Jan. 2016, doi: 10.1038/nmat4423.